

A STUDY OF THE FINE-SCALE THREE-DIMENSIONAL FLOW STRUCTURES IN
TURBULENCE USING TIME-RESOLVED STEREOSCOPIIC SCANNING
PARTICLE IMAGE VELOCIMETRY

by

YE CHENG

A Dissertation submitted to the
Graduate School-New Brunswick
Rutgers, The State University of New Jersey
in partial fulfillment of the requirements

for the degree of

Doctor of Philosophy

Graduate Program in Mechanical and Aerospace Engineering

written under the direction of

Professor Francisco Javier Diez

and approved by

New Brunswick, New Jersey

October, 2011

©2011

Ye Cheng

ALL RIGHTS RESERVED

ABSTRACT OF THE DISSERTATION

A Study of the Fine-Scale Three-Dimensional Flow Structures in Turbulence Using
Time-Resolved Stereoscopic Scanning Particle Image Velocimetry

By YE CHENG

Dissertation Director:
Professor Francisco Javier Diez

A time-resolved stereoscopic scanning particle image velocimetry (TR-SSPIV) system was developed to investigate the fine-scale 3D structures in free shear turbulent jets. The system provided a simultaneous measurement of the three-component velocity field in a three-dimensional volume (3D3C) with Kolmogorov-scale (η) resolution, providing a true representation of the complete nine-component velocity gradient tensor. Quantitative visualization of the coherent structures at fine-scale turbulence is obtained and four basic structural shapes (sheets, tube, square ribbons and spherical blobs) are identified as building blocks of complex turbulent structures. The measurement volume had dimensions of $43\eta \times 20\eta \times 18\eta$, which allowed isolating individual structures. These rendered shapes had dimensions that range from $1.5-5\eta$ to $20-30\eta$. The local acceleration $\partial \mathbf{u} / \partial t$ is obtained and represented as 3D structures. These showed a strong anti-alignment with the convective acceleration term, which helps validate

experimentally the Random Taylor Hypothesis. A novel vortex identification scheme is also introduced based on the local pressure. The method is compared to other published ones including enstrophy, Q , λ_2 and Δ criteria. Four different flow configurations are tested and extensive statistical analyses are performed to study the probability density function (PDF), joint PDF, and spectra of the velocity gradients. The analysis also considered the vorticity, rate of strain, enstrophy, and dynamic parameters such as enstrophy production rate and energy dissipation rate. Accuracy assessments included result comparison to isotropy theory and evaluation of the local conservation of mass. The flow statistics and scaling of turbulence at fine scales are compared extensively to published theoretical, numerical, and experimental results.

ACKNOWLEDGEMENT

I would like to show my gratitude to my advisor, Dr. F. Javier Diez, for his constant support and guidance throughout my five years of research and study at Rutgers University. He has always been patient and helpful whenever I have had any questions or encountered setbacks. His strong passion in scientific research has inspired me. He has taught me so much, from the basics of fluid mechanics to the complex theories in turbulence, and from performing a good experiment to writing a technical paper. I would have never gone this far if it weren't for him and I am proud to be his first doctorate student.

I would also like to thank Prof. Yogesh Jaluria, Prof. Doyle D. Knight and Prof. Qizhong Guo for being my committee members. They offered many valuable suggestions and kindly encouraged me during my dissertation process.

Many thanks to all my labmates for their help and company: Mariusz, Tom, Jon, Andrew, Josh, and Dan. Thanks to Arturo Villegas for his help and ideas with the data analysis and to my former labmate and friend always, Maria Del Mar Torregrosa, for her help with the experimental setup. Thank you to dear my friends Kellie and Tyree for making my life here enjoyable and memorable. Last but not least, I would like to express my gratefulness to my parents, Cheng Yanping and Wang Chunxiang, for their endless love and support and to all my family and friends.

NOMENCLATURE

D	Jet Nozzle Diameter
E	Enstrophy
l	Characteristic Length Scale
J_0	Momentum Flux at Jet Exit
P	Pressure
Q	Second Invariant of Velocity Gradient Tensor $Q = \frac{1}{2}(\ \Omega\ ^2 - \ S\ ^2)$
\dot{Q}	Volumetric Flow Rate
R	Third Invariant of Velocity Gradient Tensor $R = -\det(\nabla u)$
r	Jet Radial Location
Re_D	Reynolds Number Based on Jet Nozzle Diameter
Re_δ	Local Outer Reynolds Number
Re_λ	Taylor Reynolds Number
S	Norm of Rate of Strain Tensor
t	Time
U_0	Jet Exit Velocity
u	X-Component of Velocity
u_c	Local Jet Centerline Velocity
\mathbf{u}	Velocity Vector
u'	RMS Turbulence Intensity
v	Y-Component of Velocity
w	Z-Component of Velocity
Δ	Vortex Identification Parameter $\Delta = \left(\frac{1}{2}R\right)^2 + \left(\frac{1}{3}Q\right)^3$
Ω	Norm of Skew-symmetric Vorticity Tensor
α, β, γ	Three Principal Strain Rates $\alpha > \beta > \gamma$
δ	Outer Length Scale
ε	Turbulent Kinetic Energy Dissipation Rate

ϕ, φ	Orientation Angles of Principal Strain Rates
η	Kolmogorov Length Scale
κ	Wave Number $\kappa \equiv 2\pi/l$
λ_2	Intermediate Eigenvalue of Tensor $S^2 + \Omega^2$
λ_f	Longitude Taylor Length Scale
λ_g	Transverse Taylor Length Scale
λ_v	Viscous Length Scale
μ	Dynamic Viscosity
ν	Kinematic Viscosity
ρ	Density
τ_δ	Outer Time Scale
τ_η	Kolmogorov Time Scale
τ_v	Viscous Time Scale
ω	Vorticity
ξ	Local Divergence Error $\xi = \frac{(\partial u/\partial x + \partial v/\partial y + \partial w/\partial z)^2}{(\partial u/\partial x)^2 + (\partial v/\partial y)^2 + (\partial w/\partial z)^2}$

TABLE OF CONTENTS

ABSTRACT OF THE DISSERTATION	ii
ACKNOWLEDGEMENT	iv
NOMENCLATURE.....	v
TABLE OF CONTENTS	vii
LIST OF TABLES	ix
LIST OF FIGURES	x
Chapter 1 Introduction.....	1
1.1 BACKGROUND	1
1.2 REVIEW OF VELOCITY GRADIENT TENSOR MEASUREMENTS	2
1.3 REVIEW OF TURBULENT FLOW STRUCTURE VISUALIZATION	4
1.4 REVIEW OF PIV TECHNIQUES USED IN THE STUDY OF TURBULENCE	7
1.5 DISSERTATION OUTLINE	10
Chapter 2 Time-Resolved Stereoscopic Scanning PIV System.....	13
2.1 IMAGE ACQUISITION SYSTEM.....	14
2.2 SCANNING LIGHT SHEETS CHARACTERIZATION.....	15
2.3 SYSTEM TIMING AND SYNCHRONIZATION	18
2.4 STEREOSCOPIC CALIBRATION	19
2.5 IMAGE PROCESSING PROCEDURE.....	21
Chapter 3 Free Round Turbulent Jets	33
3.1 EXPERIMENTAL SETUP	34
3.2 FLOW CONDITIONS.....	35

3.3 TURBULENT JET VALIDATION	36
3.4 SCALES OF TURBULENT MOTION	38
Chapter 4 Visualization of Fine-Scale Flow Structures in Turbulent Jets	56
4.1 VISUALIZATION OF FLOW STRUCTURE: VELOCITY	57
4.2 VISUALIZATION OF FLOW STRUCTURE: VELOCITY GRADIENT	59
4.3 VISUALIZATION OF FLOW STRUCTURE: ACCELERATION	63
4.4 VISUALIZATION OF FLOW STRUCTURE: VORTICITY AND STRAIN RATE	64
4.5 VORTEX IDENTIFICATION.....	68
Chapter 5 Statistical Analysis of Turbulence.....	96
5.1 MEASUREMENT CONFIGURATIONS.....	97
5.2 VELOCITY GRADIENTS AND ISOTROPY	97
5.3 PRINCIPAL STRAIN RATES	101
5.4 ENSTROPY AND ENSTROPY PRODUCTION RATE	105
5.5 ENERGY DISSIPATION RATE	106
5.6 ENERGY AND DISSIPATION SPECTRUM	107
5.7 ACCURACY ASSESSMENT.....	109
Chapter 6 Concluding Remarks	143
Bibliography	147

LIST OF TABLES

Table 1.1. Comparison between current PIV techniques.	12
Table 3.1. Flow conditions of the three cases for the turbulent round jet measurements.	46
Table 3.2. Scaling parameters of round turbulent jet for the three flow configurations.	55
Table 4.1. Description of various vortex identification methods.	90
Table 5.1 Measured ratios of mean square velocity gradients, also showing results from Mullin and Dahm 2006, Ganapathisubramani et al. 2007 and from homogeneous isotropic theory for comparison.	115
Table 5.2. Scaling exponent α of left and right tails of the 9 velocity gradient PDFs for Case 1.	116
Table 5.3. Scaling exponent α of left and right tails of the 9 velocity gradient PDFs for Case 2.	117
Table 5.4. Scaling exponent α of left and right tails of the 9 velocity gradient PDFs for Case 3.	118
Table 5.5. Measured ratios of mean square velocity gradients, also showing results from Mullin & Dahm 2006, Ganapathisubramani et al. 2007 and from axisymmetric isotropic theory for comparison.	119
Table 5.6. Comparison of present measured velocity gradient moment skewness and kurtosis with other work.	120
Table 5.7. RMS velocity fluctuation for each component and the error ratio. The result compares favorably to Mullin & Dahm 2006.	137
Table 5.8. Energy dissipation rate calculation with different methods and assumptions.	142

LIST OF FIGURES

Figure 2.1. Layout of time-resolved stereoscopic scanning PIV system.	23
Figure 2.2. Layout of optical system used in the time-resolved stereoscopic scanning PIV system. A low-inertia galvanometric scanning mirror rapidly sweeps a vertical laser sheet horizontally through a small volume.	24
Figure 2.3. Calibration curve for rotating mirror. The angle of rotation α is linearly proportional to the input peak-to-peak voltage V_{pp}	25
Figure 2.4. Typical results for laser sheet profile measurements normal to sheet direction, showing raw measured power values and error function fit (left), and corresponding derivatives giving sheet power profile and its Gaussian fit (right).	26
Figure 2.5. Typical result of number of particles that the camera detects across the laser sheet, showing raw measured number of particles (symbols) and Gaussian fit (line).	27
Figure 2.6. Normalized laser sheet intensity profile and normalized detected number of particles profile across the laser sheet. The $1/e$ value was used to quantify the sheet thickness. The two methods provide very similar results.	28
Figure 2.7. Timing diagram showing mirror position during PIV image acquisition for each volume (top), and camera exposure timing during laser pulse.	29
Figure 2.8. Schematic of stereoscopic projection principles.	30
Figure 2.9. Picture of calibration target on a traverse stage.	31
Figure 2.10. Flowchart of image processing procedure with calibration, volume reconstruction and velocity and velocity gradients calculation.	32
Figure 3.1. Sketch of the flow facility and laser illumination. a) Jet injected in a seeded water tank horizontally along x direction. b) Close up view of the observation volume showing size and location.	44
Figure 3.2. Sketch of the orientation of the laser sheet and camera with respect to the jet showing a) the side view, and b) the cross-sectional view orientation.	45
Figure 3.3. Radial profile of jet velocity at the exit, computed with 200 images from 10 independent sets.	47

Figure 3.4. Normalized mean streamwise velocity contour at $x/D=40-75$ downstream of the jet exit. The mean was computed with 1000 planar PIV images.	48
Figure 3.5. Contour plot of the normalized (a) streamwise and (b) radial rms velocity fluctuations at $x/D=40-75$ downstream of the jet exit.	49
Figure 3.6. Normalized Reynolds stress term contour at $x/D=40-75$ downstream of the jet exit.	50
Figure 3.7. Normalized mean streamwise velocity profile at $x/D=40-70$ downstream of jet exit. The profiles at different downstream locations collapse into one and match with the experimental data from previous work (Wynanski & Fiedler 1969 and Hussein et al. 1994).....	51
Figure 3.8. Normalized streamwise RMS velocity fluctuation profile at $x/D=40-70$ downstream of jet exit compared to DNS results (Boersma et al. 1998) and experimental results (Panchapakesan & Lumley 1993).....	52
Figure 3.9. Normalized radial RMS velocity fluctuation profile at $x/D=40-70$ downstream of jet exit compared to DNS results (Boersma et al. 1998) and experimental results (Panchapakesan & Lumley 1993).....	53
Figure 3.10. Normalized Reynolds stress term profile at $x/D=40-70$ downstream of jet exit compared to DNS results (Boersma et al. 1998) and experimental results (Panchapakesan & Lumley 1993).	54
Figure 4.1. Instantaneous 3D velocity profile. a) 3D contour surface plot. b) Group iso-surface plot, which shows the flow structure in more detail.	73
Figure 4.2. Instantaneous velocity profile showing iso-surfaces from 10 independent experiments at $x/D=157$ (side view camera orientation).....	74
Figure 4.3. Instantaneous velocity profiles from 10 independent experiments at $x/D=157$ cross view camera orientation.	75
Figure 4.4. Evolution of the velocity structure in time. The structures maintain their shape and propagate downstream along the jet centerline axis	76
Figure 4.5. a) Typical instantaneous velocity magnitude showing selected iso-surfaces, and b) same volume after performing a Galilean decomposition by subtracting a velocity $0.80 u_c$ to visualize a turbulent eddy shown by streamlines and by c) a 2D vector field in a close up view.....	77

Figure 4.6. Identification of the iso-surfaces for the same velocity gradient component for different thresholding values: a) $a = 1, 1.5$; b) $a = 2, 3$; c) $a = 3, 4$	78
Figure 4.7. Resolved time series showing at selected time steps the iso-surface for one velocity gradient component being convected in the x-direction.	79
Figure 4.8. Six instantaneous three-dimensional velocity gradients, shown as iso-surfaces for chosen threshold values to extract simple geometrical shapes.....	80
Figure 4.9. Nine instantaneous three-dimensional velocity gradients obtained with 3D3C measurements, shown as iso-surfaces with values normalized by viscous scales.	81
Figure 4.10. Extracted three-dimensional structures of two volumes with velocity gradients that deviated more than $3r_{ms}$ (among 10 3D2C data sets). The streamlines show good correlation between the velocity and velocity gradients.	82
Figure 4.12. Contour plots on surfaces in a volume of the three shear (off-diagonal) rate of strain components.	84
Figure 4.13. Extracted iso-surfaces of the same volume as in Fig. 4.11, showing the three shear (off-diagonal) rate of strain components.	85
Figure 4.14. Extracted iso-surfaces of the same volume as in Fig. 4.12, showing the three vorticity components.	86
Figure 4.15. Combination of strong vorticity and strain rate component structures. The slices show contour of subtracted velocity magnitude and the vectors show the three-component velocity field. The combination of vorticity and strain rate appears at a focus type of vortex.....	87
Figure 4.16. Contour plots of enstrophy, enstrophy production rate and energy dissipation rate.....	88
Figure 4.17. Extracted iso-surfaces of the same volume as in Fig. 4.15, showing enstrophy, enstrophy production rate and energy dissipation rate.	89
Figure 4.18. Iso-surfaces of enstrophy accompanied with velocity slices showing velocity magnitude (contour) and streamlines. Enstrophy structures occur at both focus and saddle type of flow pattern.	91
Figure 4.19. Enstrophy and velocity field. a) 3D view with enstrophy iso-surfaces and velocity slices; b) 2D view of enstrophy contour. Enstrophy represents both vortex tubes and sheet-like structure created by shear.....	92

Figure 4.20. A sample observation volume showing iso-surfaces represented by different vortex identification parameters. a) Enstrophy b) Q Criterion c) λ_2 criterion d) Δ criterion.	93
Figure 4.21. A sample observation volume showing iso-surfaces represented by different vortex identification parameters. a) Enstrophy b) Q Criterion c) λ_2 criterion d) Δ criterion.	94
Figure 4.22. A sample observation volume showing iso-surfaces represented by different vortex identification parameters. a) Enstrophy b) Q Criterion c) λ_2 criterion d) Δ criterion e) Pressure f) pressure with a slice of velocity field showing location of the vortex.	95
Figure 5.1. Schematic of the four measurement configurations: a) $x/D=150$ downstream jet centerline side-view (Case 1 and 2); b) $x/D=80$ downstream off-centerline side-view (Case 3) c) $x/D=150$ downstream jet cross-view (Case 4).	114
Figure 5.2. PDF of (a) three on-diagonal and (b) six off-diagonal velocity gradients for Case 1 ($Re_D=1500$, $x/D=150$, centerline side-view).	116
Figure 5.3. PDF of (a) three on-diagonal and (b) six off-diagonal velocity gradients for Case 2 ($Re_D=3000$, $x/D=150$, centerline side-view).	117
Figure 5.4. PDF of (a) three on-diagonal and (b) six off-diagonal velocity gradients for Case 3 ($Re_D=1500$, $x/D=80$, off-centerline side-view).	118
Figure 5.5. PDF of three principal strain rates α, β, γ for the Case 1-3. The values of principal strain rates are not normalized. The unit is 1/s.	121
Figure 5.6. PDF of normalized intermediate strain rate for Case 1-3.	122
Figure 5.7. Joint PDF of magnitude of strain rate tensor e and intermediate strain rate β^* for Case 1-3. Unit of e is 1/s. The contour lines are from 0 to 1 with increment of 0.1.	123
Figure 5.8. PDF of the orientation angle of ϕ and θ for three principal strain axes e_i for Case 1.	124
Figure 5.9. PDF of the orientation angle of ϕ and θ for three principal strain axes e_i for Case 2.	125
Figure 5.10. PDF of the orientation angle of ϕ and θ for three principal strain axes e_i for Case 3.	126
Figure 5.11. PDF of enstrophy field with log normal fits for Case 1.	127
Figure 5.12. PDF of enstrophy field with log normal fits for Case 2.	128
Figure 5.13. PDF of enstrophy field with log normal fits for Case 3.	129
Figure 5.14. PDF of enstrophy production rate field with log normal fits for Case 1.	130

Figure 5.15. PDF of enstrophy production rate field with log normal fits for Case 2	131
Figure 5.16. PDF of enstrophy production rate field with log normal fits for Case 3.	132
Figure 5.17. PDF of energy dissipation rate with log normal fits for Case 1.	133
Figure 5.18. PDF of energy dissipation rate with log normal fits for Case 2.	134
Figure 5.19. PDF of energy dissipation rate with log normal fits for Case 3.	135
Figure 5.20. a) Energy and b) dissipation spectra of streamwise velocity compared to the model spectra by Pope 2000.	136
Figure 5.21. PDFs of $\partial w/\partial z$ measured and $\partial w/\partial z$ calculated using mass conservation	
$\partial u/\partial x + \partial v/\partial y + \partial w/\partial z = 0$	138
Figure 5.22. PDF of local divergence error defined as $\xi = \frac{(\partial u/\partial x + \partial v/\partial y + \partial w/\partial z)^2}{(\partial u/\partial x)^2 + (\partial v/\partial y)^2 + (\partial w/\partial z)^2}$. Mass conservation requires $\xi = 0$	139
Figure 5.23. a) PDF of local divergence error normalized with norm of velocity gradient tensor; b) Joint PDF of local divergence error and norm of velocity gradient tensor.	140
Figure 5.24. PDF of $\partial w/\partial z$ of the same jet downstream location measured with side-view configuration (Case 1) and cross-view configuration (Case 4). They show very good agreement, indicating the reliability of the TR-SSPIV system.....	141

Chapter 1

Introduction

1.1 Background

Turbulent flows can be observed in everyday life such as water flow in a river, running tap water, smoke from a chimney, or vortices around a helicopter. In industrial applications, turbulent flows are common and of great importance, as turbulence has the ability to transport and mix fluid very effectively. The study of turbulence is also of great interest to researchers as it occurs in many natural and manmade flows, and the understanding of mass, momentum and energy transport in turbulence has both theoretical and practical importance.

The eddies found in turbulent flows vary greatly in size. The large scale motions are controlled by the geometry of the flow, while the small scale motions generally depend on viscosity and the energy transported from large scales. The small scales in turbulent flows have been widely studied for their nearly universal structures (Kolmogorov 1941) yet they still remain a challenging problem. This is the case when trying to resolve with Kolmogorov-scale resolution turbulent flow structures to obtain a detail three-dimensional representation of their geometry. The Kolmogorov scale, $\eta \equiv (v^3/\varepsilon)^{1/4}$

(where ν is the kinematic viscosity of the fluid and ε is the energy dissipation rate), arguably represents the smallest scales in the flow where viscous dissipation dominates and where the energy cascade ends. Fully resolving the smallest scales can then provide a better understanding of the local viscous dissipation process, its relation to larger scales in the energy cascade process in turbulence as well as characterizing the intermittent fluctuations of velocity.

1.2 Review of velocity gradient tensor measurements

The velocity gradient tensor is known to play an important role in the dynamics of turbulence. The analyses of vorticity, rate of strain, enstrophy production and energy dissipation all depend on the availability of the velocity gradients. But the acquisition of the full nine components of the velocity gradient tensor has been a challenge to experimentalists due to its complexity involving the three-component velocity field and three-dimensional spatial locations. In most instances when the velocity gradient tensor was not available, the dynamic parameters in turbulence, such as energy dissipation rate, had to be estimated using the longitude velocity fluctuations by applying a local isotropic assumption (Kolmogorov 1941) and Taylor Hypothesis (Taylor 1935).

Browne et al. 1987 was among the first to obtain multiple velocity gradient components through experiments. They studied the energy dissipation at the wake of a cylinder and obtained eight of the velocity gradient components using a point measurement hotwire technique. They observed departure from isotropy at the cylinder wake especially by the edges. All nine components were later obtained by Tsinober et al. 1992 with a twelve-

wire hotwire probe in a turbulent grid flow. Other variations of the hotwire technique have been used by Vukoslavcevic & Wallace 1996, Ong & Wallace 1998, Kholmyansky et al. 2001, Wallace & Vukoslavcevic 2010 and Gulitski et al. 2007. The latter obtained the nine components of velocity gradient tensor simultaneously without the need to apply the Taylor hypothesis. They also obtained time derivatives of the velocity (acceleration). Nonintrusive flow measurement techniques such as laser-Doppler velocimetry (LDV) have also been developed to access velocity gradients with higher spatial resolution (Lang & Dimotakis 1982 and Agui & Andreopoulos 2003) but they are still limited to point measurements.

With the development of flow imaging techniques, the spatial resolution of velocity gradient measurement has been greatly improved. Particle tracking velocimetry (PTV) is a technique that measures the three-dimensional location of low concentrated particle fields during a time sequence, from which the velocity vector and full velocity gradient tensor can be obtained (Ishikawa et al. 2000, Holzner et al. 2008, Holzner et al. 2009). Classical particle image velocimetry (PIV) is a two-component velocity planar measurement, which can provide four of the velocity gradient components and isotropic assumptions are required to compute energy dissipation rate (George & Hussein 1991, Saarenrinne & Piirto 2000, Tanaka & Eaton 2007, 2010). To fully resolve the velocity gradient tensor, several new methods were developed as an extension of the traditional PIV system, including dual-plane stereoscopic PIV (Ganapathisubramani et al. 2006, Mullin & Dahm 2006), Holographic PIV (Zhang et al. 1997, Tao et al. 2000, Sheng et al. 2008), cinematographic stereoscopic PIV (Ganapathisubramani et al. 2007, 2008),

Orthogonal-plane cinema-stereoscopic PIV (Steinberg et al. 2009), and tomographic PIV (Staack et al. 2010, Elsinga et al. 2010). The comparison of different PIV techniques used in the measurement of velocity gradient tensor is discussed in §1.4.

1.3 Review of turbulent flow structure visualization

The fine scales of turbulent flows are dominated by coherent structures that are responsible for the mass and momentum transport and energy dissipation. The presence of these coherent structures was first observed by Kline et al. 1967 near the wall of a turbulent boundary layer. Recent reviews (Wallace 2009; Ishihara et al. 2009) show that the study of the 3D turbulent structures has been generally done using direct numerical simulations (DNS). For instance, the three-dimensional Navier–Stokes equations were solved to obtain the 3D vorticity field of turbulent flows (Siggia 1981, Kerr 1985, She et al. 1990, Vincent & Meneguzzi 1991). However, a restriction of DNS is that all scales of the flow must be resolved, from the Kolmogorov scale to the large eddies present in the flow. As a result, the larger the range of scales present (i.e., high Reynolds number), the larger the computational cost. In general, the computational grid number is reduced by limiting the smallest scales resolved to a value on the order of η (Donzis et al. 2008). For instance, Kim et al. (1987) suggested grid spacing on the order of 15η for DNS simulations of turbulent flows to resolve the essential turbulent scales, while more recent studies numerically simulated isotropic turbulence in a box with a 1.57η resolution (Moisy & Jiménez 2004) and even down to 0.95η (Wang 2010) and $0.25\text{--}0.3\eta$ (Donzis et al. 2008, Schumacher et al. 2010).

In turbulent flow at fine scales, the statistics significantly deviate from Gaussian. Rather, it is dominated by random bursts of vorticity and energy dissipation isolated in both space and time. This phenomenon, known as intermittency, is one of the most significant characteristics of turbulence. The characterization of turbulence intermittency has been challenging to researchers due to the lack of a quantitative description of fine scale structures (Frisch & Orszag 1990). Over the years, one of the goals of many DNS studies has been to visualize and quantify the coherent flow structures in fine-scale turbulence. For instance, previous DNS work indicated that strong vorticity fields consist of long tube-like structures (or “worms”) that have diameters on the order of Kolmogorov length scale (Siggia 1981, Kerr 1985, She et al. 1990, Vincent & Meneguzzi 1991). Also, She et al. 1990 visualized the vortex tubes by choosing a vorticity magnitude threshold that is 3-4 times of its RMS value and observed the spiral profile of the velocity field around the vortex tubes. Vincent & Meneguzzi 1991 also discussed the visualization of vortex tubes with different thresholds and they further quantified the geometry of the tubes by plotting the vorticity magnitude along a direction perpendicular to its axis. Passot et al. 1995 explained the formation of vortex tubes and suggested that the vortex tubes evolve from unstable strained vortex layers under combination of compression and self-induced rotation. More recent DNS studies suggest that the intense flow structures are not in fact randomly distributed in space but are organized in a sense of large-scale with clustering (Moisy & Jimenez 2004). They also observed a strong relation between intense vorticity and energy dissipation, which shows that the high vortex tubes are often accompanied by high dissipation rate structures (Sreenivasan 1999, Schumacher et al. 2010). This

correspondence was also observed in terms of time, suggesting that a rapid strain growth triggers rising vorticity with a sudden decline in stretching (Zeff et al. 2003).

To resolve the turbulent structures experimentally, various flow imaging techniques have been developed over the past two decades. Holographic PIV was applied to obtain 3D coherent turbulent structures (Meng & Hussain 1991, Zhang et al. 1997, Pu et al. 2002) and the availability of reconstructed 3D vorticity and strain rate structures has enabled the observation of alignment of vortex tubes to local strain (Tao et al. 2000). Sakakibara et al. 2001 applied a time resolved PIV technique to the measurement of an impinging jet and 3D ‘wall rib’ structures were visualized indicating the high production of vorticity at the merge of cross and wall ribs. Ganapathisubramani et al. 2006 performed a dual-plane PIV experiments which obtained the complete velocity gradient tensor and identified the hairpin vortex structures in a turbulent boundary layer.

The spatial resolution is an important factor in the visualization of 3D turbulent structures. Large scale three-dimensional vortical structures were obtained in the wake of a turbulent jet with 10η resolution by Hori & Sakakibara 2004. Steinberg et al. 2009 developed the orthogonal-plane cinema-stereoscopic PIV system to reconstruct the 3D vorticity structures with a resolution of 6η . The spatial resolution was further increased using cinematographic stereoscopic PIV to $2-3\eta$ (Ganapathisubramani et al. 2007, 2008). High temporal resolution was also achieved in the study of supersonic (Mach 2) turbulent boundary layer and the 3D hairpin structures were observed to be aligned with the streamwise direction (Elsinga et al. 2010). One of the primary goals of the present study

is the resolution of the fine-scale turbulent coherent structures with near Kolmogorov resolution and the time-resolved stereoscopic scanning PIV system was designed to visualize 3D structures with $0.6-0.83\eta$ grid separation.

1.4 Review of PIV techniques used in the study of turbulence

PIV is a non-intrusive optical technique that has been widely used over the last two decades and has seen a surge in recent years due to improvement in its components (cameras, lasers and computers) but also due to the development of new techniques based on PIV. Table 1.1 lists the different types of PIV systems applicable to the study of small-scale turbulence. Traditional PIV provides two velocity components in a plane which allows calculating four components of the velocity gradient. Also, the out of plane vorticity (Willert et al. 1991, Olsen & Dutton 2003) and the three components of the strain rate tensor can be derived. Kinetic energy dissipation rate can also be estimated with one velocity gradient by using isotropic assumptions (Saaernrinne & Piirto et al. 2000). Time-resolved PIV is also a planar measurement but compared to traditional PIV, it provides two in-plane acceleration components thanks to the high speed recording system. The acceleration can be used to estimate the dissipation rate in turbulence (Dahm & Southerland 1997) based on Taylor's hypothesis (Taylor 1935).

Stereoscopic PIV is a planar velocity measurement but it also provides the out-of-plane velocity component. Six components of the velocity gradient tensor can also be obtained with this technique which allows estimating the kinetic energy dissipation more accurately (Han et al. 2000 and Piirto et al. 2003). Mullin & Dahm 2006 introduced a

dual-plane stereoscopic PIV system to study the intermediate-scales of turbulence. The full nine velocity gradient components were obtained simultaneously in a plane of 15.5 mm \times 12.5 mm. This technique provided dynamic properties including energy dissipation rate, enstrophy and enstrophy production rate.

Of particular interest to the present work are those measurements that can be extended to three-dimensional space. Ganapathisubramani et al. 2007 applied a time-resolved stereoscopic PIV system to the study of a turbulent jet. Consecutive high speed PIV images were taken at the same plane and the Taylor's frozen hypothesis used to provide a quasi-instantaneous reconstruction of the vortical structures in a volume ($250\eta \times 160\eta \times 160\eta$) with an excellent resolution (3η) for the size of the volume observed.

As part of the present work (Cheng et al. 2011, Diez et al. 2011) a time-resolved scanning PIV system is developed to measure the small scales of the flow in a low Reynolds number turbulent jet. Scanning PIV combines conventional PIV with scanning techniques to obtain the two components of the velocity field in a set of light-sheet planes across a volume (Brücker 1997). For scanning frequencies adjusted sufficiently high compared to the characteristic time scale of the flow, the measurements can be considered as quasi-instantaneous over a scan cycle. Scanning systems have been used in the past for laser induced fluorescence measurements to obtain concentration and also velocity fields (Yip et al. 1988, Merkel et al. 1995, Dahm et al. 1992). The present scanning system is on the other hand used for particle image velocimetry measurements. As shown in Table 1.1, the time-resolved scanning PIV system also provides 3D volumetric measurements with two-

component velocity information, in comparison to 2D visualization using the dual-plane stereoscopic PIV system (Mullin & Dahm 2006). Six components of the velocity gradient and two components of the acceleration can also be derived.

The time-resolved scanning PIV was further expanded during the present work with a second camera resulting in a time-resolved stereoscopic scanning PIV (TR-SSPIV). This technique has been used by a limited number of researchers due to its high complexity. Burgmann et al. 2006 applied stereoscopic scanning PIV to investigate the structure and dynamics of vortices in a laminar separation bubble. The method was also applied to extract the large vortical structures present in turbulent jets (Hori & Sakakibara 2004). Nevertheless, the results are limited to vortex structures within scales far from the inner length scales due to the large volume used (i.e.: $100 \text{ mm} \times 100 \text{ mm} \times 100 \text{ mm}$) during the measurements.

The time-resolved stereoscopic scanning PIV (TR-SSPIV) system provides the three-component velocity field in a three-dimensional volume and it is time resolved. The complete nine-component velocity gradient tensor can also be simultaneously obtained, together with the three components of the acceleration. Vorticity, strain rate, enstrophy, kinetic energy and other important dynamic properties can be calculated with the 3D3C velocity information. The developed TR-SSPIV system is a tool to study the small-scales of turbulence, where the small coherent structures dominate the process of momentum, heat transport and energy dissipation. The TR-SSPIV system not only enables quantitative visualization of small-scale coherent flow structures, but also offers a true

measurement of the kinetic energy. It also provides statistical information that helps understand the physics of turbulence which could also be used for validating and improving numerical simulations.

1.5 Dissertation outline

As mentioned in the previous section, two different systems (time-resolved scanning PIV and time-resolved stereoscopic scanning PIV) are used to study the fine scales of turbulence. This dissertation focuses on the latter results from the TR-SSPIV system, since it provides simultaneously 3D3C velocity measurements. The detailed configuration and results for the time-resolve scanning PIV system can be found in Cheng et al. 2011 and Diez et al. 2011.

Chapter 2 provides the detailed description of the TR-SSPIV system including the implementation of the imaging acquisition and scanning system. Chapter 3 describes the free shear turbulent jets which will be investigated for the purpose of resolving the fine scales of turbulence. This chapter includes the experimental setup and flow conditions as well as the validation of jet velocity profile and discussion of the parameters that characterize turbulent motion.

Chapter 4 present quantitative visualization results in three-dimensional volumes. Structures of velocity, velocity gradients, and dynamic parameters such as enstrophy and dissipation rate are illustrated to show the coherent ‘building blocks’ of the flow structures of turbulence at the fine scales. A novel approach in vortex identification with

local pressure is introduced and compared with current identification schemes. Chapter 5 discusses the statistics of the fine scales in turbulence. The statistical analysis includes probability density function (PDF) of the velocity gradient, joint PDFs, and the energy spectrum of velocity gradients among other parameters studied. The accuracy of the measurements is discussed and a comprehensive comparison to published work is also included. Chapter 6 summarizes the results and emphasizes the main contributions of the current work.

Technique	Observation Area	Velocity Components	Velocity Gradient Components	Acceleration Components	Dynamic Properties
Traditional PIV	2D Plane	u, v	$\frac{\partial u}{\partial x}, \frac{\partial v}{\partial x}$ $\frac{\partial u}{\partial y}, \frac{\partial v}{\partial y}$	--	ω_z $\epsilon_{xx}, \epsilon_{yy}$ ϵ_{xy}
Time-resolved PIV	2D Plane	u, v	$\frac{\partial u}{\partial x}, \frac{\partial v}{\partial x}$ $\frac{\partial u}{\partial y}, \frac{\partial v}{\partial y}$	$\frac{\partial u}{\partial t}, \frac{\partial v}{\partial t}$	ω_z $\epsilon_{xx}, \epsilon_{yy}$ ϵ_{xy}
Stereoscopic PIV	2D Plane	u, v, w	$\frac{\partial u}{\partial x}, \frac{\partial v}{\partial x}, \frac{\partial w}{\partial x}$ $\frac{\partial u}{\partial y}, \frac{\partial v}{\partial y}, \frac{\partial w}{\partial y}$	--	ω_z $\epsilon_{xx}, \epsilon_{yy}, \epsilon_{zz}$ ϵ_{xy}
Dual-Plane Stereoscopic PIV	Two 2D Planes	u, v, w	$\frac{\partial u}{\partial x}, \frac{\partial v}{\partial x}, \frac{\partial w}{\partial x}$ $\frac{\partial u}{\partial y}, \frac{\partial v}{\partial y}, \frac{\partial w}{\partial y}$ $\frac{\partial u}{\partial z}, \frac{\partial v}{\partial z}, \frac{\partial w}{\partial z}$	--	$\omega_x, \omega_y, \omega_z$ $\epsilon_{xx}, \epsilon_{yy}, \epsilon_{zz}$ $\epsilon_{xy}, \epsilon_{yz}, \epsilon_{zx}$ $1/2 \omega_i \omega_i$ $\omega_i \epsilon_{ij} \omega_i$ $2\nu \epsilon_{ij} \epsilon_{ij}$
Time-resolved Stereoscopic PIV	Quasi-instantaneous 3D Volume	u, v, w	$\frac{\partial u}{\partial x}, \frac{\partial v}{\partial x}, \frac{\partial w}{\partial x}$ $\frac{\partial u}{\partial y}, \frac{\partial v}{\partial y}, \frac{\partial w}{\partial y}$ $\frac{\partial u}{\partial z}, \frac{\partial v}{\partial z}, \frac{\partial w}{\partial z}$	--	$\omega_x, \omega_y, \omega_z$ $\epsilon_{xx}, \epsilon_{yy}, \epsilon_{zz}$ $\epsilon_{xy}, \epsilon_{yz}, \epsilon_{zx}$ $1/2 \omega_i \omega_i$ $\omega_i \epsilon_{ij} \omega_i$ $2\nu \epsilon_{ij} \epsilon_{ij}$
Time-resolved Scanning PIV	3D Volume	u, v	$\frac{\partial u}{\partial x}, \frac{\partial v}{\partial x}$ $\frac{\partial u}{\partial y}, \frac{\partial v}{\partial y}$ $\frac{\partial u}{\partial z}, \frac{\partial v}{\partial z}$	$\frac{\partial u}{\partial t}, \frac{\partial v}{\partial t}$	ω_z $\epsilon_{xx}, \epsilon_{yy}$ ϵ_{xy}
Time-resolved Stereoscopic Scanning PIV	3D Volume	u, v, w	$\frac{\partial u}{\partial x}, \frac{\partial v}{\partial x}, \frac{\partial w}{\partial x}$ $\frac{\partial u}{\partial y}, \frac{\partial v}{\partial y}, \frac{\partial w}{\partial y}$ $\frac{\partial u}{\partial z}, \frac{\partial v}{\partial z}, \frac{\partial w}{\partial z}$	$\frac{\partial u}{\partial t}, \frac{\partial v}{\partial t}, \frac{\partial w}{\partial t}$	$\omega_x, \omega_y, \omega_z$ $\epsilon_{xx}, \epsilon_{yy}, \epsilon_{zz}$ $\epsilon_{xy}, \epsilon_{yz}, \epsilon_{zx}$ $1/2 \omega_i \omega_i$ $\omega_i \epsilon_{ij} \omega_i$ $2\nu \epsilon_{ij} \epsilon_{ij}$

Table 1.1. Comparison between current PIV techniques.

Chapter 2

Time-Resolved Stereoscopic Scanning PIV System

The present work successfully resolves the nine components of the velocity gradient in a three-dimensional volume simultaneously and as a function of time. With this information, the fine scales in a turbulent jet are resolved and the flow structures are visualized at those scales. To obtain these three-dimensional three-component (3D3C) velocity field information, a time-resolved stereoscopic scanning PIV system, TR-SSPIV, was designed, built and applied to the study of small scale turbulence for the first time. The system is able to provide flow information including velocity, velocity gradients, vorticity, rate of strain, and acceleration with Kolmogorov-scale resolution.

The design of the TR-SSPIV system is shown in Fig. 2.1. The main components of the time-resolved stereoscopic scanning PIV system include a high repetition laser, two high speed cameras, a synchronization unit, a computer, a series of optics and an oscillating mirror. The laser beam first passes through a set of spherical and cylindrical lenses and expands into a laser sheet. A rotating mirror is used to redirect the single laser sheet into a “fan” of laser sheets, which are passed through a spherical lens becoming parallel to each other and illuminating the observation volume. Two high speed cameras are focused on the same observation volume from two different angles (nearly 90 degrees from each

other). The observation volume is located at some distance downstream of the turbulent jet. A synchronization unit was used to communicate between the laser, scanning mirror and the two cameras.

The direct output of the TR-SSPIV system are PIV image pairs taken with the two cameras from two different angles at twenty different planes in the observation volume. The images at each plane are processed with INSIGHT 3G software by TSI, a PIV software that generate the three-component velocity fields from the images from the two cameras. The set of planar parallel three-component velocity fields obtained from scanning are reconstructed into a volume, to form a 3D3C velocity field. Further analyses were done to provide vorticity, energy dissipation and other statistical information about the turbulent flow at its fine scales. The detailed description of the system is presented in this chapter.

2.1 Image acquisition system

The configuration of the image acquisition system is shown in Fig. 2.1. The system consists of two high speed cameras (Photron Ultima APX) with 1024 pixels \times 1024 pixels resolution at 2000 Hz, an Nd-YAG 532 nm pulsed laser (Pegasus) with 10 mJ at 1000 Hz, and a synchronization unit with 1ns resolution. The pulsed laser, with a short duration of 3-5 ns, allows the camera images to ‘freeze’ the particle motion at a determined instance in time without producing a streaking effect typical of longer exposure illumination systems. The thickness of the laser sheet at the test section is kept at less than 1 mm to ensure proper spatial resolution.

By placing the two cameras at 30° from the laser-sheet, the images obtained maximize the overlapping viewing area between the two cameras and minimize the error in the calculation of the out-of-plane velocity component. To eliminate the out-of-focus effect on the images due to the perspective angles between camera and laser sheet, two scheinplugs are used between the cameras and their lenses which corrects the perspective angle. Camera lenses with 100 mm focal length are used at $f\#$ of 16 with a 0.5 m focus distance. For these lens conditions, the measured depth of focus is 14 mm, which is larger than the observed volume and ensures that all the PIV planes are in focus. A timing unit synchronized the laser, cameras, and the function generator that controls the scanning mirror. The Photron FASTCAM Viewer 3.2 software is used as the image acquisition platform with the images first stored in the camera (up to 1000 images per second) and then transferred to the computer.

2.2 Scanning light sheets characterization

While the three components of the velocity are obtained using a stereoscopic PIV arrangement, the three-dimensional volumetric information is achieved using a mirror system that scans the laser sheet through a volume. The Nd:YAG 532 nm laser generated a 3 mm diameter laser beam that passed through a spherical lens (1000 mm focal length), and a cylindrical lens (15 mm focal length) and it is redirected by the scanning mirror to generate a set of laser sheets as shown in Fig. 2.2. The cylindrical lens expands the laser beam vertically into a sheet while the first spherical lens creates a laser sheet waist at the test section, with an effective thickness of 0.9 mm. The silver coated oscillating mirror (6

mm \times 5 mm) is mounted on a GSI Lumonics VM500 galvanometer, and is controlled by a MiniSax modular driver that provides a maximum scanning angle of 25 degrees. To remove the divergence angle generated by the scanning mirror between contiguous laser sheets, a second spherical lens (500 mm focal length) is placed 500 mm after the mirror and makes the laser sheets parallel to each other.

The scanning mirror sweeps an angle α that is proportional to the driving voltage while the rotating speed of the mirror is controlled by the frequency from a function generator. Figure 2.3 illustrates the change in mirror angle by the input peak-to-peak voltage. The square symbols represent the experimental results which are fit by a straight line given by $\alpha = 0.0079V_{pp} - 0.0855$ with $R^2 = 0.9996$. In the present work, a 200 mV signal is used and the total scanned angle of the mirror is 1.43 degrees resulting in a 12 mm scanning width at the observation volume location.

The laser sheet thickness is an important characteristic of any PIV system which limits its resolution in the out-of-plane direction as well as the accuracy achievable by the measurements. Two methods are used to quantify the thickness as described by Cheng et al. 2011: (1) laser intensity distribution (power measurement), (2) particle distribution (particle count measurement). Both methods showed a good agreement. The first method involves traversing a knife edge across the laser sheet and collecting the transmitted light onto a photodiode detector. The knife edge is mounted on a traversing stage with 1 μ m accuracy. The knife edge is traversed from one side of the laser sheet to the other with at 50 μ m increments. The photodiode detector measures the intensity of the laser pulsing at

1000 Hz. Figure 2.4 shows the laser intensity profiles at different locations in the laser sheet. As shown in Fig. 2.4a, the laser power reaching the photodiode goes from 0 (when the knife edge blocks the laser beam completely) to a constant maximum near 8000 mV (when the knife edge allows the laser beam to pass freely). The laser power is then differentiated (central-difference) along the knife edge position and the resulting intensity profile is illustrated in Fig. 2.4b. The measurements are fitted with a first order Gaussian showing a good match with the results.

The second method used to calculate the laser sheet thickness is based on the number of detected PIV particles across the laser sheet. A knife edge slit, made with two sharp knife edges separated by 200 μm , is oriented vertically parallel to the incident laser sheet. It blocked most of the incident light except for the small portion of the laser sheet that passed through the slit. The knife edge slit is traversed along the laser-sheet-normal direction in 100 μm increment. The laser light that passed through the slit illuminated a water tank seeded with 10 μm diameter tracer particles. Particle images are taken of the still water in the tank at the same location where the jet measurements will be taken. Images are taken for each slit location. A MATLAB code is created to analyze the images and identify the number of tracer particles in each image. The detailed particle identification technique can be found in Cheng et al. 2010. Figure 2.5 shows that the particle distribution along the laser-sheet-normal also has a Gaussian profile, and it is equivalent to the laser sheet intensity profile measured previously.

These two methods to measure the laser sheet thickness are compared in Fig. 2.6, where the two profiles are normalized by their peak values. Both profiles are fitted with a Gaussian, and the $1/e$ value of each peak is used to determine the effective laser sheet thickness. The thicknesses are 0.94 mm and 0.96 mm for the laser intensity method and for the particle count method respectively. This thickness provided the appropriate spatial resolution in the out-of-plane direction for the measurements performed in the present work.

2.3 System timing and synchronization

One key aspect to this time-resolved stereoscopic scanning PIV system is the synchronization between the laser, the scanning mirror and the two cameras. A 50 Hz triangle wave with 200 mV peak-to-peak voltage (V_{pp}) is used to control the scanning mirror angle. Within one period of the triangle wave, the mirror rotated from $-\alpha/2$ to $\alpha/2$ and back to $-\alpha/2$, sweeping the laser sheet across the observation volume twice during its forward and backward motion. Therefore, the volume is scanned once every half period, and it takes 10 ms for the mirror to rotate from $-\alpha/2$ to $\alpha/2$ degrees. During every half period, the laser pulses 20 times at 500 μ s intervals, with each camera taking an image during each pulse. As a result, each volume contained 20 particle images taken at 20 equally spaced planes. Only the first half of each period is used for the present measurements.

To create a PIV image-pair, the images taken with each camera at the same plane (same scanning mirror angle) in adjacent volumes were used. The time delay between the two

images in a PIV image pair (Δt) can be changed by choosing images from different volumes. For instance, in Fig. 2.7a, Δt is 20 ms (one period of the signal) by pairing images from volume 1 and 2, and is 40 ms (two periods of the signal) by pairing images from volume 1 and 3. To get stereo results (i.e.: three components of the velocity) the PIV image pair from both cameras are combined through the stereoscopic calibration.

The PIV system uses two double exposure cameras synchronized with a double pulsed laser. To further explain the synchronization between these components, Fig. 2.7b shows a timing diagram for the two cameras, scanning mirror and laser for the first four images in a period. Fig. 2.7b shows that each camera shutter was opened twice (i.e.: frame 1A and 1B) with the same duration (500 μ s) during one synchronization period, and the laser was also pulsed twice with an initial delay of 250 μ s followed by a 500 μ s separation. This provided a sequence of images taken at 2000 frames per second with each volume containing 40 images (only the first half of each volume is saved). This setup provides continuous capturing of 3D3C velocity volumes and has an adjustable frequency and Δt suitable for PIV in different flow configurations.

2.4 Stereoscopic calibration

The stereoscopic calibration is a critical process for the TR-SSPIV system as it determines the accuracy of the out-of-plane velocity component. The calibration provides the mapping information to obtain the three components of the velocity from two PIV image pairs taken with two cameras from different angles. The schematic of the stereoscopic projection principle is sketched in Fig. 2.8. Briefly, the object plane (the

laser sheet plane) is defined with 3D world coordinates (X, Y, Z). When the object plane is being imaged, it appears on both left and right cameras in 2D image coordinates (x, y). As shown in the figure, the rectangular grids on the object plane are projected to the two image planes as warped grids. During the experiment, a calibration target with reference markers (dots) with known locations is used. For the present work, the calibration target has reference marks (dots) 0.5 mm diameter precisely spaced 3 mm apart on a planar acrylic glass with a fiduciary marker in the center, as shown in Fig. 2.9. The calibration target is set on a two-directional traverse stage and calibrations are obtained at five object planes in the measurement volume. The projection correlation can be derived for each object plane from geometric analysis assuming pinhole cameras, but the actual correspondence can be more complex due to the optical distortions and other image nonlinearities. But these distortions can be accounted for through additional optical corrections when the calibration target is used to increase the accuracy of the mapping parameters.

During the calibration process five calibration images are taken, one image is taken with the target plane at the laser sheet location, two more images are taken at 10 and 20 μm in front of the laser sheet and two more images are taken at 10 and 20 μm behind the laser sheet. These five calibration images are used to calculate a third-order mapping polynomial for one laser sheet location. The current stereoscopic scanning PIV system has 20 collimated laser sheets with 600 μm spacing. In total five mapping polynomial sets are obtained and each correlation set is used to map four adjacent planes. Last, particle images are taken when fluid stood still to perform disparity correction (Wieneke

2005). This process corrected any possible misalignments between laser sheet and target plane and thus increased the accuracy of the stereoscopic mapping.

2.5 Image processing procedure

The image processing algorithms extract the displacement information from particle images, obtain the three-component velocity fields and reconstruct the three-dimensional volumetric velocity field. The flowchart of the image processing procedure for the current study is illustrated in Fig. 2.10. The images are first processed via FFT cross-correlation algorithms in Insight 3G software (TSI Inc, MN, USA) to obtain 2D vector fields. The images are not pre-processed and are correlated with $24 \text{ pixel} \times 24 \text{ pixel}$ interrogation windows with 50% overlapped. There were approximately 15-20 particles in each interrogation window. Processing resulted in >99% good vectors, and is followed by a 3×3 local median validation filter to replace the few spurious vectors.

In each volumetric measurement set, both left and right cameras captured 20 pairs of particle images. Through the FFT cross-correlation, each image pair becomes a two-dimensional two-component 2D2C planar velocity field. The mapping polynomial obtained during target calibration is used to correlate the 2D2C planar velocity field from the left and right camera and produce a two-dimensional three-component planar velocity field. The position of the 20 2D3C planar velocity fields is known so they can be combined and reconstructed into a three-dimensional three-component volumetric velocity field. TR-SSPIV system enabled the true representation of 3D3C velocity information as well as its evolution in time.

Further analysis is done to calculate the nine-components of the velocity gradient and the three-components of the local acceleration using a second-order central difference schemes. The velocity gradient tensor is used to calculate the strain rate, vorticity, enstrophy, energy dissipation rate and other dynamic flow properties. Statistical analysis is done to study the probability density function (PDF) and spectrum of these flow parameters. The TR-SSPIV system's ability to provide the 3D3C volumetric velocity field and the instantaneous velocity gradient tensor will be used during the present work to study the fine-scale flow structures in a turbulent jet.

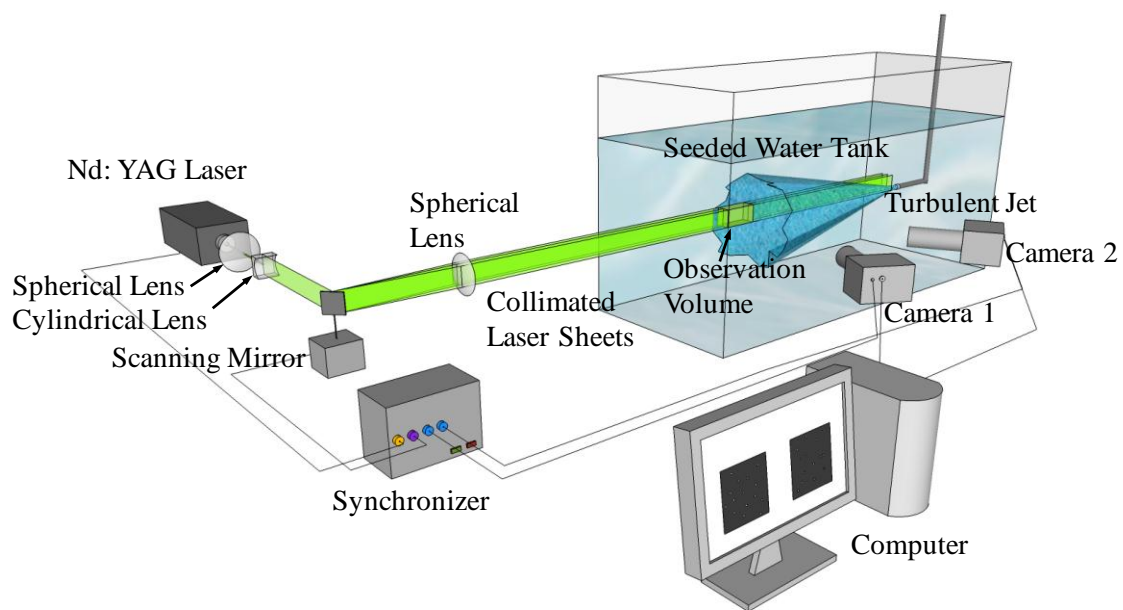


Figure 2.1. Layout of time-resolved stereoscopic scanning PIV system.

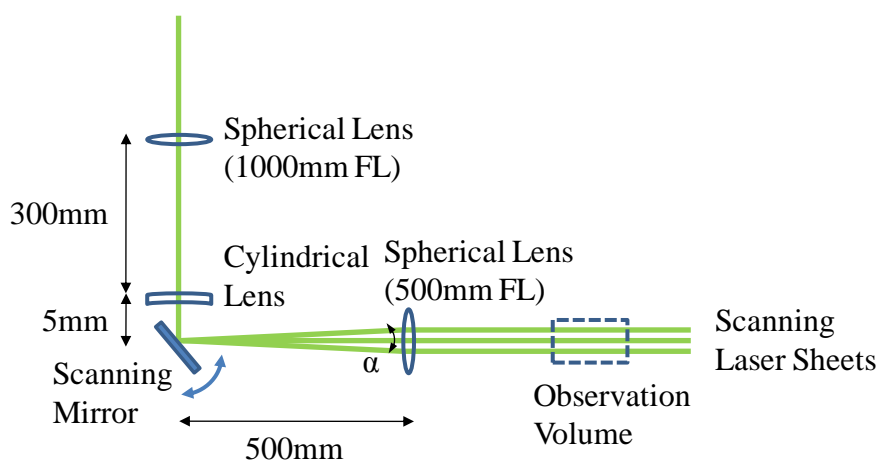


Figure 2.2. Layout of optical system used in the time-resolved stereoscopic scanning PIV system. A low-inertia galvanometric scanning mirror rapidly sweeps a vertical laser sheet horizontally through a small volume

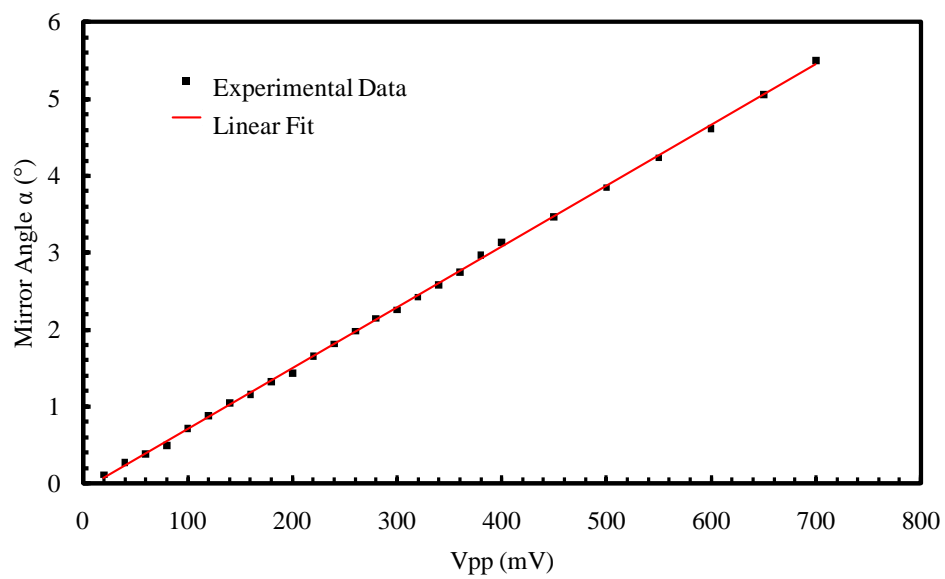


Figure 2.3. Calibration curve for rotating mirror. The angle of rotation α is linearly proportional to the input peak-to-peak voltage V_{pp} .

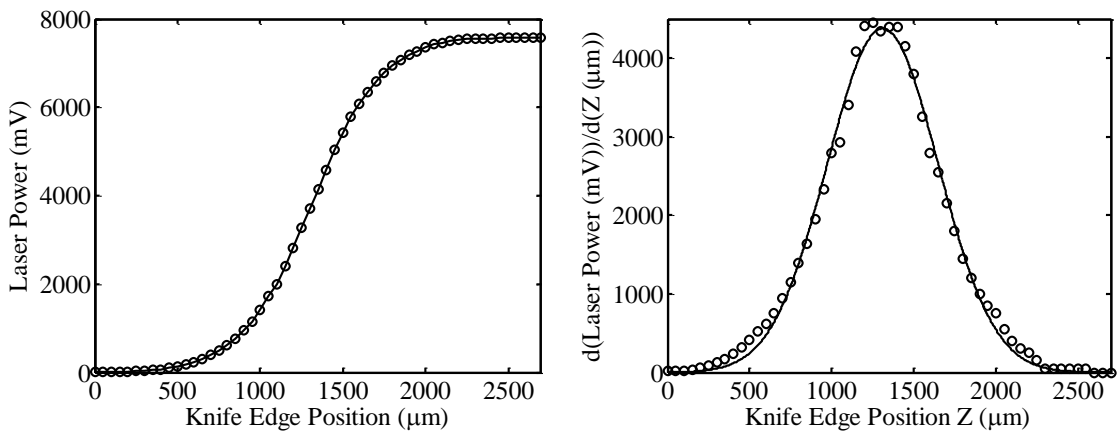


Figure 2.4. Typical results for laser sheet profile measurements normal to sheet direction, showing raw measured power values and error function fit (left), and corresponding derivatives giving sheet power profile and its Gaussian fit (right).

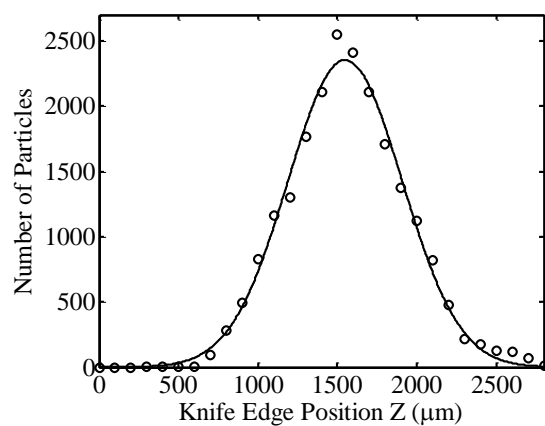


Figure 2.5. Typical result of number of particles that the camera detects across the laser sheet, showing raw measured number of particles (symbols) and Gaussian fit (line).

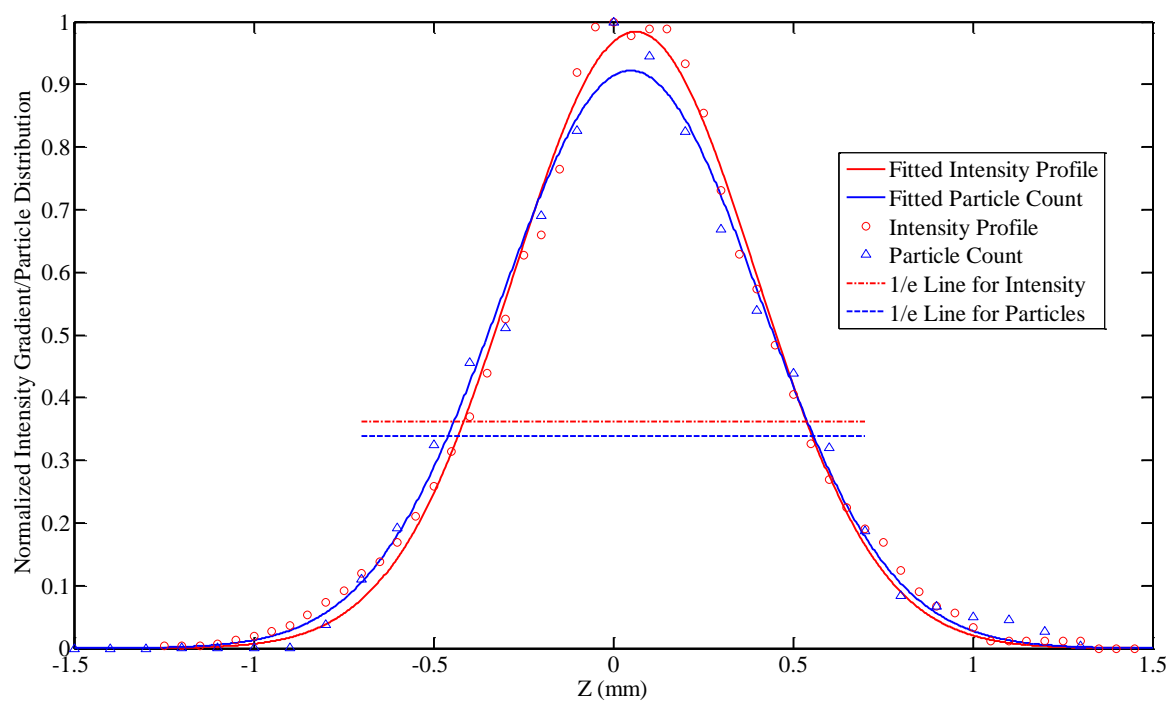


Figure 2.6. Normalized laser sheet intensity profile and normalized detected number of particles profile across the laser sheet. The 1/e value was used to quantify the sheet thickness. The two methods provide very similar results.

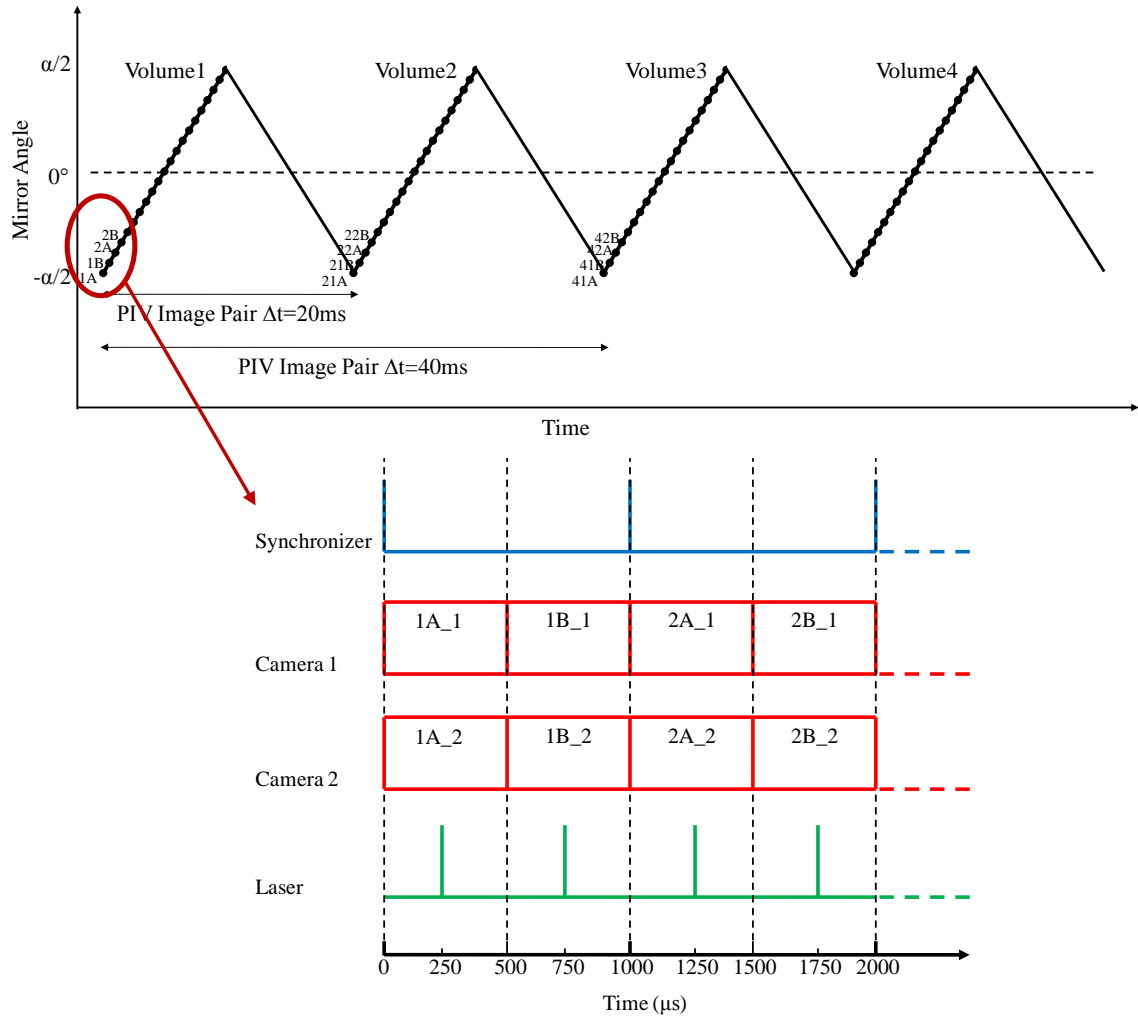


Figure 2.7. Timing diagram showing mirror position during PIV image acquisition for each volume (top), and camera exposure timing during laser pulse.

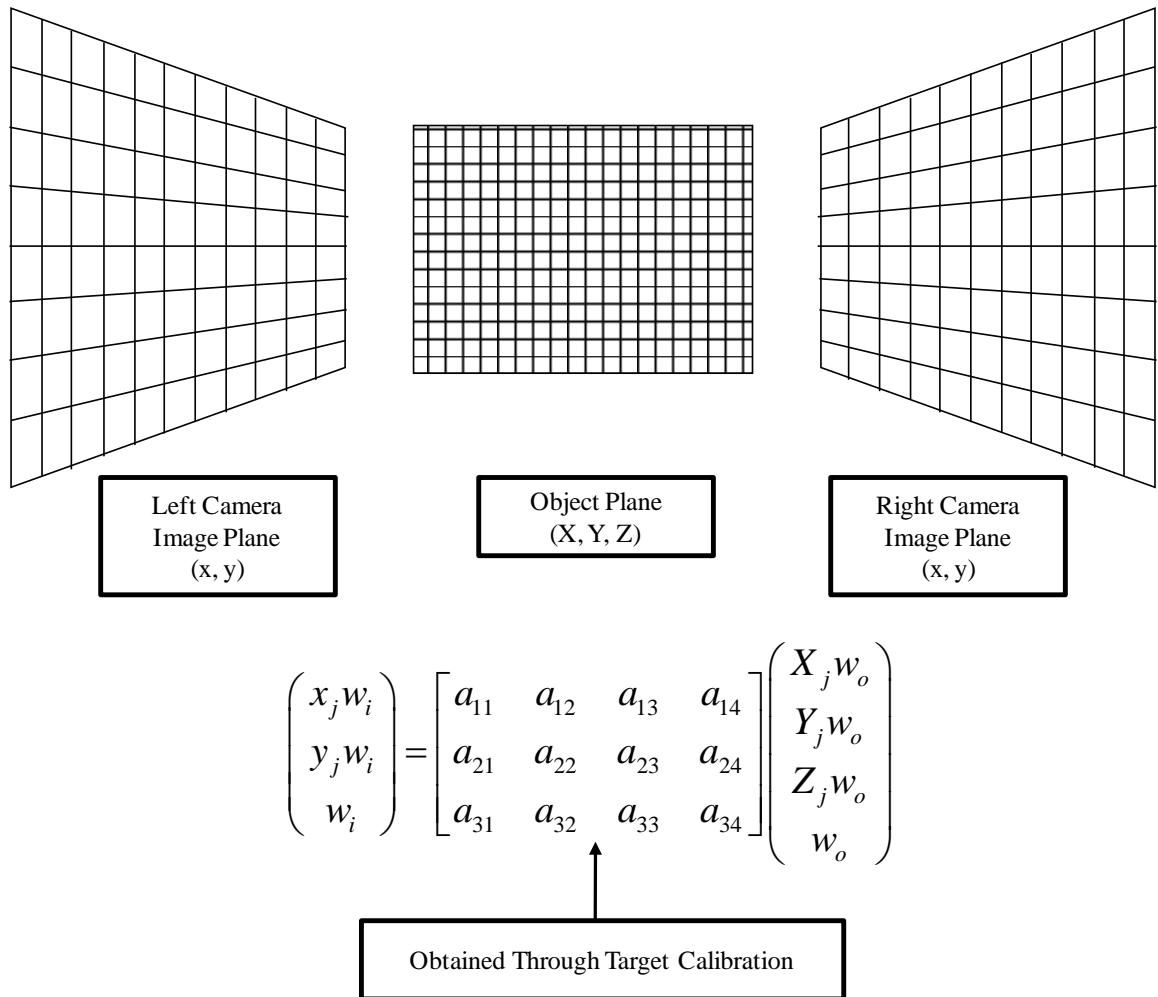


Figure 2.8. Schematic of stereoscopic projection principles.

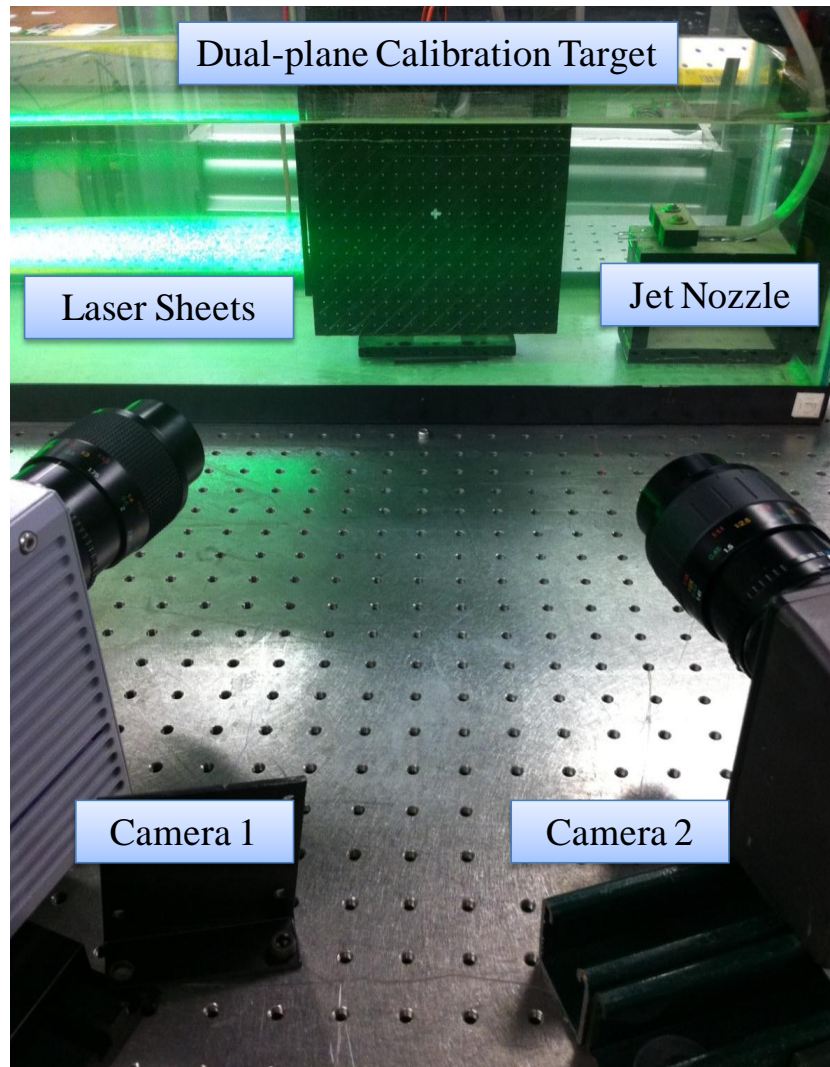


Figure 2.9. Picture of calibration target on a traverse stage.

Chapter 3

Free Round Turbulent Jets

Free round turbulent jets have been widely studied for their isotropic turbulence flow properties (along the centerline) and other basic turbulence characteristics. As mentioned in Chapter 1, the main purpose of the present work is to investigate the small scales of turbulence, visualize the fundamental three-dimensional ‘building blocks’ at those scales, and statistically study the energy dissipation within small eddies which are proportional to the Kolmogorov length scale. This chapter describes the experimental setup of the free round turbulent jet and the three different flow cases studied. Single planar PIV results are obtained to validate the turbulent jet behavior at both the exit and downstream location. The results are compared with published turbulent jet velocity and Reynolds stress profiles (Wynanski & Fiedler 1969, Panchapakesan & Lumley 1993, Hussein et al. 1994, Boersma et al. 1998). The main length scales in turbulent flows are also discussed emphasizing their physical significance and their use as non-dimensionalization parameters in the results chapters.

3.1 Experimental setup

The experiment is performed in a glass tank filled with distilled water with a water jet injected from a horizontal nozzle. The water tank had dimensions of 750 mm × 300 mm × 400 mm and the water level is kept at 300 mm as shown in Fig. 3.1. The side walls and the bottom of the tank are made of 3 mm thick glass panels to provide optical access for the scanning laser sheets and cameras. The tank contained distilled water that is kept at 21 °C and is seeded with silver coated hollow glass spheres as tracer particles. The mean diameter of the tracer particles was $10 \mu\text{m} \pm 2 \mu\text{m}$ and the density was 1.05-1.15 g/cm³. This type of particles is chosen for their small velocity lag in water and good light scattering capabilities for easy detection by the cameras.

In order to create the free turbulent jets without any buoyancy effect, the injection system for the jet is filled with the seeded water from the tank maintaining the temperature and particle concentration. The jet exits into the tank through a 5 cm long acrylic tube nozzle, with smooth 3.2 mm inner diameter, that is mounted horizontally. The jet is generated by a pulse-less syringe pump (Harvard Apparatus, PHD2000) with two 140 cc syringes. The adjustable injection flow rate allowed the generation of turbulent jets with different Reynolds number. A soft tube connected the nozzle and syringes and had a total length of 200 mm to ensure a fully developed flow at the exit.

As mentioned in §2.2, the measurement volume is illuminated by the sweeping laser sheet which enters the water tank from the wall opposite to the jet nozzle. Figure 3.1b shows a close-up view of the observation volume. It is located 480 mm ($x/D=150$)

downstream of the jet exit and is $31 \text{ mm} \times 15 \text{ mm} \times 12 \text{ mm}$ in size. The overlapping field of view (FOV) from the two cameras ($31 \text{ mm} \times 15 \text{ mm}$) is obtained with two 100 mm macro camera lenses that provided sufficient magnification to visualize the structure of the small scales of turbulence. The scanning laser system generates 20 laser sheet planes 0.9 mm thick spaced 0.6 mm apart resulting in a 12 mm observation volume width scanned in 10 ms. The small spacing between laser sheets is chosen to achieve a sufficient spatial resolution in the z -direction.

Two different camera orientation configurations are used in the present work. Figure 3.2 shows a sketch of the side-view and cross-view configurations. The main difference between the two configurations is the direction of the scanning laser sheets. In the side view configuration, the laser sheets are in the XY plane, parallel to the jet centerline, while in the cross view configuration, the laser sheets are in the YZ plane, scanning the cross-section of the jet. The two cameras are placed with at small angles facing the laser sheets. These two configurations are used to verify that the TR-SSPIV measurements are independent of the camera orientation while ensuring accuracy and repeatability.

3.2 Flow conditions

The present study of the small scales of turbulence examines a turbulent jet at two different Reynolds number, at two downstream locations and at two radial locations (jet centerline and off-axis). The three different flow conditions used in the TR-SSPIV measurements are shown in Table 3.1. Case 1 and 2 are taken at the same downstream location of the jet but the Reynolds number is doubled from Case 1 to Case 2. The

observation volume was at the centerline for both Case 1 and 2. Case 3 kept the same general flow condition as Case 1, but changed the measurement location closer to the jet exit ($x/D=80$) and at an off-centerline location at the shear layer at the edge of the jet.

3.3 Turbulent jet validation

The purpose of the turbulent jet validation is to verify that the generated jet in the present study satisfies the observed jet behavior previously reported in the literature. Planar PIV is used to investigate the velocity field at the jet exit and downstream in the jet. Measurements were obtained along the jet centerline at two downstream locations, one location is at the jet exit and the other at $x/D=40$. The velocity fluctuation and Reynolds stress terms are calculated and compared with classical work on round turbulent jets (Wynanski & Fiedler 1969, Panchapakesan & Lumley 1993, Hussein et al. 1994).

The radial profile of the jet velocity at the exit from the nozzle shown in Fig. 3.3 is obtained from 200 PIV images taken with a low speed PIV system (15 fps). This is the averaged jet velocity normalized by the nozzle inner diameter D . The velocity is symmetric with respect to the jet centerline and has a near flat-top profile right after the nozzle exit. The jet expands in the radial direction as it moves downstream and the streamwise velocity profile gradually becomes Gaussian. This behavior agrees with previous experimental work (Hasselbrink & Mungal 2001, Staack et al. 2010).

The jet is also investigated at downstream locations $x/D=40-75$ using a low speed (15 fps) stereoscopic PIV system. The mean \bar{u} velocity field is shown in Fig. 3.4 and is

obtained from the instantaneous velocity field from 20 independent sets of 50 image pairs each (1000 images total). The centerline velocity u_c is used to normalize the mean \bar{u} velocity and to compare the results at different local Reynolds number. The field of view for this test was $35D \times 24D$ with a $1\text{mm} \times 1\text{mm}$ resolution. Figure 3.5 shows both the streamwise u'_{rms} and radial v'_{rms} RMS velocity fluctuations fields. After normalizing by the centerline velocity u_c , both u'_{rms} and v'_{rms} are less than $0.25u_c$, with the u'_{rms} component showing the higher fluctuations. The mean velocity and RMS velocity fluctuation fields are symmetric with respect to the centerline of the jet. The normalized Reynolds stress $\overline{u'v'}$ field is shown in Fig. 3.6. It is antisymmetric with respect to the centerline of the jet and the values are comparable to Mullin 2002.

To further investigate the jet velocity behavior, the radial profile of the normalized mean streamwise velocity is shown in Fig. 3.7 for four downstream locations $x/D=40, 50, 60$ and 70 . The radial direction is normalized by the local streamwise position, r/x . Results are compared to previous experimental results obtained with hotwire anemometer (Wynanski & Fiedler 1969) and with laser-Doppler anemometry (Hussein et al. 1994). The streamwise velocity profiles for the different downstream locations collapsed into one after being normalized and matched previous published work as shown in Fig. 3.7.

The radial profiles of the streamwise (u'_{rms}) and radial (v'_{rms}) RMS velocity fluctuations at downstream locations $x/D=40, 50, 50$ and 70 are calculated and compared with DNS results (Boersma et al. 1998) and hotwire measurements (Panchapakesan & Lumley 1993) in Figs. 3.8 and 3.9. Both u'_{rms} and v'_{rms} radial profiles are symmetric with respect

to the jet centerline and are below 25% and 20% of the centerline streamwise velocity value. The streamwise RMS velocity fluctuation has two symmetric peaks off the centerline since the shear production of kinematic energy occurs there. The radial RMS velocity of the current data set shows smaller peak value than the DNS results (Boersma et al. 1998) but shows a better agreement with the experimental data (Panchapakesan & Lumley 1993). The radial profile of the Reynolds stress $\overline{u'v'}$ normalized by u_c is shown in Fig. 3.10. The profile is antisymmetric with upper and lower limits at ± 0.02 respectively. The results show excellent agreement with classical jet measurements (Wynanski & Fiedler 1969, Papanicolaou & List 1988 and Hussein et al. 1994).

The planar PIV measurements characterized the flow showing that it matches the typical velocity and velocity fluctuations profile observed experimentally and numerically in the literature. These results ensure that the small scale three-dimensional flow structures that will be obtained with the TR-SSPIV system are performed in fully developed round turbulent jet.

3.4 Scales of turbulent motion

A range of flow scales determined by eddy sizes can be found in all turbulent flows. Generally, the largest size eddies are responsible for most of the momentum transport and their sizes are comparable to the size of the flow, while the smallest size eddies are mainly affected by viscous dissipation. In the study of turbulent flows four main scales are commonly considered: the local outer scale (integral scale), the local inner scale (viscous scale), the Taylor microscale, and the Kolmogorov microscale.

The local outer scales of turbulent shear flows are the following: the outer length scale δ , given by the local flow width of the jet, the outer velocity scale u_c , given by the local mean centerline velocity of the jet, and the timescale τ_δ . For turbulent jets, δ and u_c are related to the downstream distance x from the jet exit, the density of the fluid, and the only invariant of the jet dynamic parameter, the local momentum flux J_o (Diez & Dahm 2007). These relations for round turbulent non-buoyant jets are:

$$\delta(x) = 0.36x, \quad (\text{Eqn. 3.1a})$$

$$u_c(x) = 7.2(J_o/\rho)^{1/2} x^{-1}, \quad (\text{Eqn. 3.1b})$$

$$\tau_\delta(x) = \delta(x)/u_c(x), \quad (\text{Eqn. 3.1c})$$

$$\text{Re}_\delta(x) = \delta(x)u_c(x)/\nu, \quad (\text{Eqn. 3.1d})$$

where the constants in Eq. 3.1 are obtained from Papanicolaou & List 1988. Also, the integral invariant associated with the flow is given by

$$J_o = \frac{\pi\rho U_o D^2}{4}. \quad (\text{Eqn. 3.2})$$

The local outer scales are often used to normalize flow parameters in turbulent jets since they characterize the structural and statistical flow properties and it is only affected by the downstream location (Mullin & Dahm 2006).

Unlike the local outer length scales, Kolmogorov microscales are the smallest scales in turbulent flows, where the viscous effects cannot be neglected and the energy is dissipated into heat. The mean dissipation rate of kinetic energy ε is given by

$$\varepsilon \equiv 2\nu \overline{S_{ij}S_{ij}}, \quad (\text{Eqn. 3.3a})$$

where S_{ij} is the rate of strain given by

$$S_{ij} = \frac{1}{2} \left(\frac{\partial u_i}{\partial x_j} + \frac{\partial u_j}{\partial x_i} \right). \quad (\text{Eqn. 3.3b})$$

The kinetic energy dissipation rate ε and the kinematic viscosity ν are used to define the Kolmogorov length, velocity and time scales (Kolmogorov 1941) as follows,

$$\eta \equiv (\nu^3 / \varepsilon)^{1/4}, \quad (\text{Eqn. 3.4a})$$

$$u_\eta \equiv (\varepsilon \nu)^{1/4}, \quad (\text{Eqn. 3.4b})$$

$$\tau_\eta = (\nu / \varepsilon)^{1/2}. \quad (\text{Eqn. 3.4c})$$

One of the goals of the present study is to obtain the three-dimensional flow structures with Kolmogorov-scale resolution in a turbulent jet.

The local inner (viscous) length scale is the largest length scale at which the eddies in turbulent flows are still strongly influenced by viscosity, but at the same time there is inertia from the local strain rate and equilibrium is achieved. This requires the inertia terms to be of the same order as the viscous term (Tennekes & Lumley 1972) giving by

$$\frac{\lambda_v}{\delta} : \text{Re}_\delta^{-1/2}. \quad (\text{Eqn. 3.5})$$

Also, the viscous length scale is proportional to the Kolmogorov length scale (Friehe et al. 1971) and given by

$$\lambda_v = 5.9\eta, \quad (\text{Eqn. 3.6a})$$

The corresponding time scale is then defined as

$$\tau_v \equiv \lambda_v^2 / \nu. \quad (\text{Eqn. 3.6b})$$

The viscous scales are used to nondimensionalize the velocity, velocity gradients, and higher order parameters throughout the present work with the goal of investigating the universality of the structures in turbulent free shear flow regardless of Reynolds number and other flow conditions.

In small scale eddies, the motions tend to be independent of orientation effects introduced by the flow itself at the large scales, and thus small scale turbulence are considered locally isotropic. In that case, the mean energy dissipation rate can be simplified to

$$\varepsilon = 15\nu \overline{\left(\frac{\partial u_1}{\partial x_1}\right)^2}. \quad (\text{Eqn. 3.7a})$$

Both Eqns. 3.3a and 3.7a will be evaluated in the present work to show the local isotropy of turbulent jets. Taylor 1931 defined the following length scale λ_g (transverse Taylor length scale)

$$\overline{\left(\frac{\partial u_1}{\partial x_1}\right)^2} \equiv \frac{u'^2}{\lambda_g^2}, \quad (\text{Eqn. 3.7b})$$

where u' is the RMS turbulence intensity given by

$$u' \equiv \left(\frac{1}{3} \overline{u_i u_i}\right)^{1/2}. \quad (\text{Eqn. 3.7c})$$

Alternatively, the longitudinal λ_f and transverse λ_g Taylor length scales can be expressed by

$$\overline{\left(\frac{\partial u_i}{\partial x_j}\right)^2}_{i=j} = \frac{2u'^2}{\lambda_f^2}, \quad (\text{Eqn. 3.8a})$$

$$\overline{\left(\frac{\partial u_i}{\partial x_j}\right)^2}_{i \neq j} = \frac{2u'^2}{\lambda_g^2}. \quad (\text{Eqn. 3.8b})$$

For isotropic turbulence, both Eq. 3.8a and 3.8b can be combined to give

$$\lambda_f = \sqrt{2}\lambda_g. \quad (\text{Eqn. 3.8c})$$

The Reynolds number based on the Taylor length scale is widely used in numerical and experimental studies to describe turbulent flows (Dimotakis 2005, Mullin & Dahm 2006, Ganapathisubramani et al. 2007 and Elsinga et al. 2010). The Taylor microscale Reynolds number is given by

$$\text{Re}_\lambda = \frac{u'\lambda_g}{\nu}. \quad (\text{Eqn. 3.9})$$

The present study uses the Taylor Reynolds number when comparing the results with previously published numerical and experimental work.

The parameters for the three cases studied are listed in Table 3.2. The resolution of the volume is given by the thickness of the laser sheet, 1.24η , and the interrogation window used $1.21\eta \times 1.21\eta$ (0.88×0.88 mm). Calculated velocity vectors are spaced 0.6η in the x - and y -directions and 0.83η in the z -direction (which corresponds to 0.6 mm separation between planes). The final measurement volume is $43\eta \times 20\eta \times 18\eta$ ($7\lambda_v \times 3\lambda_v \times 3\lambda_v$). In comparison, the two-dimensional field of view used in Mullin & Dahm 2006 was $12.5\lambda_v \times 10.1\lambda_v$ and the three-dimensional observation volume used in

Ganapathisubramani et al. 2008 was $1300\eta \times 160\eta \times 160\eta$ with a resolution of $3\eta \times 3\eta$. The small observation volume used in the present study increased the resolution to near-Kolmogorov scale resolution over previous studies allowing a close-up view of the flow structures that form the ‘building blocks’ in small-scale turbulence.

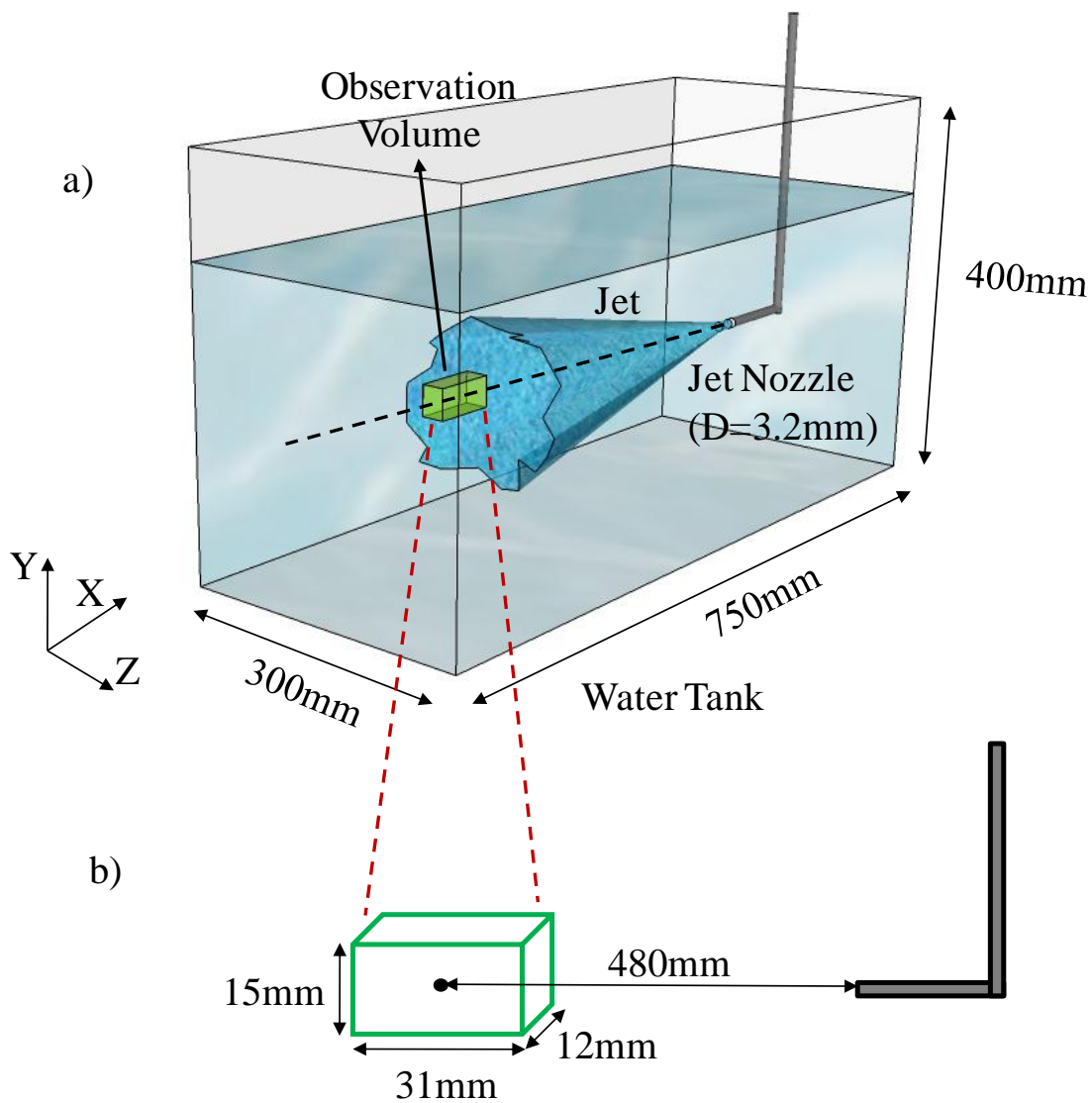


Figure 3.1. Sketch of the flow facility and laser illumination. a) Jet injected in a seeded water tank horizontally along x direction. b) Close up view of the observation volume showing size and location.

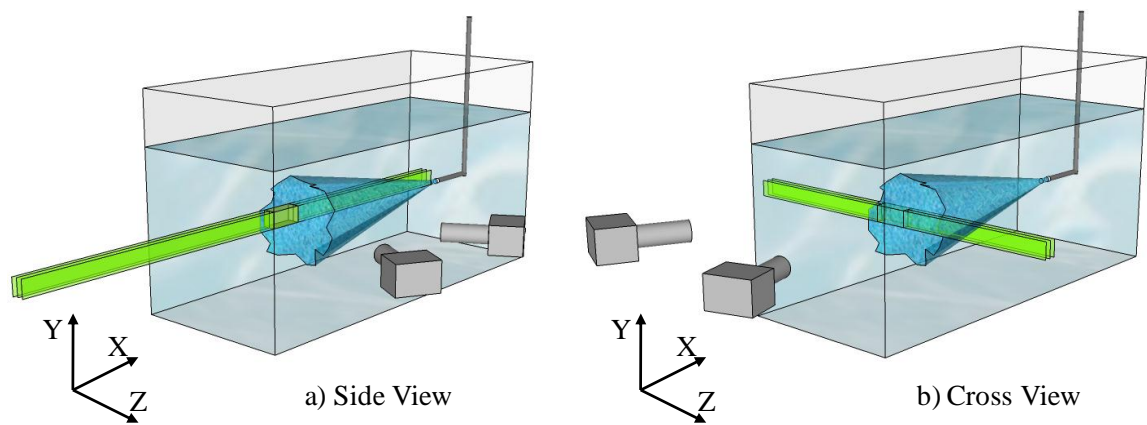


Figure 3.2. Sketch of the orientation of the laser sheet and camera with respect to the jet showing a) the side view, and b) the cross-sectional view orientation.

Parameter	Symbol	Unit	Value		
Temperature	T	°C	21		
Kinematic viscosity	ν	m ² /s	1.00472×10 ⁻⁶		
Density	ρ	kg/m ³	998		
Source diameter	D	mm	3.2		
			Case 1	Case 2	Case 3
Flow rate	\dot{Q}	ml/min	210	420	210
Exit velocity	U_o	m/s	0.4352	0.8704	0.4352
Source Reynolds number	Re_D	--	1386	2772	1386
Center of observation volume from jet exit	X	mm	480	480	256
Radial location of observation volume in terms of source diameter	r/D	--	0-4.6	0-4.6	0.6-5.2
Axial location of observation volume in terms of source diameter	x/D	--	145-155	145-155	75-85
Local jet centerline velocity	u_c	m/s	0.0185	0.037	0.0347

Table 3.1. Flow conditions of the three cases for the turbulent round jet measurements.

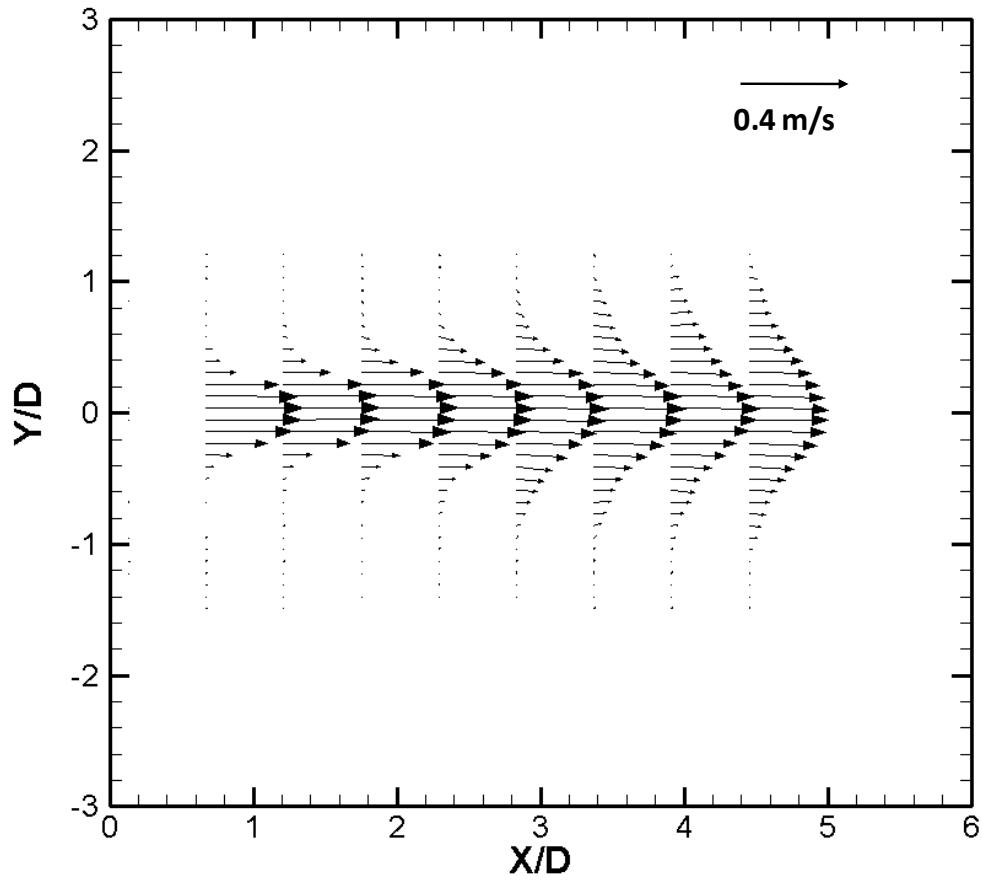


Figure 3.3. Radial profile of jet velocity at the exit, computed with 200 images from 10 independent sets.

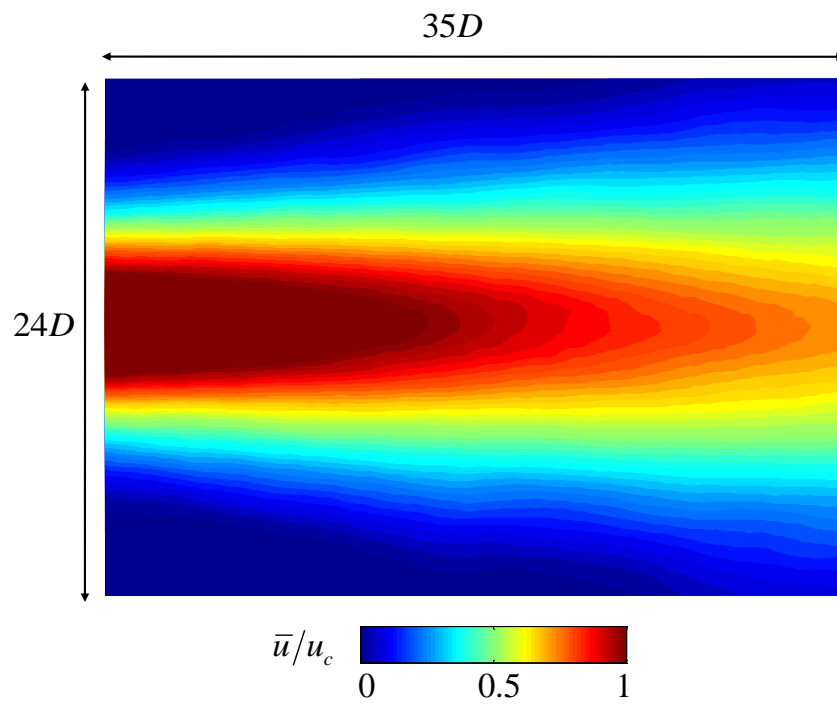


Figure 3.4. Normalized mean streamwise velocity contour at $x/D=40-75$ downstream of the jet exit. The mean was computed with 1000 planar PIV images.

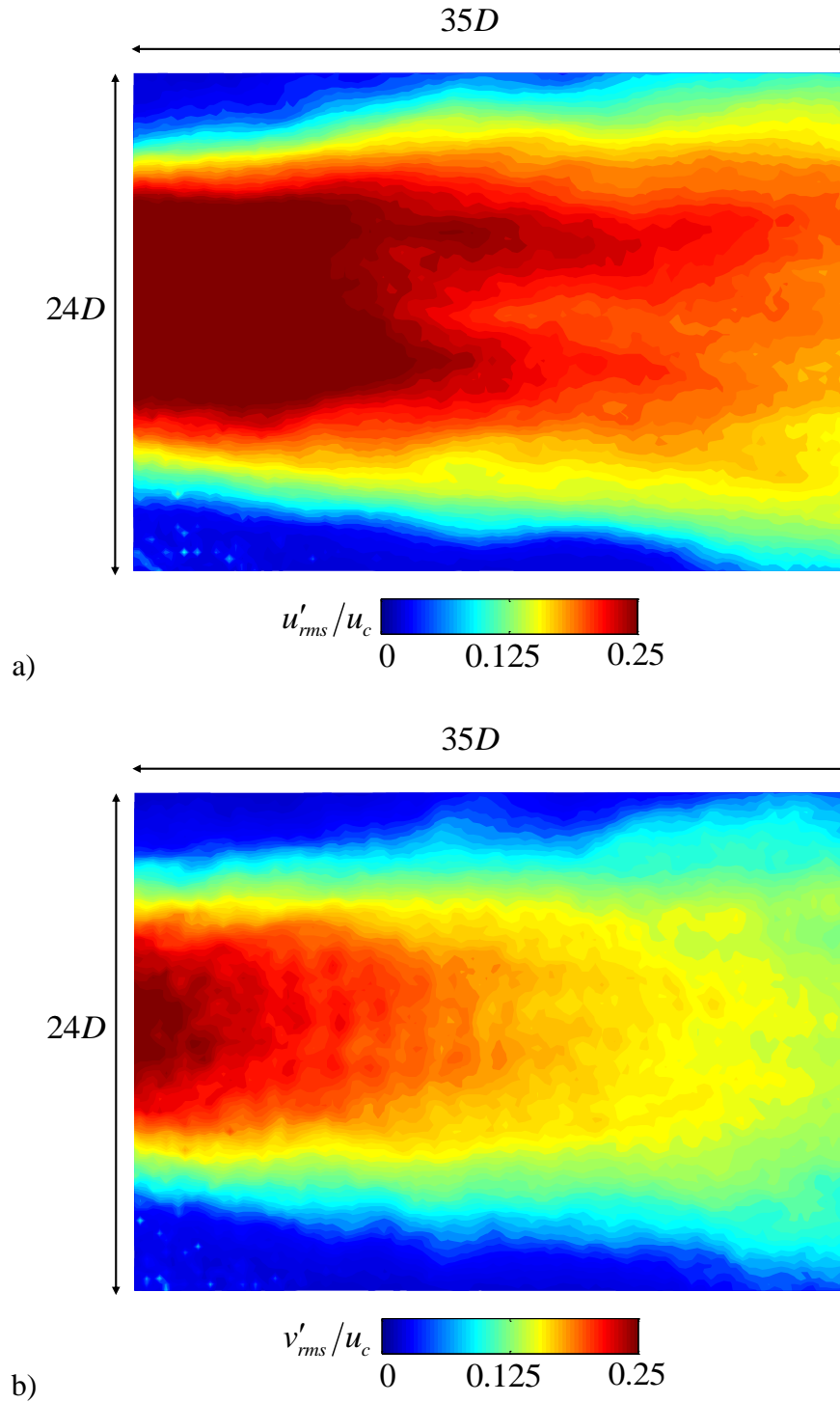


Figure 3.5. Contour plot of the normalized (a) streamwise and (b) radial rms velocity fluctuations at $x/D=40-75$ downstream of the jet exit.

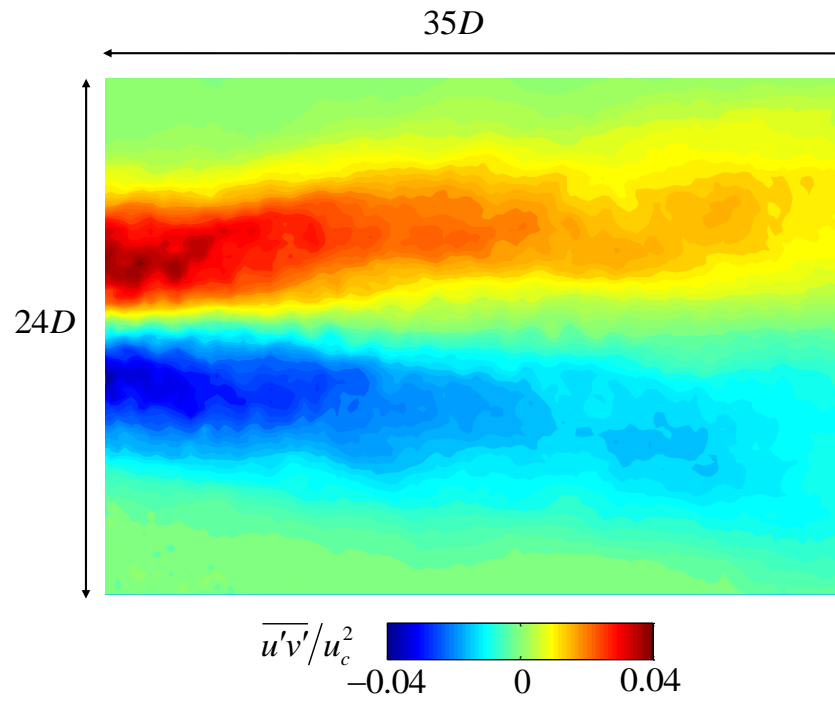


Figure 3.6. Normalized Reynolds stress term contour at $x/D=40-75$ downstream of the jet exit.

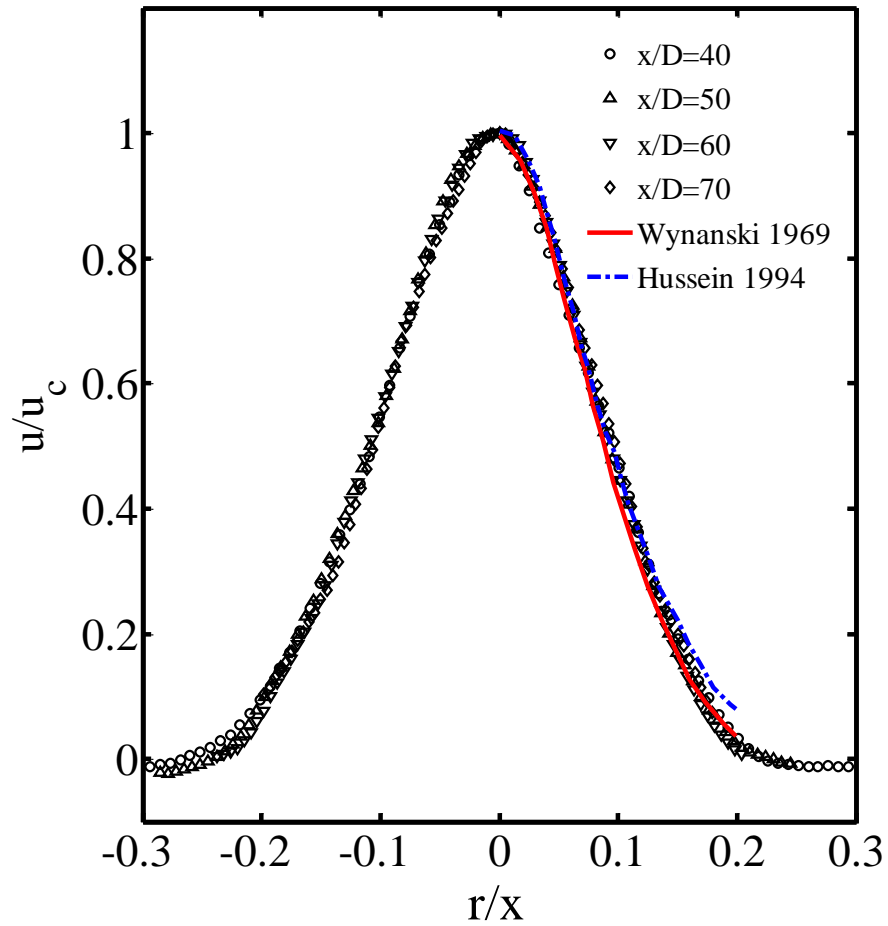


Figure 3.7. Normalized mean streamwise velocity profile at $x/D=40-70$ downstream of jet exit. The profiles at different downstream locations collapse into one and match with the experimental data from previous work (Wynanski & Fiedler 1969 and Hussein et al. 1994).

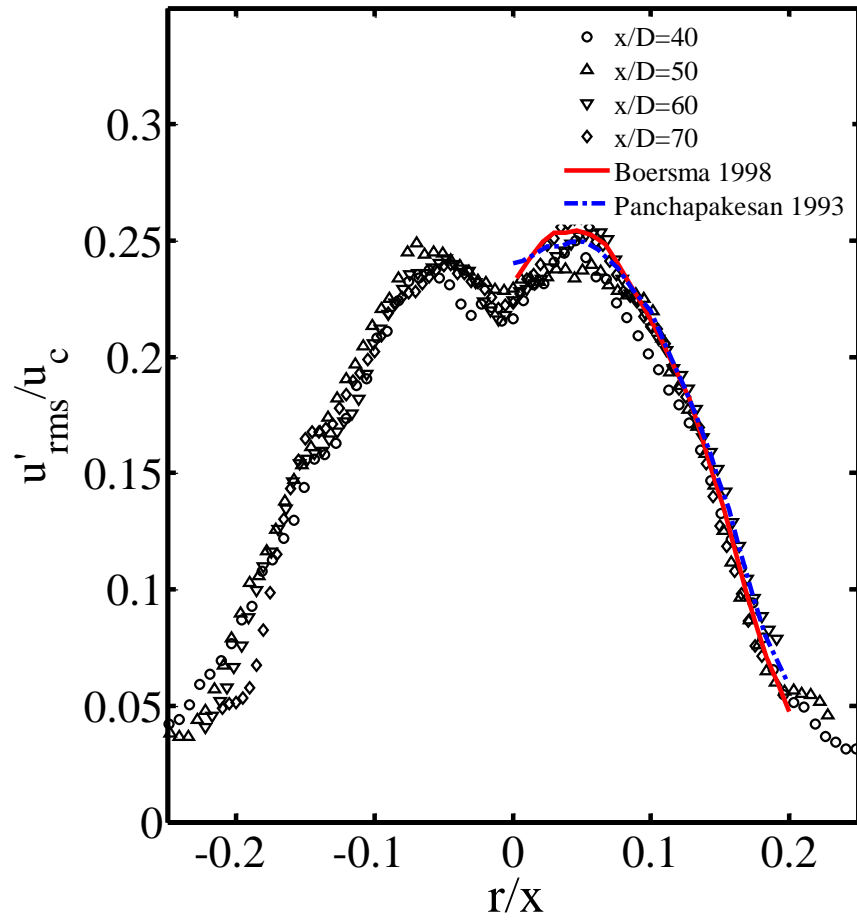


Figure 3.8. Normalized streamwise RMS velocity fluctuation profile at $x/D=40-70$ downstream of jet exit compared to DNS results (Boersma et al. 1998) and experimental results (Panchapakesan & Lumley 1993).

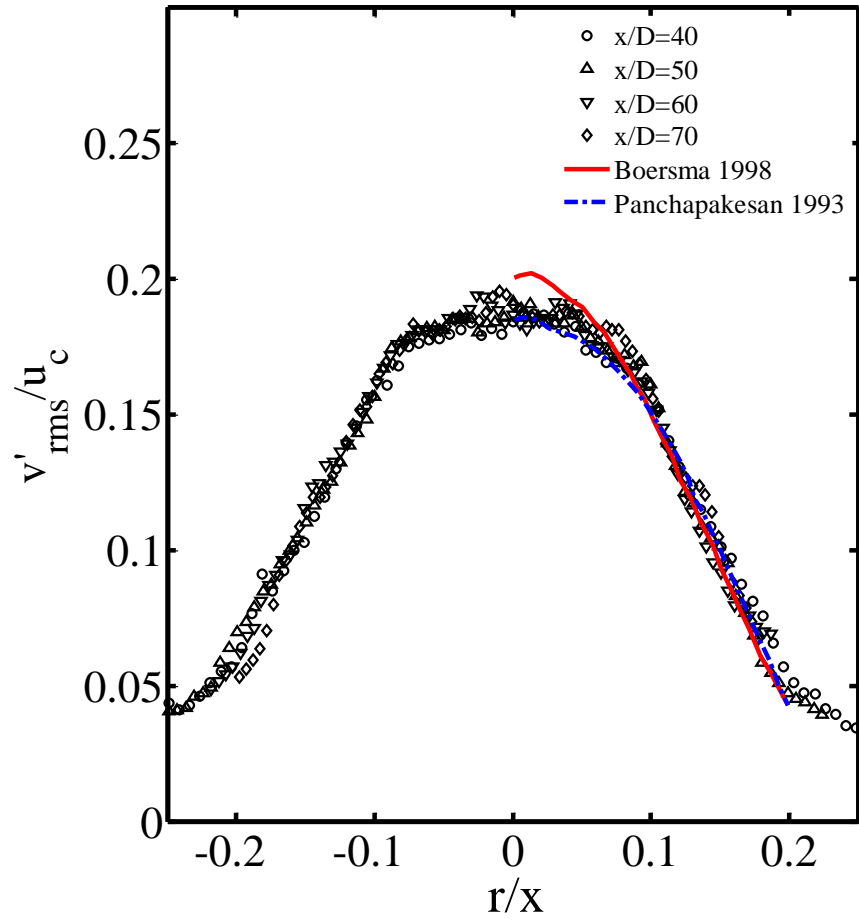


Figure 3.9. Normalized radial RMS velocity fluctuation profile at $x/D=40-70$ downstream of jet exit compared to DNS results (Boersma et al. 1998) and experimental results (Panchapakesan & Lumley 1993).

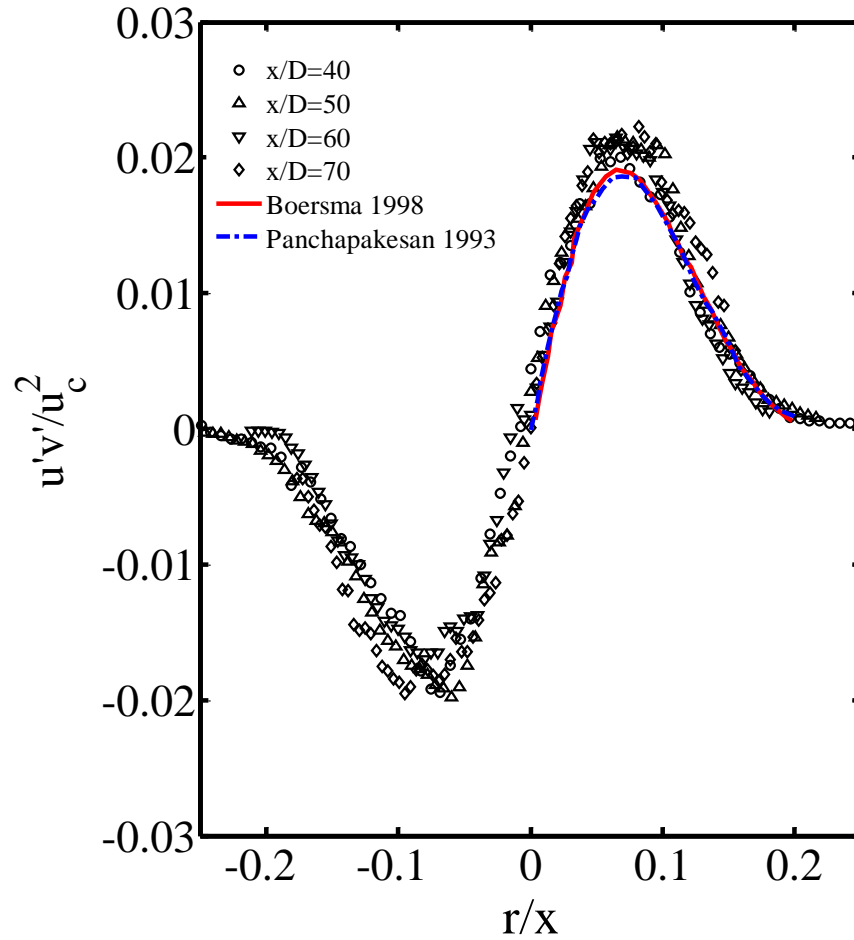


Figure 3.10. Normalized Reynolds stress term profile at $x/D=40-70$ downstream of jet exit compared to DNS results (Boersma et al. 1998) and experimental results (Panchapakesan & Lumley 1993).

Parameter	Symbol	Unit	Value	Value	Value
			Case 1	Case 2	Case 3
Momentum flux at jet exit	J_0	N	1.5×10^{-3}	6.1×10^{-3}	1.5×10^{-3}
Local outer length scale	δ	m	0.17	0.17	0.092
Local centerline velocity	u_c	m/s	0.019	0.037	0.035
Local outer Reynolds number	Re_δ	--	3200	6400	3200
Local outer time scale	τ_δ	s	9.3	4.7	2.7
Local mean dissipation rate	ε	m^2/s^3	2.9×10^{-6}	2.3×10^{-5}	3.6×10^{-5}
Kolmogorov length scale	η	m	7.7×10^{-4}	4.6×10^{-4}	4.1×10^{-4}
Kolmogorov time scale	τ_η	s	0.58	0.21	0.17
Local inner length scale	λ_v	m	4.5×10^{-3}	2.7×10^{-3}	2.4×10^{-3}
Local inner time scale	τ_v	s	20.4	7.2	5.8

Table 3.2. Scaling parameters of round turbulent jet for the three flow configurations.

Chapter 4

Visualization of Fine-Scale Flow Structures in Turbulent Jets

Resolving the extraordinary spatial and temporal complexity of turbulent flows has been a challenge for both numerical and experimental researchers. Direct numerical simulation (DNS) is computationally expensive especially at intermediate and small scales, while large eddy simulation (LES) is limited by the spatial resolution (Wallace 2009). On the other hand, few experimental approaches have simultaneously obtained the nine components of velocity gradient in a three-dimensional volume (Elsinga et al. 2010, Ganapathisubramani et al. 2008). Experimentally resolving these velocity gradients at the smallest scales of turbulent flows is of great importance since it provides true insight to the fine scale dynamics helping validate turbulence theories and numerical models.

The present study resolves the dissipation scales in a turbulent jet by measuring 3D3C velocity and nine-component velocity gradient. The primary goal is to investigate the fine scale coherent structures or ‘building blocks’ that contribute to the more complex turbulent behavior, as previously discovered by several numerical and experimental studies (Siggia 1981, Moisy & Jimenez 2004, Ganapathisubramani et al. 2008). To visualize and study the dynamics of these structures, the TR-SSPIV system is used to

measure the flow field of turbulent jets at different Reynolds numbers, downstream locations, and radial positions.

This chapter presents the quantitative visualization results of fine-scale turbulence in terms of velocity and velocity gradients, and dynamic parameters including rate of strain, vorticity, enstrophy, vorticity production rate and energy dissipation rate. Last, a novel approach is used to obtain the local pressure by solving the Navier-Stokes equation with the velocity and velocity gradient measurements. This approach introduces a new methodology to vortex identification, which has been studied previously using the Q criteria, Δ criteria and λ_2 criteria among others (Jeong & Hussain 1995, Chakraborty et al. 2005, Elsinga et al. 2010). Visualization of vortex with local pressure is presented and compared to other criteria.

4.1 Visualization of flow structure: velocity

Turbulent flows have complex three-dimensional velocity structures that classical planar PIV measurements cannot resolve. Time-resolved stereoscopic scanning PIV provides simultaneous 3D3C velocity fields. This allows visualizing the three-component velocity field in a volume using different visualization techniques such as surface contours, iso-surface groups, planar slices, 3D vector fields and streamlines to better understand the 3D turbulence structures.

The velocity magnitude ($|V| = \sqrt{u^2 + v^2 + w^2}$) contour plot is often used to represent the flow obtained with planar stereoscopic PIV (Mullin & Dahm 2005). With TR-SSPIV, the

planar velocity magnitude contour plot can be extended to surface contour plot in a 3D volume, as shown in Fig 4.1a. Furthermore, to visualize the velocity structures inside the volume, an iso-surface plot can be used (Fig. 4.1b). The velocity magnitude is represented by both the color scale and the 3D surfaces to help identify flow structures.

To visualize the typical velocity patterns in fine-scale turbulence, ten independent reconstructed volumes of instantaneous velocity magnitude are shown in Fig. 4.2. This figure shows the results from 3D2C velocity measurements obtained at $x/D=157$ downstream in a turbulent jet with the side-view time-resolved scanning PIV setup. The observation volume was at the center of the jet and the local Taylor-microscale Reynolds number (Re_λ) was 44. In these 10 different sets, the velocity magnitude varied along the x -direction (set 1 and 9), y -direction (set 3, 4 and 7), z -direction (set 8) or any other arbitrary directions (set 2, 5, 6 and 10). This indicates that at small scales, the turbulent structure can have any orientation. Figure 4.3 illustrates another ten independent sets of velocity structures taken at the same $x/D=157$ downstream location of the jet but using the cross-view time-resolved scanning PIV setup. Both PIV setups (i.e.: side-view and cross-view) provided similar results as shown in Fig. 4.2 and Fig. 4.3. The results also show that the velocity did not have a preferred direction, which suggest that the results satisfy the Kolmogorov's hypothesis of local isotropy.

As a result of the high temporal resolution of the TR-SSPIV system, the evolution of velocity structures in time can be obtained. Figure 4.4 illustrates a time sequence of the velocity field with increments of 20 ms between images. The flow pattern maintains the

same structure during at least 100 ms and it is convected along the x -direction with the streamwise velocity of the jet. The fact that the same geometries were tracked in time with a displacement of 5% the length of the observation volume in 5 time steps validates the temporal resolution of the TR-SSPIV system and demonstrates an accurate volume reconstruction from the set of scanning planes.

Further details about the flow can be obtained by visualizing the flow structures. These are represented using iso-surfaces in combination with contour plots. Figure 4.5a shows a typical instantaneous measurement volume of the velocity distribution. In this case, there is an increase in velocity in the x -direction and almost constant values in the y -direction. In order to extract other features of the flow, such as turbulent eddies, a Galilean decomposition (Ganapathisubramani et al. 2008) is used. This involves subtracting a convection velocity from the instantaneous velocity field. For instance, Fig. 4.5b shows the velocity field after a streamwise convection velocity $0.80u_c$ is subtracted from the local jet velocity. This process reveals, with the aid of selected streamlines, two structures in the observed volume, a tube-like structure and a sheet-like structure. A 2D velocity vector field close-up of the tube-like structure, shown in Fig. 4.5c, clearly reveals the presence of a small vortex. The velocity structures observed in Fig. 4.5 were common in the other independent data sets, as shown in Fig 4.2-4.3.

4.2 Visualization of flow structure: velocity gradient

The 3D3C velocity field obtained with the TR-SSPIV system allows resolving the nine components of the velocity gradient tensor simultaneously. The three components of the

velocity u_i were differentiated along the three directions x_j to obtain the nine-components of the velocity gradient $\partial u_i / \partial x_j$. Finite central-difference is used to calculate all the terms to achieve a higher accuracy with second order numerical error. The velocity gradients are plotted with iso-surfaces at chosen thresholds to reveal the ‘core’ of flow structures.

The choice of threshold for iso-surfaces plays an important role in separating complex structures to visualize simple fundamental shapes. Before choosing the threshold, the velocity gradient values were all normalized with their RMS values calculated from all the data sets. This enables a comparison of data sets with each other as well as with published results (Moisy & Jimenez 2004). Figure 4.6 illustrates the velocity gradient structure at different thresholds α , where $\alpha \equiv (\partial u_i / \partial x_j) / (\partial u_i / \partial x_j)'$. If lower thresholding values had been chosen, especially for $|\alpha| < 1$, the particular gradient structures observed can be fairly complex as they are formed from the merging of weaker strength individual shapes. On the other hand, if higher thresholding values are chosen, the structures identified maintain their shape, but get smaller and only their core is observed.

Additionally, even though the structures observed correspond to a particular instant in time, they maintain their shape for periods of time of the order of the Kolmogorov time scale as shown in Fig. 4.7. In this figure, two tube-like structures are convected downstream with only small observable changes in shape during $\Delta t = 400$ ms. This indicates that the flow structure visualization by using iso-surfaces with certain

thresholds is a reliable and consistent method. Meanwhile, it is interesting to note that the ability to track the trend of derived velocity parameters in time is another significant advantage of the TR-SSPIV system. This also enables the calculation of acceleration in the 3D volume, as presented in §4.3.

Some typical velocity gradient visualization results are shown in Fig. 4.8. The thresholding values of the normalized velocity gradients are $\alpha = \pm 1.5, \pm 2$. It should be noted that velocity gradients with a threshold above $1.5(\partial u_i / \partial x_j)'$ fill 11% of the volume, while those above $2(\partial u_i / \partial x_j)'$ fill 5% of the volume. Therefore, these values correspond to values close to the maximum velocity gradient levels observed from all the measurements taken. Incidentally, similar ratios (although in terms of vorticity) are used by Moisy & Jimenez 2004 and Jimenez et al. 1993 in the visualization of vorticity and dissipation structures.

For example, Fig. 4.8 shows the iso-surfaces of the six velocity gradients for one of the more feature-rich data sets taken with the 3D2C single camera scanning PIV measurements. They reveal simple geometrical shapes such as sheets (Fig. 4.8d), tubes (Fig. 4.8a, c, and e), square ribbons (Fig. 4.8f) and also spherical blobs (Fig. 4.8d). Similar individual shapes corresponding to vorticity structures have also been observed in DNS simulations (Moisy & Jimenez 2004). The size of these basic shapes ranged from $1.5-5\eta$ for the core of the tube or thickness of a sheet, to $20-30\eta$ for the length of a tube or sheet. More complex structures, formed from “individual blocks”, extended beyond

the observation volume and could not be sized. Also, if lower threshold values are chosen, more of the particular gradient structures are exposed which corresponds to complex structures formed from the merging of weaker strength individual shapes.

Another example taken with the 3D3C TR-SSPIV measurements shows the iso-surfaces of the nine velocity gradients in Fig. 4.9. To compare the strength of each velocity gradient component, the values are normalized by the viscous length scale ν/λ_v^2 . As shown in Fig. 4.9, the nine velocity gradients have structures varying in shape and strength. While previous studies focus solely on the strain rate or vortex structures (Vincent & Meneguzzi 1991, Ganapathisubramani et al. 2008, Elsinga et al. 2010), the current measurement results present the structure of individual components of velocity gradients. This shows that the ‘worm’- like or ‘sheet’-like shapes of vortex structures, as visualized by Ganapathisubramani et al. 2008 and Elsinga et al. 2010, are composed of different velocity gradients with simple shapes. In this example, $\partial u/\partial y$ and $\partial v/\partial x$ are the dominating components out of all nine and they are responsible for the vortex structures explained in §4.5. The results are comparable to Mullin & Dahm 2006, where the full nine components were presented. However, unlike the planar representation from their dual-plane stereoscopic PIV system, the TR-SSPIV system provides the full three-dimensional velocity structures and therefore offers a more accurate determination of the shapes of these structures.

The next example of velocity gradients shows intense structures detected that are over three times the RMS values. Two cases of strong velocity gradient peaks are represented

by iso-surfaces in Fig. 4.10a & b. They show two basic shapes, a tube-like structure in Fig. 4.10a and spherical blob structures in Fig. 4.10b, with dimensions, $10-20\eta$, in agreement with DNS simulations (Ishihara et al. 2009). These two volumes are the only ones that have strong flow structures out of the 10 individual data sets taken at the same condition, which means high strength vortex structures are rare. The streamlines shown indicate a good correlation between the velocity and the specific velocity gradient.

4.3 Visualization of flow structure: acceleration

As a result of the high temporal resolution of the high speed system, local acceleration at each grid point in the observation volume can be calculated using second order central difference from three adjacent volume data. Figures 4.11a & b illustrate the 3D iso-surfaces of the two local acceleration terms $\partial u/\partial t$ and $\partial v/\partial t$. Surprisingly, the features of the local acceleration $\partial u/\partial t$ and $\partial v/\partial t$ correlate very well with the convective acceleration $u\partial u/\partial x$ and $u\partial v/\partial x$ shown in Figs. 4.11c & d. In fact, they have nearly the same structures yet with opposite values. This anti-alignment phenomenon can be explained by the random Taylor hypothesis summarized by Tennekes 1975.

The total fluid particle acceleration is defined as:

$$Du_i/Dt \equiv \partial u_i/\partial t + u_j \partial u_i/\partial x_j, \quad (\text{Eqn. 4.1})$$

where $\partial u_i/\partial t$ is the local acceleration at a fixed reference point and $u_j \partial u_i/\partial x_j$ is the convection acceleration due to the bulk movement of the flow. Random Taylor hypothesis suggests that the total (Lagrangian) acceleration of a fluid particle in isotropic

turbulent flow is considerably small so that it can be treated as $Du_i/Dt = 0$. This hypothesis has previously been proven by DNS study (Tsinober et al. 2001). In the current measurements, jet centerline was along x -direction, and thus streamwise velocity u is much larger than the other two radial components v and w , which makes $u\partial u_i/\partial x$ the dominating term in the convective acceleration. Therefore, the behavior of the local acceleration structures nearly cancelling the convective ones is observed in Fig. 4.11. The measurement from TR-SSPIV system provided an experimental proof of the random Taylor hypothesis in isotropic turbulence.

4.4 Visualization of flow structure: vorticity and strain rate

Once the 9 components of the velocity gradient tensor are obtained, other important parameters including vorticity, rate of strain, enstrophy, enstrophy production rate and energy dissipation rate can be derived. The visualization of these parameters is another step towards understanding the basic ‘building blocks’ of small-scale turbulence and were traditionally only available through numerical simulations (Siggia 1981, Jimenez et al. 1993, Moisy & Jimenez 2004). Recent experiments have resolved the 3D structures of the large scales in the flow (Sakakibara et al. 2001, Elsinga et al. 2006) and also resolved the intermediate-scale of turbulence (Ganapathisubramani et al. 2008 and Elsinga et al. 2010). The current work intends to resolve the smallest scales with a 0.8η resolution in $43\eta \times 20\eta \times 18\eta$ volumes and observe the interaction between rate of strain and vorticity at close-up views.

Having calculated the nine velocity gradient components, the rate of strain tensor is directly given by

$$\varepsilon_{ij} \equiv \frac{1}{2} \left(\frac{\partial u_i}{\partial x_j} + \frac{\partial u_j}{\partial x_i} \right), \quad (\text{Eqn. 4.2})$$

The normal strain rate components, ε_{xx} , ε_{yy} , ε_{zz} , are the same as the diagonal velocity gradient components and were shown in Fig. 4.9. The shear rate components, ε_{xy} , ε_{xz} , ε_{yz} , are normalized by the viscous scale and shown as contour plots in Fig. 4.12. These results in Fig. 4.12 can be directly compared with the 2D contour plots in Fig. 7 in Mullin & Dahm 2006. The nondimensionalized rate of strain appears to be less intense than in Mullin & Dahm 2006, probably due to the higher Reynolds number they used. However, the width of the structures is in the same range ($2-3\lambda_v$) in both studies, which shows the universality of small-scale turbulence structures regardless of Reynolds number or other flow conditions.

To visualize the intense structures in the flow, iso-surfaces of the rate of strain components are shown in Fig. 4.13. The component ε_{xy} is the most intense and has a tube-like shape, which contributed the most to the energy dissipation rate discussed in more detail later. In comparison, the component ε_{zx} had a blob-like structure (this structure is also represented as a contour plot in Fig. 4.12). A comparison between Figs. 4.12 and 4.13 shows the effectiveness of the thresholding iso-surface representation technique to obtain the 3D shapes of the rate of strain.

Having calculated the nine velocity gradient components, the three vorticity components can also be derived. They are plotted in Fig. 4.14 and given by

$$\omega_i \equiv \frac{1}{2} \left(\frac{\partial u_j}{\partial x_i} - \frac{\partial u_i}{\partial x_j} \right), \quad (\text{Eqn. 4.3})$$

From the three components of the vorticity field for the particular instant of the flow shown in Fig. 4.14, the ω_z component is the most intense one and its 3D structure has a tube-like shape. Surprisingly, this structure appears to be very similar to that of the rate of strain component ε_{zx} , so both of them are illustrated in the same graph in Fig. 4.15. These two similar shapes are very closely spaced as if they interact with each other. This pairing of rate of strain and vorticity has been reported in numerical studies (Kida & Ohkitani 1992, Pradeep & Hussain 2006) as well as experimental studies (Ganapathisubramani et al. 2008). To help visualize the flow behavior where the strong vorticity and rate of strain occurs, the relative velocity field (instantaneous velocity field subtracted from the mean velocity field) is also shown. In this case, a ‘focus’ type of vortex occurs at the location of the intense tube structures. More details about vortex identification techniques are described in the next section.

To investigate the energy dissipation mechanisms at the viscous length scales in turbulence, the enstrophy is calculated. This is the integral of the square of vorticity,

$\frac{1}{2} \omega \cdot \omega$, and is often used to describe the kinetic energy that corresponds to dissipation.

The enstrophy is illustrated in Fig. 4.16a, where it is calculated from the vorticity components in Fig. 4.14. For this particular instant of the flow, the enstrophy has an intense core in the center of the volume. The 3D shape is similar to the vorticity

component ω_z , since this component was the most intense. Third order velocity gradient parameter, the enstrophy production rate $\omega_i \varepsilon_{ij} \omega_j$, is the result from local stretching of vortex rings by the rate of strain tensor. Figure 4.16b and 4.17b show the enstrophy production rate, which has a dominating positive value and the magnitude is consistent with work by Mullin & Dahm 2006, showing its universality at the smallest scales.

Critical to the study of the fine-scale turbulence is the accurate calculation of the energy dissipation rate $2\nu\varepsilon_{ij}\varepsilon_{ij}$. This is used to define the Kolmogorov scale and is related to the effectiveness of energy passing from large eddies to smaller ones. During the present work, the energy dissipation rate was directly calculated and the typical instantaneous 3D structures were represented in Fig 4.16c and 4.17c. For instance, the iso-surfaces shown in Fig 4.17c have a value two times the calculated mean energy dissipation rate and they reveal the location where intense dissipation occurs. Without the 3D3C velocity measurements, energy dissipation rate can only be estimated through local isotropy theories or experimental correlations. Our approach provides a true representation of turbulent kinetic energy dissipation rate with high spatial and temporal resolution and is compared with other work where different isotropy assumptions were used (Friehe et al. 1971, Tanaka & Eaton 2007, Saarenrinne & Piirto 2000, George & Hussein 1991) in §5.7.

4.5 Vortex identification

The presence of three-dimensional vortex structures is one of the most significant characteristics of turbulent flows and many vortex identification criteria have been established to isolate vortex structures from the low turbulence background flow. However, there is still no universal definition to extract them (Jeong & Hussain 1995, Chakraborty et al. 2005). Table 4.1 lists a brief description of the most well-known criteria, as well as a proposed pressure criterion that has originated as part of the present study.

Enstrophy, the square of vorticity, is the most common way to define strong vortex cores (Hussain & Hayakawa 1987, Jeong & Hussain 1995). However, the high enstrophy criterion does not always identify vortex cores successfully especially when strong shear is involved or high vorticity sheets occur. Figure 4.18 is an example of a typical instantaneous enstrophy field visualized using iso-surfaces. For clarification, velocity streamlines and contours are also included showing that the high enstrophy structure in the center of the volume represents a ‘focus’ type vortex core. Moreover, the iso-surfaces on the left side of the volume show a ‘saddle’ type vortex. In another example shown in Fig. 4.19 of a typical instantaneous enstrophy field visualized using iso-surfaces, the vorticity field is shown as contours to help identify the vortex. While the high vorticity magnitude successfully reveals a vortex core on the top right, the other high magnitude region on the bottom right appears to be a sheet-like structure and does not characterize a vortex core. This suggest that although high enstrophy structures can help identify vortex

cores in small-scale isotropic turbulence, more sophisticated criteria are needed to characterize vortices in broader circumstances.

Another method to identify vortex structures is the Q criterion, proposed by Hunt et al. 1988, is defined as the second invariant of the velocity tensor using

$$Q = \frac{1}{2} (\|\Omega\|^2 - \|S\|^2), \quad (\text{Eqn. 4.4})$$

where $\|S\| = [\text{tr}(SS^T)]^{1/2}$ and $\|\Omega\| = [\text{tr}(\Omega\Omega^T)]^{1/2}$. The Q criterion detects vortices using $Q > 0$, which is a balance between high vorticity and high strain rate. Figures 4.20b, 4.21b, and 4.22b illustrate three different cases of vortex structures identified using the Q criterion. The Q iso-surfaces appear similar to the enstrophy ones but in general they are smoother. For instance, in Fig. 4.21a, the structure identified by the enstrophy is composed of multiple elements but in Fig. 4.21b, the structure identified by the Q criterion is a single element with a smooth surface. Although the structure does not have a uniform cross section, it is still considered as tube-like structure due to the fact that the vortex core is aligned along the tube.

Another method to identify vortex structures is the λ_2 criterion introduced by Jeong & Hussain 1995 to detect the local pressure minimum region in a plane perpendicular to the vortex axis. The intermediate eigenvalue λ_2 ($\lambda_1 \geq \lambda_2 \geq \lambda_3$) of the symmetric tensor $S^2 + \Omega^2$ is used to define the vortex core as ‘a connected region with two negative eigenvalues’, which means $\lambda_2 < 0$ within the vortex core. Figures 4.20c, 4.21c and 4.22c

show three examples of structures identified by the $\lambda_2 < 0$ criterion. The λ_2 criterion gives similar results to the Q criterion, but with a smaller boundary in general. This is expected since the λ_2 criterion captures the pressure minimum in a plane and is more restrictive criterion compared to the Q criterion. However, in other circumstances such as in Fig. 4.22c, the λ_2 criterion may not be suitable to define the vortex core, especially when the local pressure difference is small, since this criterion neglects the irrotational straining and viscous terms in the Navier-Stokes equation.

Another method to identify vortex structures is the Δ criterion (Chong et al. 1990). It uses the complex eigenvalues of velocity gradient tensor to identify local streamline patterns. This includes spiral streamlines or streamlines that form a close loop around a point in the flow in a moving reference frame. For incompressible flow, Δ is defined as

$$\Delta = \left(\frac{1}{2}R\right)^2 + \left(\frac{1}{3}Q\right)^3, \quad (\text{Eqn. 4.5})$$

where $R = -\det(\nabla v)$ and $Q = \frac{1}{2}(\|\Omega\|^2 - \|S\|^2)$. A pair of complex conjugate eigenvalues occur when $\Delta > 0$, which corresponds to a swirling vortex core. The Δ criterion resembles the Q criterion, as shown by the similar extracted structures in Figs. 4.20-4.22d with both methods. From the definition of Δ and Q, however, $\Delta > 0$ is less restrictive than $Q > 0$ and it may have the benefit of keeping the vortex core from broken into small segments.

The different criteria discussed have been widely applied in many DNS studies in turbulence (Hunt et al. 1988, Chong et al. 1990, Jeong et al. 1995, Chakraborty et al. 2005, Kolar 2007) but only recently could experimental measurements provide the necessary results to evaluate these criteria (Elsinga et al. 2010). From the 3D3C velocity data obtained in the present study all the parameters required to apply the different criteria for vortex identification can be obtained. Furthermore, this experimental work can also resolve for the pressure which will be applied as a vortex identification method. To our knowledge, only a few numerical simulations have used the local pressure to characterize the vortex core (Douady et al. 1991, Kalelkar 2006, Wang 2010), and this is the first time it is evaluated experimentally. This is mainly due to the complexity of calculating the pressure experimentally, which involves solving the Navier-Stokes equation after measuring the 3D3C velocity field.

The proposed *pressure criterion* detects the local low pressure region to represent the vortex core structures. Starting from the unforced Navier-Stokes equation,

$$\frac{\partial \bar{u}}{\partial t} + (\bar{u} \cdot \nabla) \bar{u} = -\frac{\nabla p}{\rho} + \nu \nabla^2 \bar{u}, \quad (\text{Eqn. 4.6})$$

applying the continuity equation and taking the divergence, the Poisson equation is obtained (Bradshaw & Koh 1981):

$$\nabla^2 p = \rho \left(\frac{1}{2} \Omega^2 - S^2 \right). \quad (\text{Eqn. 4.7})$$

The right hand side of the equation can be calculated from the experimental 3D3C velocity field. The evaluated right hand side consists of a calculated scalar value at every grid point in the observation volume. The Poisson equation is then solved using a

numerical iteration code in MATLAB to provide the pressure field in the observation volume. A low pressure threshold is used to extract iso-surfaces from the pressure field as shown for an instantaneous snapshot of the flow in Fig. 4.22e. For this simple flow, the shape of the low pressure region is similar to that of enstrophy, Q and Δ . However, the pressure iso-surface has a smoother and better defined boundary. It is speculated that this smoother shapes observed is the result of solving the full Navier-Stokes equation without discarding some of the terms as the other criteria do, which allow precise calculation of the low-pressure regions. Figure 4.22f shows the low-pressure iso-surface and a velocity field in a plane near the center of the volume is also included to show further flow patterns. The velocity field suggests that a rotational vortex (focus) occurs at the low-pressure region and the thresholding iso-surface successfully represents the core of the vortex.

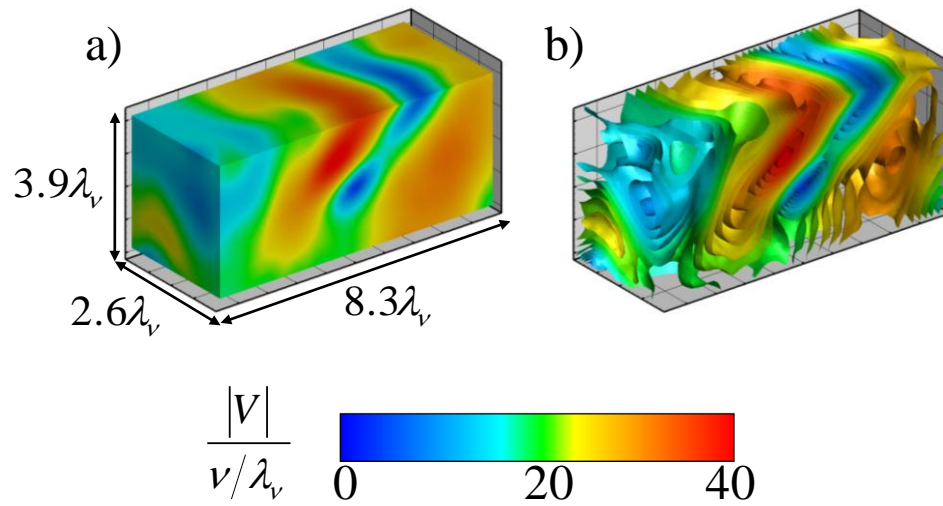


Figure 4.1. Instantaneous 3D velocity profile. a) 3D contour surface plot. b) Group iso-surface plot, which shows the flow structure in more detail.

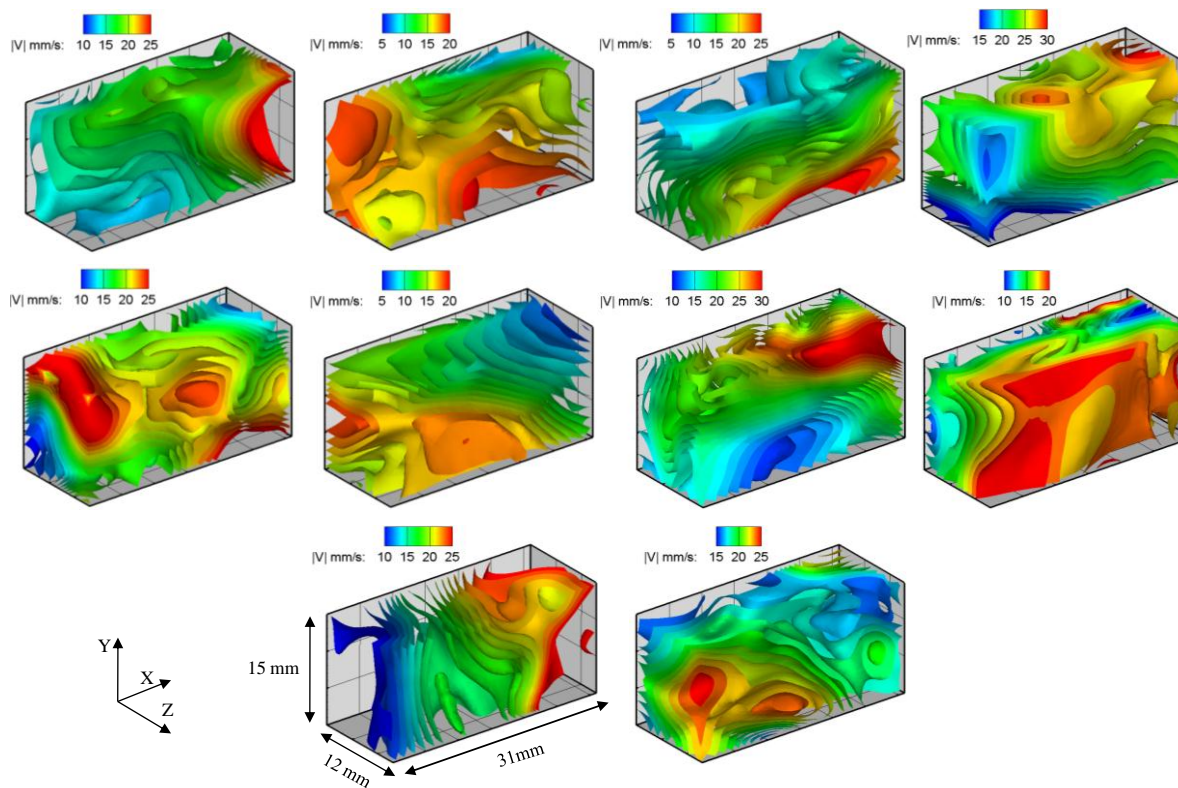


Figure 4.2. Instantaneous velocity profile showing iso-surfaces from 10 independent experiments at $x/D=157$ (side view camera orientation).

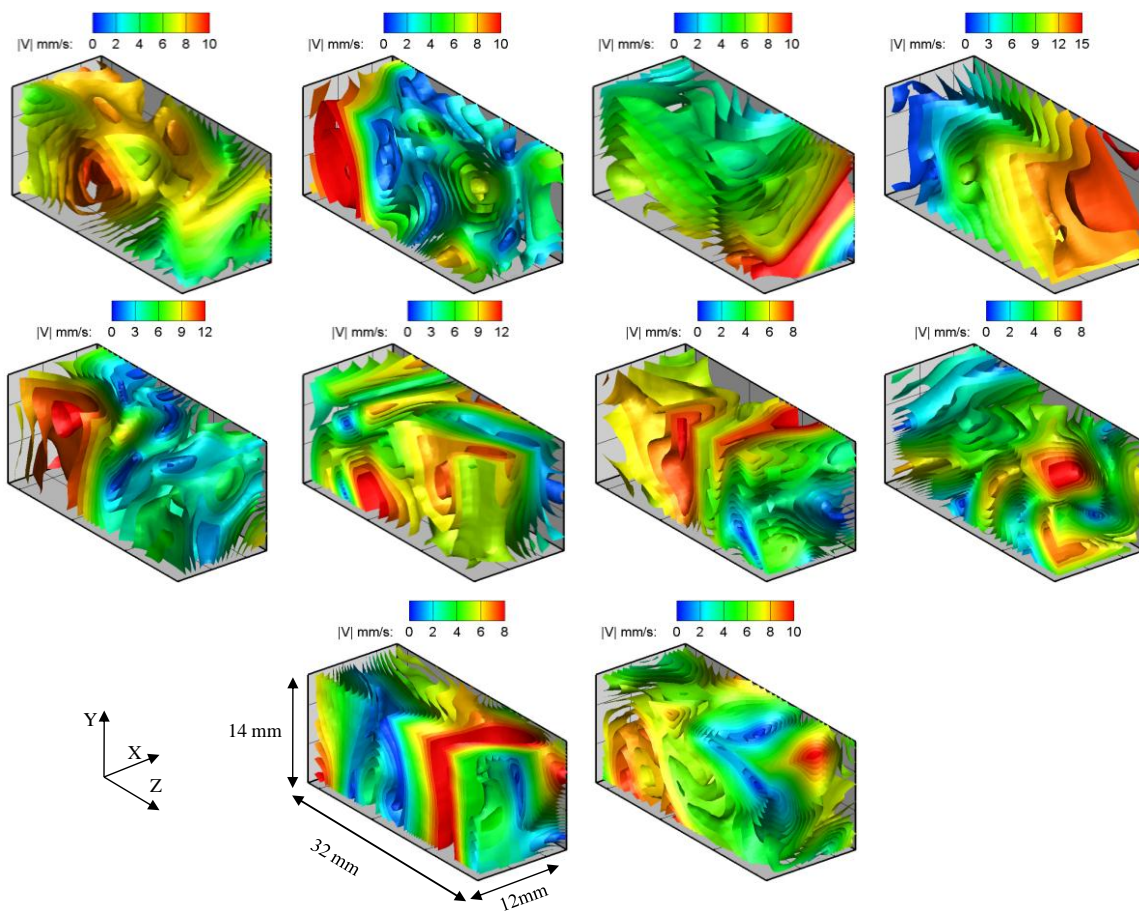


Figure 4.3. Instantaneous velocity profiles from 10 independent experiments at $x/D=157$ cross view camera orientation.

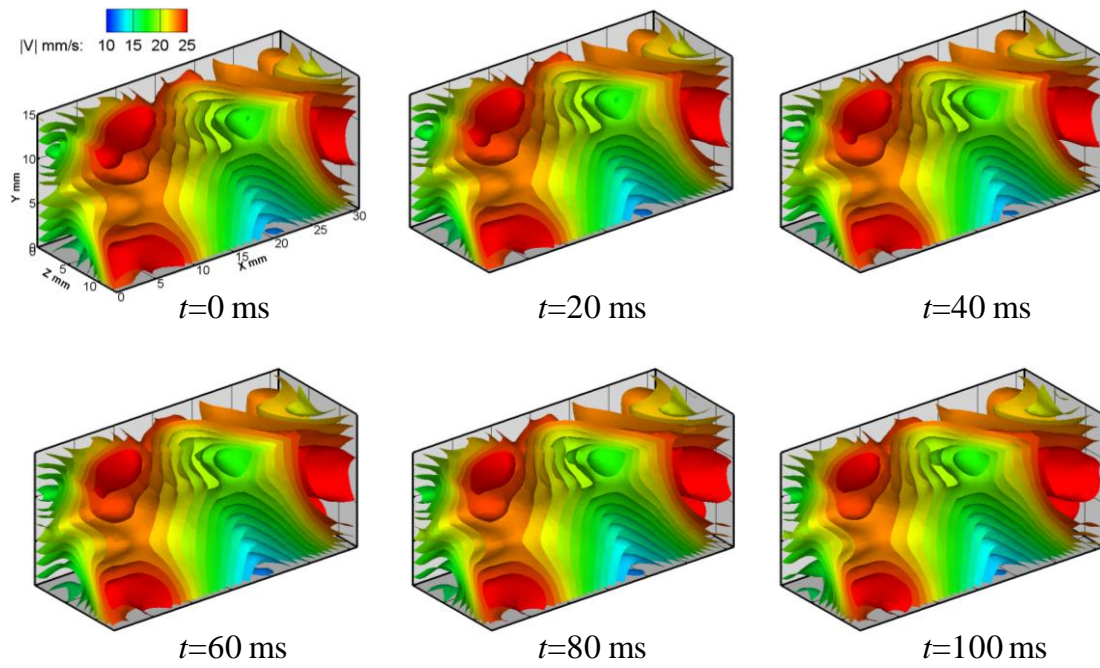


Figure 4.4. Evolution of the velocity structure in time. The structures maintain their shape and propagate downstream along the jet centerline axis

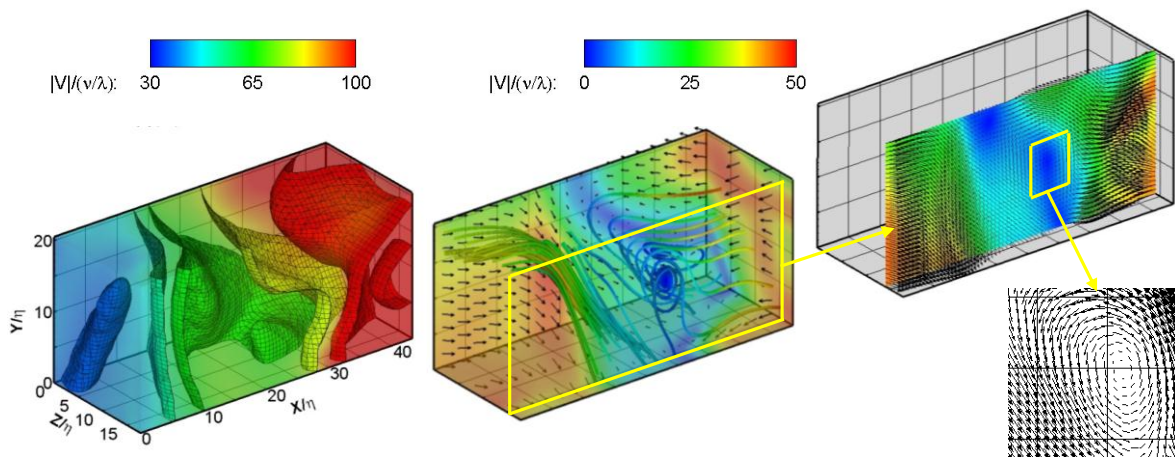


Figure 4.5. a) Typical instantaneous velocity magnitude showing selected iso-surfaces, and b) same volume after performing a Galilean decomposition by subtracting a velocity $0.80 u_c$ to visualize a turbulent eddy shown by streamlines and by c) a 2D vector field in a close up view.

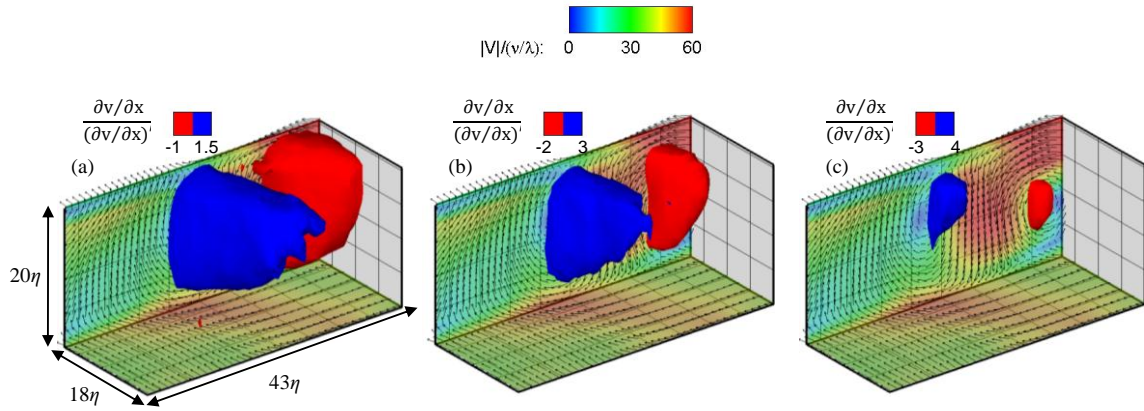


Figure 4.6. Identification of the iso-surfaces for the same velocity gradient component for different thresholding values: a) $a = 1, 1.5$; b) $a = 2, 3$; c) $a = 3, 4$.

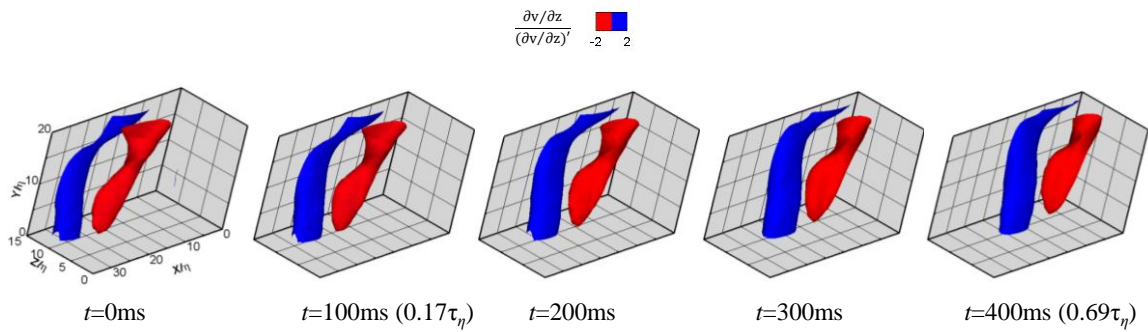


Figure 4.7. Resolved time series showing at selected time steps the iso-surface for one velocity gradient component being convected in the x-direction.

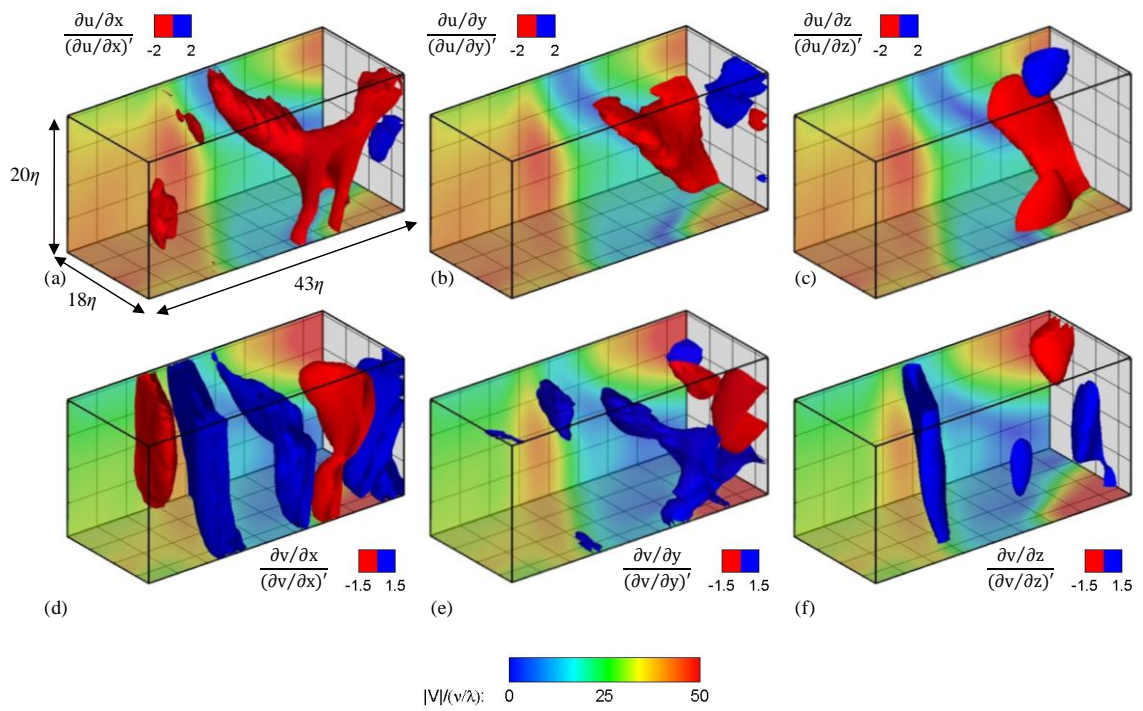


Figure 4.8. Six instantaneous three-dimensional velocity gradients, shown as iso-surfaces for chosen threshold values to extract simple geometrical shapes.

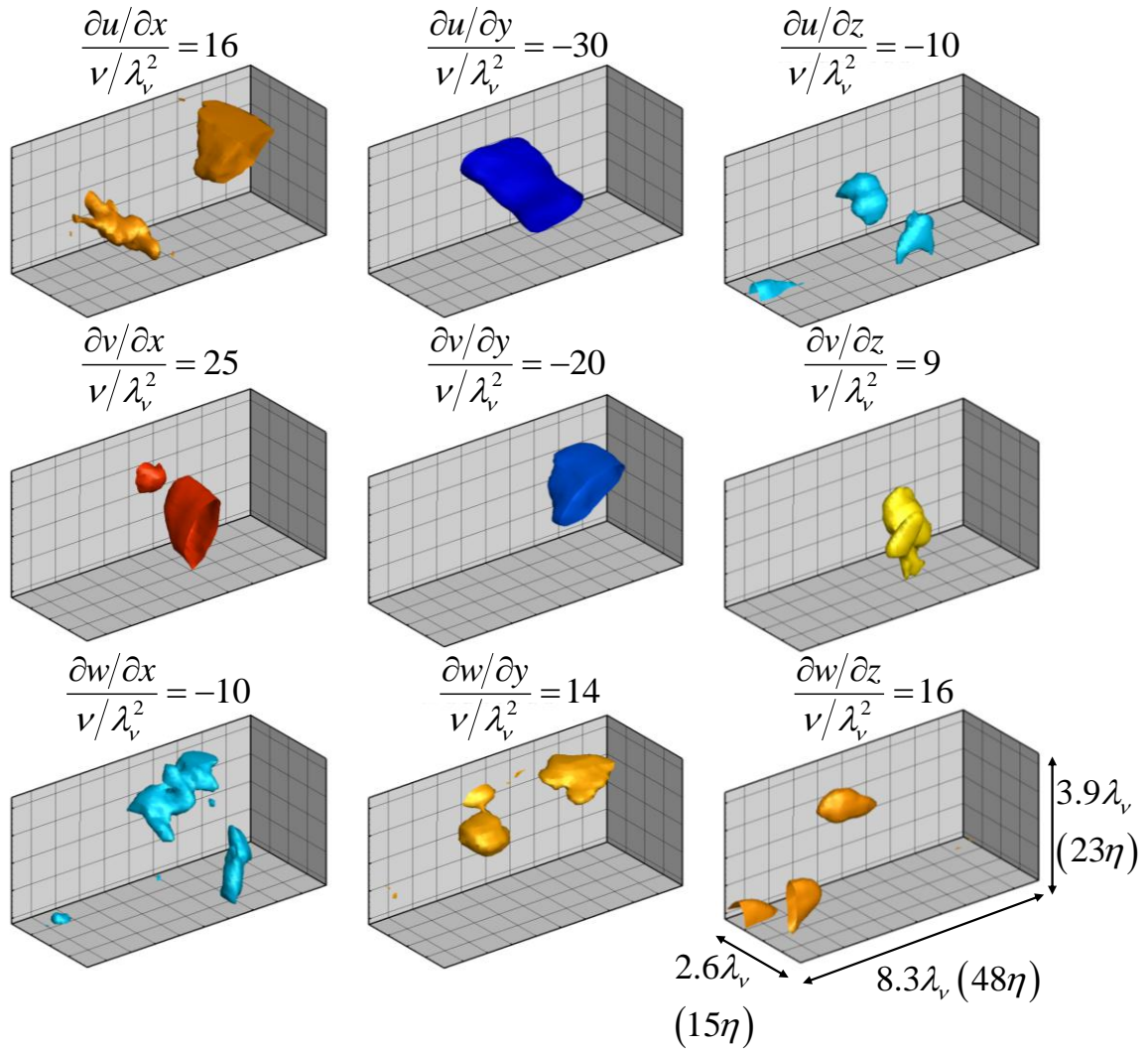


Figure 4.9. Nine instantaneous three-dimensional velocity gradients obtained with 3D3C measurements, shown as iso-surfaces with values normalized by viscous scales.

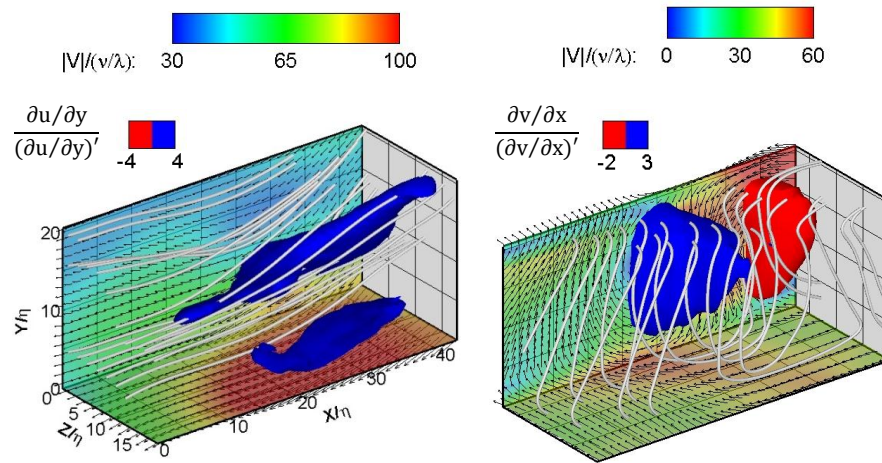


Figure 4.10. Extracted three-dimensional structures of two volumes with velocity gradients that deviated more than 3rms (among 10 3D2C data sets). The streamlines show good correlation between the velocity and velocity gradients.

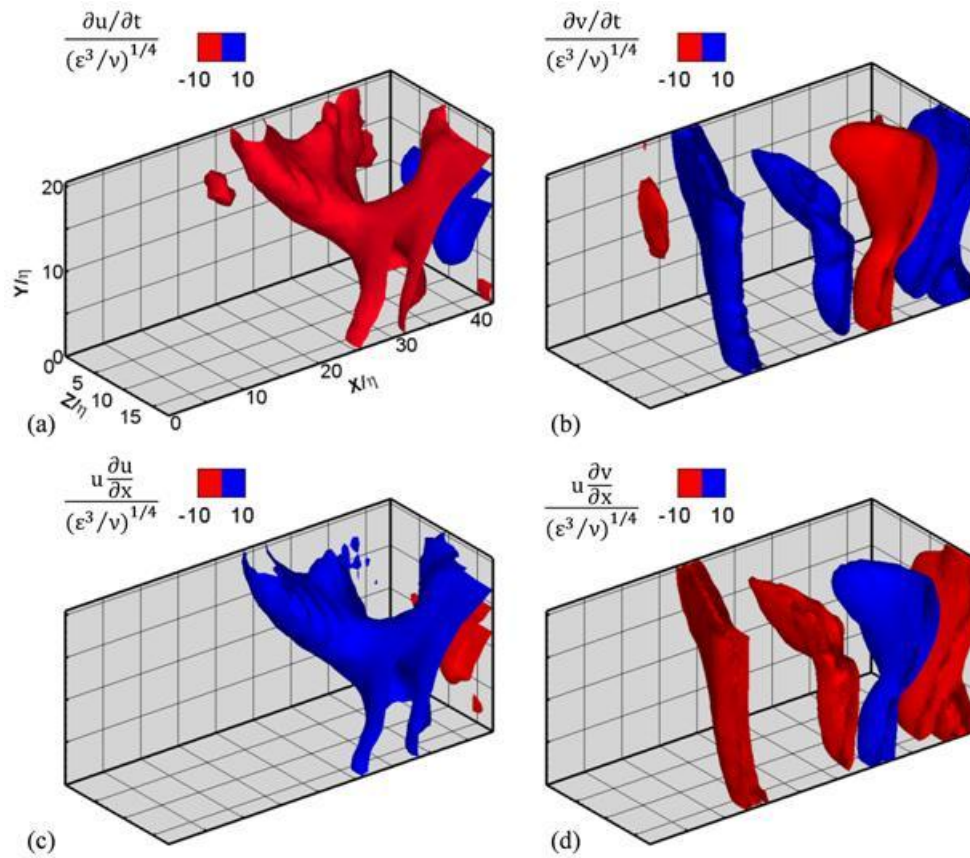


Figure 4.11. Extracted three-dimensional local acceleration structures for a) $\partial u / \partial t$ and b) $\partial v / \partial t$ c) $u \partial u / \partial x$ and d) $v \partial v / \partial x$ normalized by local viscous scales. The local accelerations appear to be anti-aligned with the convection acceleration terms.

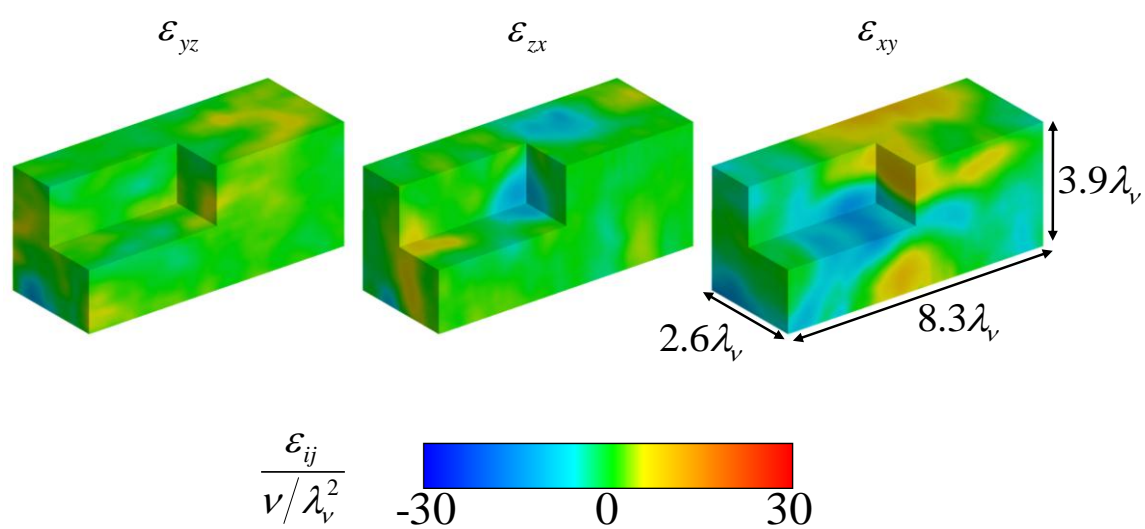


Figure 4.12. Contour plots on surfaces in a volume of the three shear (off-diagonal) rate of strain components.

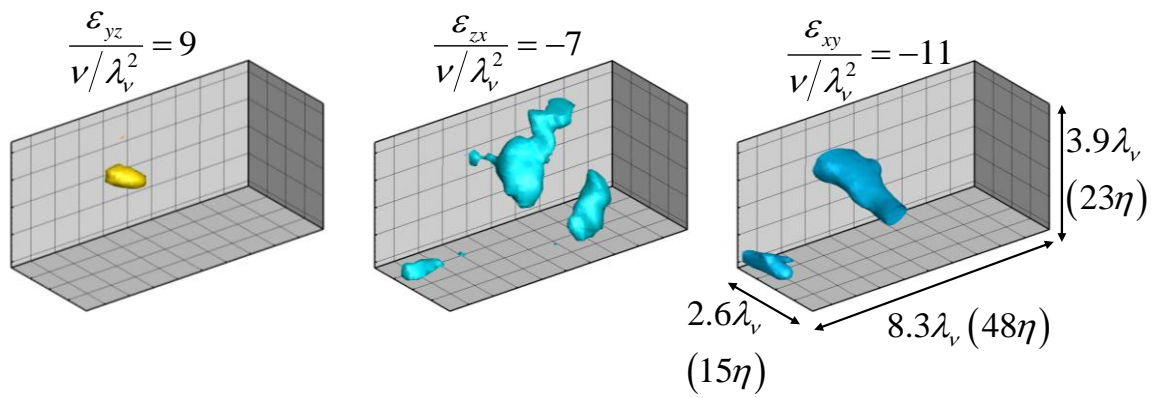


Figure 4.13. Extracted iso-surfaces of the same volume as in Fig. 4.11, showing the three shear (off-diagonal) rate of strain components.

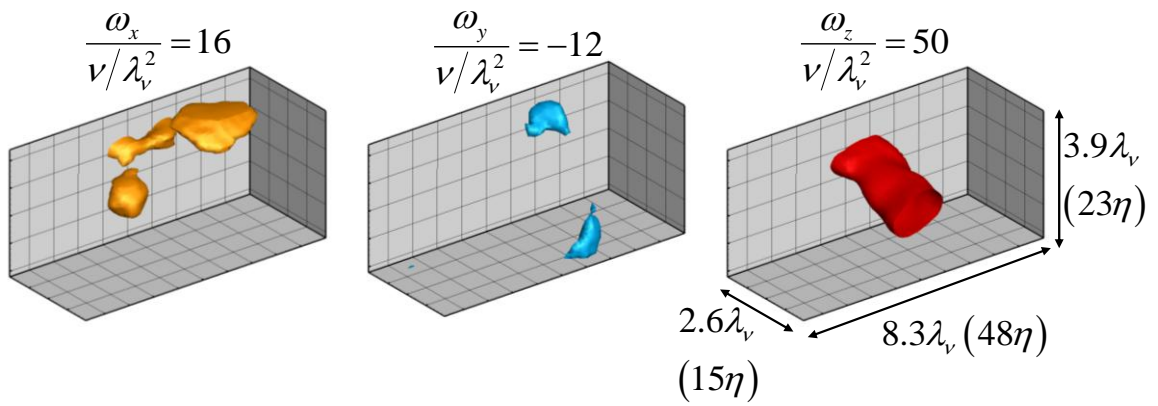


Figure 4.14. Extracted iso-surfaces of the same volume as in Fig. 4.12, showing the three vorticity components.

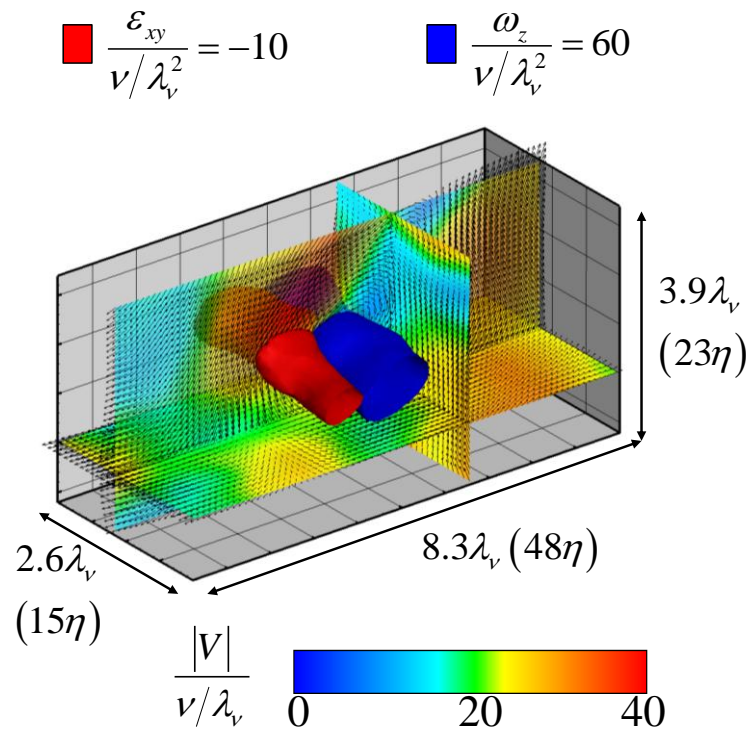


Figure 4.15. Combination of strong vorticity and strain rate component structures. The slices show contour of subtracted velocity magnitude and the vectors show the three-component velocity field. The combination of vorticity and strain rate appears at a focus type of vortex.

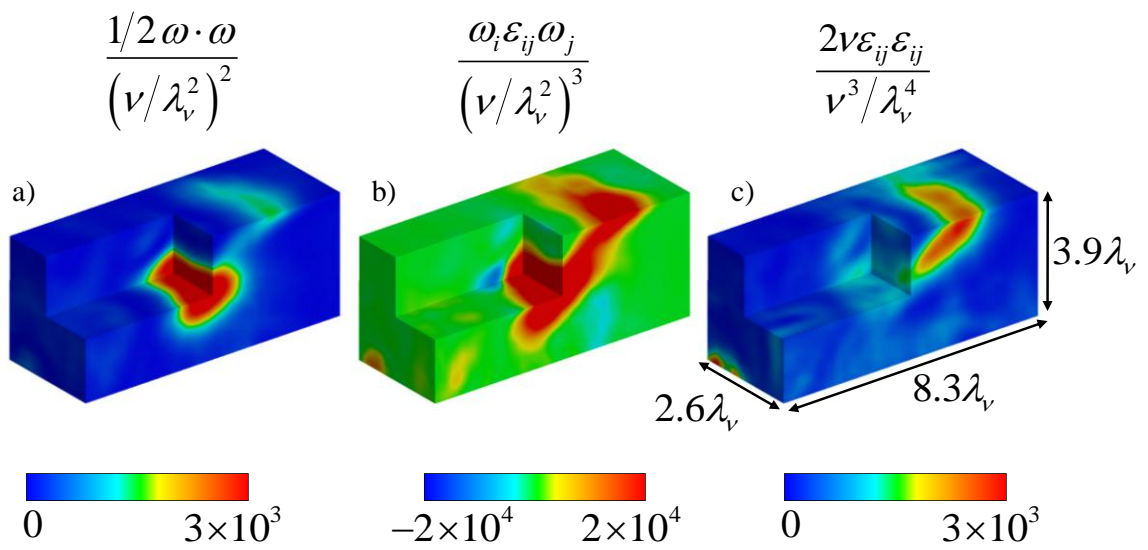


Figure 4.16. Contour plots of enstrophy, enstrophy production rate and energy dissipation rate.

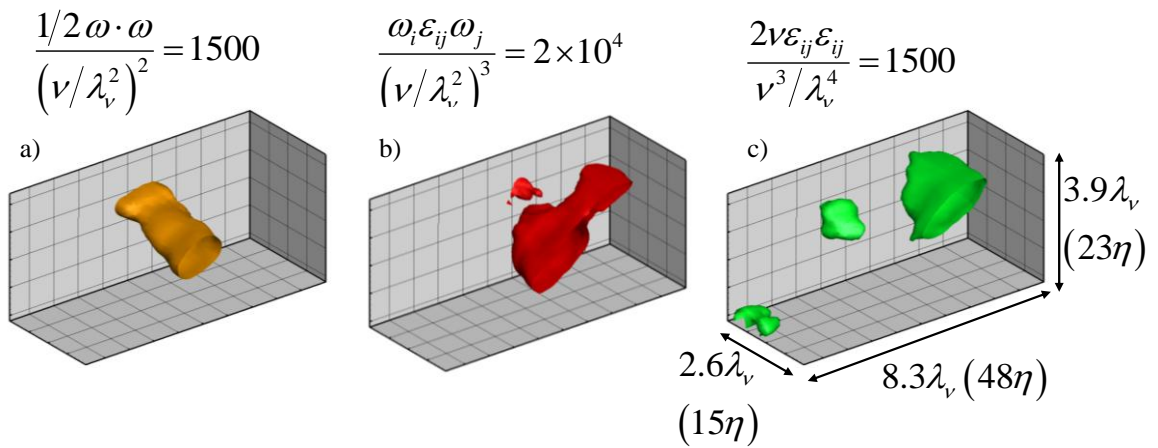


Figure 4.17. Extracted iso-surfaces of the same volume as in Fig. 4.15, showing enstrophy, enstrophy production rate and energy dissipation rate.

Methods	Description	Criteria for vortex core
Enstrophy	$E = \ \Omega\ ^2$	$E \neq 0$
Q criterion	$Q = \frac{1}{2}(\ \Omega\ ^2 - \ S\ ^2)$	$Q > 0$
λ_2 criterion	λ_2 is the intermediate eigenvalue ($\lambda_1 \geq \lambda_2 \geq \lambda_3$) of tensor $\Omega^2 + S^2$.	$\lambda_2 < 0$
Δ criterion	$\Delta = \left(\frac{1}{2}R\right)^2 + \left(\frac{1}{3}Q\right)^3,$ <p>where $R = -\det(\nabla u)$ and $Q = \frac{1}{2}(\ \Omega\ ^2 - \ S\ ^2)$</p>	$\Delta > 0$
Pressure	Local pressure solved with Poisson equation $\nabla^2 P = \rho \left(\frac{1}{2} \Omega^2 - S^2 \right)$	$P \approx 0$

Table 4.1. Description of various vortex identification methods.

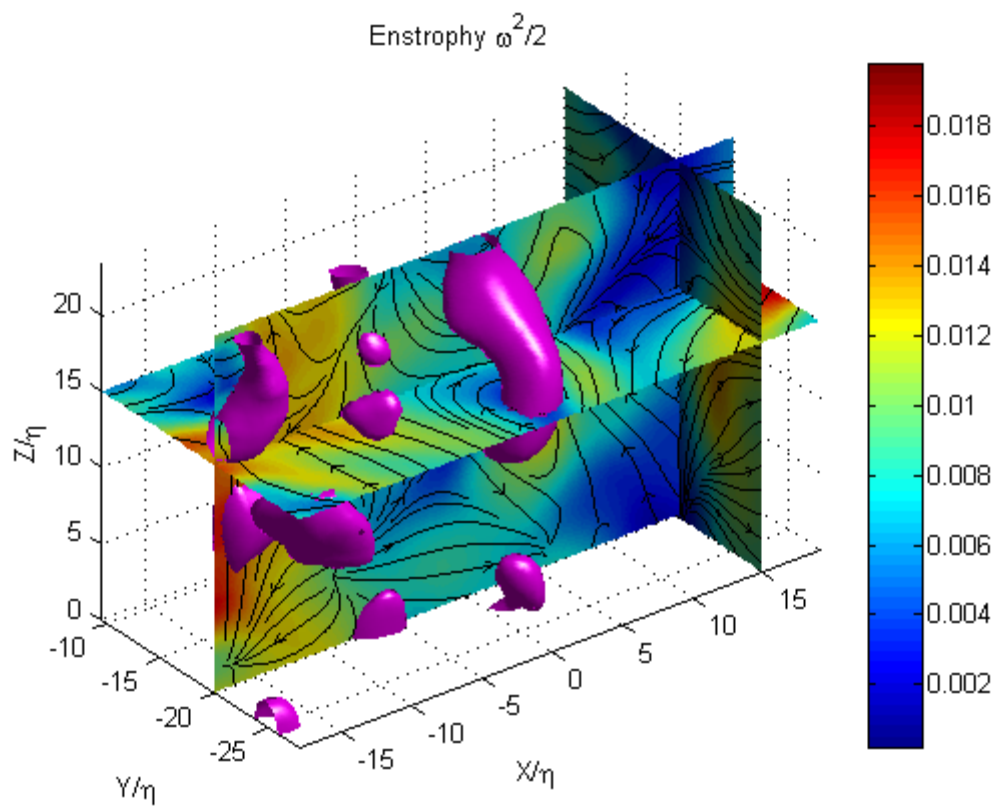


Figure 4.18. Iso-surfaces of enstrophy accompanied with velocity slices showing velocity magnitude (contour) and streamlines. Enstrophy structures occur at both focus and saddle type of flow pattern.

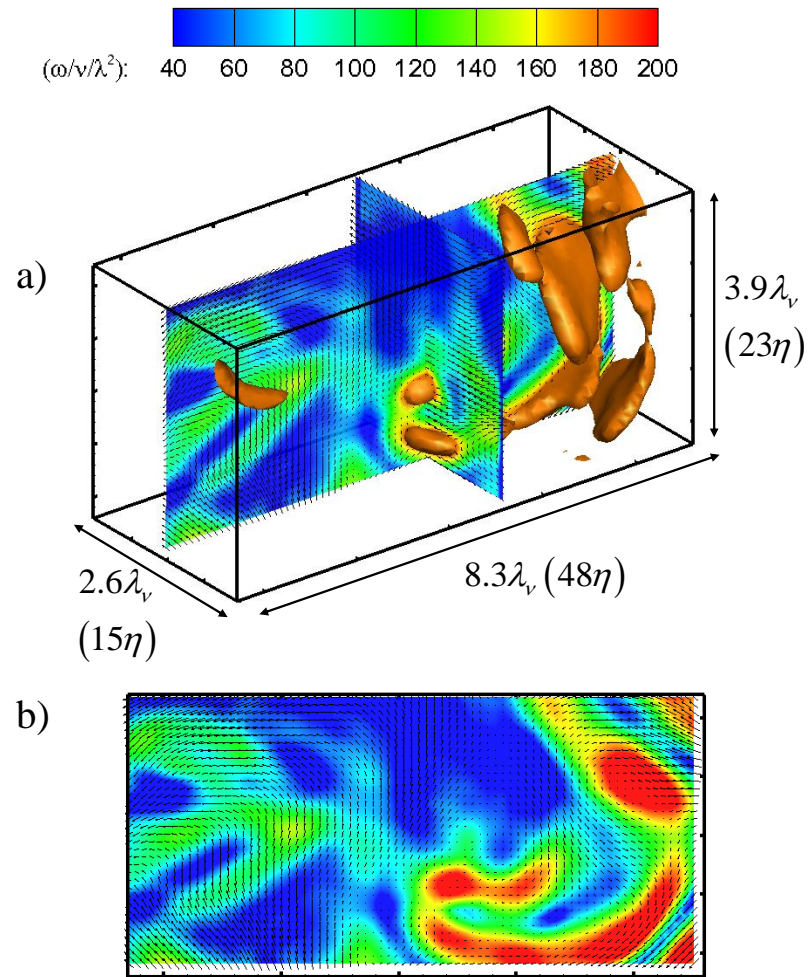


Figure 4.19. Enstrophy and velocity field. a) 3D view with enstrophy iso-surfaces and velocity slices; b) 2D view of enstrophy contour. Enstrophy represents both vortex tubes and sheet-like structure created by shear.

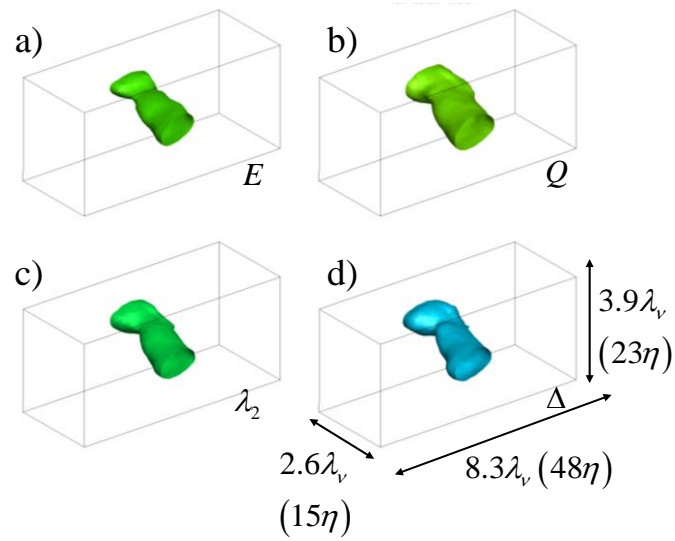


Figure 4.20. A sample observation volume showing iso-surfaces represented by different vortex identification parameters. a) Enstrophy b) Q Criterion c) λ_2 criterion d) Δ criterion.

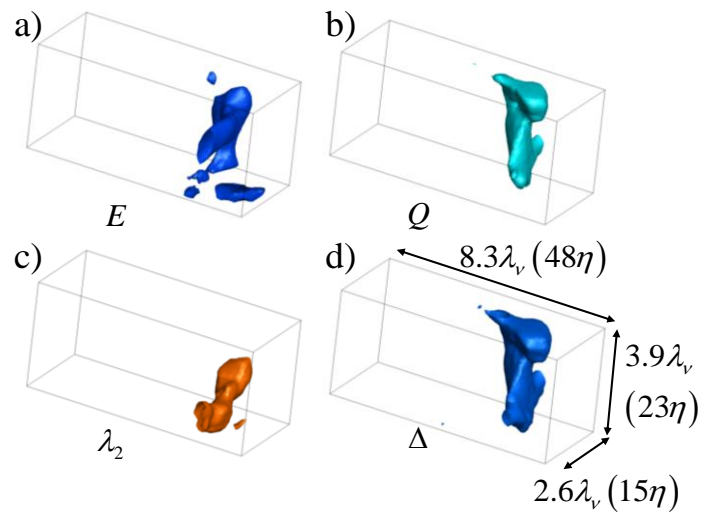


Figure 4.21. A sample observation volume showing iso-surfaces represented by different vortex identification parameters. a) Enstrophy b) Q Criterion c) λ_2 criterion d) Δ criterion.

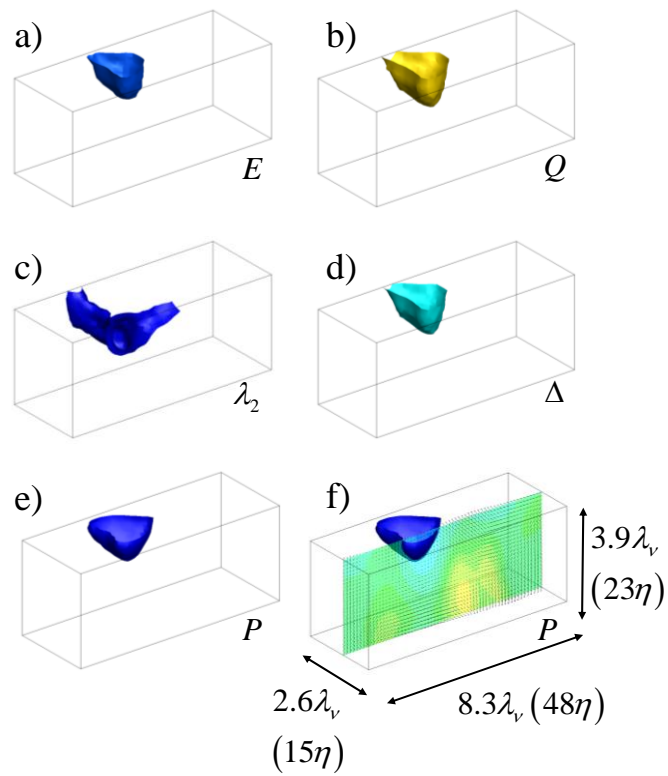


Figure 4.22. A sample observation volume showing iso-surfaces represented by different vortex identification parameters. a) Enstrophy b) Q Criterion c) λ_2 criterion d) Δ criterion e) Pressure f) pressure with a slice of velocity field showing location of the vortex.

Chapter 5

Statistical Analysis of Turbulence

Due to its extreme complexity, turbulence is often quantitatively characterized through statistical analysis. Many previous studies in turbulent flow have performed different types of averaging, probability density, and spectra analyses on velocity gradients and energy dissipation. Most of these studies were done in DNS simulations (Biferale et al. 1991, Gotoh et al. 2002, Wilczek et al. 2010) and only two experimental studies (Mullin & Dahm 2006, Ganapathisubramani et al. 2008) were also able to obtain the full velocity gradient components with sufficient samples for statistical analysis. The present work includes results from 4 different flow and measurement conditions, each obtained from 10 independent sets with 10 instantaneous reconstructed volumetric velocity fields each. The analysis includes the statistics of velocity gradients, velocity gradient ratios, principle strain rates, vorticity, enstrophy, enstrophy production rate, energy dissipation rate, energy spectrum and dissipation spectrum. The results were compared among the four cases and validated with published work where possible. A detailed error analysis is presented considering the continuity relation, isotropy assumption and repeatability.

5.1 Measurement configurations

The present study considers four different flow configurations in a free shear turbulent jet. A description of the four cases is listed in Table 3.2. Case 1 and 2 are taken at the same downstream centerline location $x/D=150$ at jet exit Reynolds numbers $Re_D=1400$ and $Re_D=2800$ respectively (Fig. 5.1a). Case 3 is taken at a downstream location $x/D=80$ off-axis from the centerline at $Re_D=1400$ (Fig. 5.1b). Case 4 considers the same flow condition as Case 1 ($x/D=150$, $Re_D=1400$, centerline), but with the two cameras in a cross-view orientation (Fig. 5.1c). Case 4 should yield similar statistical results as Case 1 since they observe the same volume and the TR-SSPIV system provides the 3D3C velocity in that volume regardless of the camera orientation.

5.2 Velocity gradients and isotropy

Velocity gradients are responsible for the rotation and deformation of fluid material in turbulence. Material propagation, mixing, vortex stretching, dissipation, and many other dynamic phenomena are closely related to the presence of velocity gradients. Especially in fine-scale turbulence, the statistics of the velocity gradients are often studied to characterize the universality of the flow. Probability density function (PDF) of the velocity gradients have been widely investigated in both DNS and experimental studies (Biferale et al. 1991, Mullin & Dahm 2006, Ganapathisubramani et al. 2008, Yoshimatsu et al. 2009, Ishihara et al. 2009). The present study calculates the PDF of nine velocity gradients for three flow conditions (Case 1-3 in §5.1) and compare it with available published results.

The nine components of velocity gradients are calculated using a central-difference scheme in the volumetric velocity fields. The PDFs calculated at the boundaries of the observation volume are discarded considering that the higher accuracy central difference scheme could not be applied at these boundaries. Each volumetric velocity field contains 20 planes. Each plane contains 76×38 grid points with the three components of the velocity known at each point. The analysis is performed in 10 individual sets with 10 instantaneous reconstructed volumetric velocity fields each. Figures 5.2-5.4 illustrate the PDFs of velocity gradients for Case 1-3. The results are shown in semi-logarithmic axes, with the velocity gradient components non-dimensionalized by the viscous scale (v/λ_v^2) to allow for comparison between different flow conditions. The PDF shapes are similar between different flow conditions and between the different velocity components as well. The shape of the PDFs deviates significantly from Gaussian profiles which has been previously reported in both numerical and experimental studies (Chen et al. 1989, Sreenivasan & Antonia 1997, and Ganapathisubramani et al. 2008). This is due to the intermittency of turbulence, the presence of occasional high velocity gradient values causing the separation at the tails.

Some revealing features of the velocity gradient PDFs will be discussed next. First, the tail of the pdfs for the three on-diagonal velocity gradient components ($\partial u_i / \partial x_j, i = j$) in Figs. 5.2a-5.4a, have steeper gradient than the tails of the pdfs for the off-diagonal components ($\partial u_i / \partial x_j, i \neq j$) in Figs. 5.2-5.4b. This is consistent with other experimental results for free shear turbulence (Mullin & Dahm 2006 and Ganapathisurbarmani et al.

2008) where the data satisfied the local homogeneous isotropy relation $\overline{(\partial u_i / \partial x_j)_{i \neq j}^2} = 2 \overline{(\partial u_i / \partial x_j)_{i=j}^2}$. This is further verified in Table 5.1 for the present data where the ratios of the root mean square statistics are compared to local isotropy and with Mullin & Dahm 2006 and Ganapathisubramani et al. 2007. Mullin & Dahm 2006 also concluded that they had a reasonable agreement when comparing their calculated ratios to local isotropy conditions as shown in Table 5.4. On the other hand, Ganapathisubramani et al. 2007 indicated that their measurements do not satisfy local isotropy conditions, especially along the mean flow direction as indicated by their ratios of 1.455 and 1.629 shown in Table 5.4 which depart from the isotropy value of 2. Instead, Ganapathisubramani et al. 2007; George & Hussein 1991 observed that their far field data in a turbulent jet conformed to axisymmetric isotropy conditions and not to homogeneous isotropy.

A second revealing feature observed corresponds to the behavior of left and right tails of the velocity gradient PDFs. The right tails appear steeper and less separated than the left ones, especially in Case 1 (Fig. 5.2) and Case 3 (Fig. 5.4), where the Reynolds numbers are smaller compared to Case 2 (Fig. 5.3). Considering that all the PDFs appear to have a straight line profile when plotted on semi-logarithmic axes, the slopes can be computed as exponentials decay using

$$\alpha = - \frac{d \log P(\partial u_i / \partial x_j)}{d |\partial u_i / \partial x_j|}, \quad (\text{Eqn 5.1})$$

where α is the scaling factor (slope of the straight-line) and $P(\partial u_i / \partial x_j)$ is the PDF of any velocity gradient. A least-square fit was used to compute the scaling factor α and the

results are listed in Table 5.1-5.3 for the three cases studied. The scaling factors can vary significantly between the left and right tails of the same velocity gradient component with up to 34% difference. These results indicate a slight departure from local homogenous isotropy. This phenomenon was also observed in DNS simulations (Gotoh et al. 2002) and experimental studies (Mullin & Dahm 2006, Ganapathisubramani et al. 2008).

The third observation is the slight variations in the velocity gradient PDFs between the three cases. These variations are observed when the Reynolds number was varied. For instance, from Case 1 to Case 2 the Reynolds number was doubled. As a result, when comparing the PDFs between these two cases in Fig. 5.2 and 5.3, Case 1 shows less separation between different velocity gradient components in both on- and off-diagonal directions. This can be explained by reports suggesting that homogeneous isotropy requires sufficient large Reynolds number, and Case 1 ($Re_\lambda = 44$) is considered at the low end of turbulent shear flow. Variations between the PDFs are also observed when measurements were taken along the jet centerline or off-axis. For instance, Case 1 and 2 were both taken at the centerline of the jet, while Case 3 was taken in the shear layer region near the jet's edge. Clearly, Case 3 departs from isotropy in the shear layer as shown in Fig. 5.4b, but not the other two cases along the centerline. This was also discussed in detail by Mullin & Dahm 2006.

To further investigate the isotropy of free shear turbulent flows, the ratios of the RMS velocity gradients are calculated. When possible, the measurements are compared to the results by Ganapathisubramani et al. 2007 in Table 5.5 which observed local

axisymmetry for these flows. The requirements for axisymmetric isotropy (Ganapathisubramani et al. 2007, George & Hussein 1991) are only a subset of the requirements needed for homogeneous local isotropy. The present data shows a reasonable agreement with axisymmetric isotropy with a largest error of 9%, compared to the largest of 7% by Mullin & Dahm 2006 and 14% by Ganapathisubramani et al. 2007. The departure from local isotropy is possibly related to the fact that the RMS are averaged in a 3D volume for the current case and Ganapathisubramani et al. 2007, whereas in a 2D plane by Mullin & Dahm 2006.

Higher order derivatives of the velocity gradients can be calculated and compared with previously published work. Table 5.6 shows the skewness (third-order moments) and kurtosis (fourth-order moments) of velocity gradients. They compared favorably to the measurements by Mullin & Dahm 2006 at $Re_\lambda = 45$, and to Gulitski et al. 2007 at $Re_\lambda = 1600$. Meanwhile, the calculated skewness and kurtosis for the velocity gradient ($\partial u / \partial x$) from Table 5.6 match the results in Fig. 1 from Sreenivasan & Antonia 1997 at $Re_\lambda = 38$.

5.3 Principal strain rates

Strain rate describes the basic flow structures in terms of stretching and compression and affects the dynamics of the flow. Three principal strain rates (α, β, γ) are often used to characterize the strain rate tensor. Principal strain rates are defined as the three eigenvalues of the strain rate tensor ($\alpha \geq \beta \geq \gamma$), where α is the compressive principal

strain, β is the intermediate principal strain, and γ is the extensive principal strain. A PDF analysis of the three principal strain rates is presented in Fig. 5.5. In Fig. 5.5a (Case 1, $Re_\delta = 3200$ centerline), the compressive and extensive strain rates are nearly symmetric from each other around the 0 value, which correspond to the near symmetric shape of the intermediate strain rate. The profiles of the principal strain rate PDFs are in agreement with recent published work (Nomura & Post 1998 and Dahm & Mullin 2006). The PDFs showed improved symmetry compared to those by Ganapathisubramani et al. 2008, perhaps due to the improved resolution of the present measurements.

For incompressible flow, the continuity equation requires the three principal strain rates to satisfy $\alpha + \beta + \gamma = 0$. The calculated RMS for $\alpha + \beta + \gamma$ in the present study is 0.2 which is comparable to Ganapathisubramani et al. 2007. The small departure from zero is created by the uncertainty and error in the velocity and velocity gradients measurements with a more detailed error analysis presented in §5.7. There are also some differences between the three flow conditions studied. For instance, Fig. 5.5c (Case 3, $Re_\delta = 3200$ off-centerline) shows the results for the same turbulent jet as in Fig. 5.5a (Case 1, $Re_\delta = 3200$ centerline), but at a different radial location. The value of the principal strain rates appears to vary significantly, with the off-axis case being nearly two times that of the centerline case. This indicates that higher strains occur at the interface between the jet and the quiescent fluid. Mullin & Dahm 2006 reported similar findings.

Intermediate principal strain β can be either positive or negative depending on the values of α and γ . Previous studies show that the sign of β affects the structures of the

flow, where $\beta > 0$ characterizes tube-like structures and $\beta < 0$ represents higher strain rate with sheet-like structures (Betchov 1956, Diamessis & Nomura 2000). To study the intermediate principal strain, it is normalized using $\beta^* = \sqrt{6}\beta / \sqrt{\alpha^2 + \beta^2 + \gamma^2}$. Figure 5.6 shows the profile of the PDF of the normalized intermediate strain rate β^* . In all three cases, the profiles appear to be near symmetric with a slight preference towards $\beta^* > 0$. This is consistent with the statement that the ensemble average of intermediate strain rate is larger than zero in homogeneous turbulence (Diamessis & Nomura 2000). The profile of intermediate strain reveals some error in the velocity measurements, since there are values of β^* that exceeds ± 1 , which are physically impossible. Nevertheless, Lund & Rogers 1994 and Ganapathisubramani et al. 2007 also noted that the tails of PDF of β^* extends to ± 1.5 due to uncertainty in experimental measurements.

To study the relationship between the normalized intermediate strain rate β^* and the magnitude of strain rate tensor $e = \sqrt{\alpha^2 + \beta^2 + \gamma^2}$, their joint PDF is calculated and shown in Fig. 5.7. While β^* is nearly symmetric, the peak of the joint PDF shows a slight tendency toward higher intermediate strain rate. This is another indication that the high strain rate yields sheet-like structures, as previously reported by DNS study (Ashurst et al. 1987) and experimental measurements (Ganapathisubramani et al. 2008). Also, the highest probability of strain rate magnitude varies between the three cases. Case 2 has the highest strain rate magnitude among all and is about 2.8 times that of Case 1. The relation of the strain rate and outer Reynolds number can be expressed using $e \propto \nu / \lambda_v^2 \propto \text{Re}_\delta^{3/2}$, and since the outer Reynolds number of Case 2 is 2 times of that of Case 1, the ratio in strain

rate magnitude (2.8) matches the above relation. This further suggests that using viscous scale normalization (ν/λ_v^2) helps characterizing the flow independent of Reynolds number for the range of Re_λ discussed.

The three eigenvectors \hat{e}_i of the strain rate tensor that correspond to the three principal strain rates are also evaluated for isotropy. A spherical coordinate frame is used to characterize the alignment of eigenvectors. The PDFs of the two spherical angles θ and φ are:

$$P(\theta) = \frac{1}{2\pi}, \quad (\text{Eqn 5.2})$$

$$P(\varphi) = \frac{1}{2} \sin \varphi, \quad (\text{Eqn 5.3})$$

when the flow is isotropic. The PDFs of the two spherical angles for the three principal eigenvectors are shown in Fig. 5.8-5.10. The theoretical PDFs for isotropy are shown with solid lines for comparison with the experimental results. The PDFs of the spherical angles for the three eigenvectors have some preferred alignment direction: $\varphi = \pi/2$ and $\theta = 0$. This indicates that the departure from isotropy is due to the mean shear from the bulk flow movement. Case 1 (Fig. 5.8) and 2 (Fig. 5.9) have better resemblance compared to Case 3 (Fig. 5.10), where stronger alignment with $\theta = 0$ is observed, indicating more intense shear at the boundary of the jet. Comparable results were previously reported by Mullin & Dahm 2006 and the similar fashion of departure from isotropy in the three cases suggests the consistency of the current measurements.

5.4 Enstrophy and enstrophy production rate

The study of higher order velocity gradient parameters can provide additional information about the isotropy of the flow. This includes the enstrophy, $\frac{1}{2}\omega \cdot \omega$, a second order velocity gradient parameter, which will be evaluated to check for isotropy and investigate its relation with the dissipation at the fine scales in turbulence. Figure 5.11a (Case 1) presents the PDF of the enstrophy normalized by the viscous length scale. The PDF shows a peak at about 40 with occurrences of some large values up to 1000. This is due to the intermittency of turbulence at fine scales where local intense fluctuations exist. Taking the logarithm of enstrophy, the PDF can be fitted with a log-normal distribution as shown in Fig. 5.11b. The PDF peaks at 2.5 and similar peak values were obtained by Mullin & Dahm 2006 although under different flow condition. Figure 5.12 shows the PDF of enstrophy for Case 2. A closer resemblance to lognormal is observed with this flow with higher Reynolds number ($Re_\delta = 6400$), indicating that the departure in Case 1 is due to its lower Reynolds number which is at the low end of isotropic turbulence.

Enstrophy production rate, $\omega \cdot S \cdot \omega$, is a third order velocity gradient parameter that describes the local stretching of vortices by strain rate tensor. Figures 5.14a-16a show the PDF of enstrophy production rate normalized by the appropriate viscous scale, $(\nu/\lambda_v^2)^3$. The PDF shows a sharp spike at 0 which is expected from high velocity gradient parameters and it then quickly drops to less than $\pm 1 \times 10^5$. A Semi-logarithm scale is used in Figs. 5.14b-16b to better observe the tails of the PDF of enstrophy production rate. The profile is nearly symmetric and the rarely occurring high values are bonded between

$\pm 2.5 \times 10^4$. It is also observed that Case 3 (Fig. 5.16) shows the lowest enstrophy production rate. This indicates that the enstrophy production rate is lower at the shear layer of the jet.

5.5 Energy dissipation rate

The kinetic energy dissipation rate, $\varepsilon = 2\nu S_{ij}S_{ij}$, represents the intensity of the local strain and is an important parameter in turbulence since its average value is used to define the Kolmogorov scale parameters. Therefore it has been widely studied in numerical simulations. Also, this is part of the $k-\varepsilon$ model which is often used to solve the Navier-Stokes equation especially in free shear turbulence. The calculation of the mean energy dissipation rate is related to axisymmetric and homogenous isotropy and will be discussed in detail in §5.7. First, the probability distribution of the energy dissipation rate will be analyzed. Figure 5.17a illustrates the PDF of energy dissipation rate normalized by ν^3/λ_v^4 . The tail of the high energy dissipation rate is not as pronounced as that for the high enstrophy in Fig. 5.11a. This behavior is consistent with the observation by Donzis et al. 2008 through DNS methods. Enstrophy appears to be more intermittent and have more scattered intense values compared to energy dissipation rate.

The logarithm of the energy dissipation rate PDF is shown in Fig. 5.17b. It has a high resemblance to the PDF of the enstrophy (Fig. 5.11b), and it has a better lognormal distribution fit. These PDFs and their statistical similarity between energy dissipation rate and enstrophy are consistent with DNS results from Zeff et al. 2003 and Donzis et al. 2008 and experimental measurement by Mullin & Dahm 2006. They indicate the

universality of the energy dissipation field in fine-scale turbulent flow. Figures 5.18-5.19 show the PDFs of energy dissipation rate for Case 2 and 3. Their shapes and range of values are both same to those of Case 1. This is due to the fact that the energy dissipation rate is normalized with viscous scales ν^3/λ_v^4 , which is on the same order of ε .

5.6 Energy and dissipation spectrum

The energy spectrum $E(\kappa)$ is of great interest since it characterizes how the turbulent kinetic energy is distributed among eddies of different sizes. The wavenumber κ , is defined as $\kappa \equiv 2\pi/l$, where l is the characteristic length of eddies. The energy spectrum of the u velocity along the streamwise direction is calculated from the instantaneous volumetric velocity fields and normalized by Kolmogorov scales. The energy spectrum is plotted in Fig. 5.20a with the experimental data shown by circles. For comparison, a theoretical model of the energy spectrum for homogeneous isotropic turbulence (Pope 2000) is also shown by the solid line. Although the inertial range is mostly missing for such a low Reynolds number studied, the experimental data approach this inertial range with the $-5/3$ slope. The high spatial resolution of the PIV measurements allowed the experimental data to collapse with the theory, even at high wave number κ .

The actual spatial resolution and the filtering behavior that can be obtained with PIV measurements have been considered in great detail by Hart 2000 and Foucaut et al. 2004. From these studies it can be shown that for the present measurements the smallest eddies (with a near Kolmogorov length size) would be slightly under-resolved. This can be

estimated from an expression in Hart 2000, where an assumed sinusoidal velocity is used to compare the gain G_{FFT} of the computed velocity with the true velocity using FFT spectral correlation. The expression for the gain is given by $|G_{FFT}| = |V_{cal}/V_{true}| = |2\sin(\kappa L/2)/\kappa L|$, where L is the size of the interrogation window. For the present work the maximum wavenumber calculated, as shown in Fig. 5.20a, is $\kappa_{max} = 1.5/\eta$ which corresponds to $l = 4.2\eta$ and a gain of $|G_{FFT}| = 0.87$. This corresponds to the lowest gain for the highest wavenumber shown in Fig. 5.20a, and therefore even smaller deviation from the true velocities are obtained for $\kappa\eta < 1.5$. In addition, the minimum wavenumber is calculated by $\kappa_0 = 2\pi/L_{max}$ (Pope 2000), where L_{max} is the length of the field of view 48.8η which corresponds to $\kappa_0\eta = 0.129$.

The dissipation spectrum $D(\kappa)$ is the spectrum of the kinetic energy dissipation rate ε and is related to the way energy is dissipated between different size eddies. The dissipation spectrum of the streamwise velocity can be easily derived from the energy spectrum using $D_{11}(\kappa) = \kappa^2 E_{11}(\kappa)$. Figure 5.20b shows the normalized dissipation spectrum on semi-logarithm axes, where solid line represents model spectrum by Pope 2000. A peak value occurs at around $\kappa\eta \approx 0.1$, which is consistent with other work (Antonia et al. 1982 and Mi & Nathan 2003). This indicates that most of the dissipation occurs at eddies that are larger than the Kolmogorov scale.

5.7 Accuracy assessment

The accuracy analysis for stereoscopic PIV systems has long been considered a challenge due to its complexity and involvement of numerous hardware components and computational correlation. Time-resolved stereoscopic scanning PIV, TR-SSPIV, is a far more complex system and thus a complete accuracy assessment is necessary. The sources of error can be categorized into three main types: a) errors from experimental setup and procedure b) errors from image processing correlation c) numerical computation.

The largest error in the experimental configuration comes from the projection of 3D world coordinates to 2D image coordinates. This geometric error relates closely to the camera viewing angles and calibration process. Lawson & Wu 1997 performed both theoretical analysis and experimental investigation on the geometric error of stereoscopic PIV system. Their study suggested that the in-plane velocity measurement bears minimum error when the cameras have minimum included angle, while the out-of-plane velocity error is minimum when the cameras are 90 degrees apart. An optimal error condition is found to be when the camera angle is 40-50 degrees. Coudert et al. 2000 performed PIV measurements with different camera angle combination and concluded that higher accuracy is obtained when the two cameras are located symmetrically with respect to the laser sheet.

In the current study, the two cameras were kept at 29 degree and 30 degree to minimize the error ratio, which is defined as the ratio between the standard deviation of out-of-plane velocity and that of the in-plane velocity $e_r = \delta(\Delta z)/\delta(\Delta x)$ (Lawson & Wu 1997).

Table 5.7 shows the RMS velocity fluctuations in all three directions and the calculated error ratio is 1.6. This value is consistent with the results by Lawson & Wu 1997 and Mullin & Dahm 2006.

Another possible error in the experimental configuration is related to the calibration, when the target plane is not perfectly aligned with the laser sheet. As mentioned in §2.4, this disparity was corrected by taking particle images simultaneously with both cameras. The displacement obtained after applying the mapping correlation is used to correct the calibration polynomial. This process can eliminate the disparity down to the order of 0.01 pixel (Wieneke 2005). Given that the current average particles move 12 pixels in the x -direction, the error caused by misalignment is less than 0.1% and is negligible. Moreover, large F number (#16) scheinplugs were used to eliminate the out-of-focus effect and image distortion.

The errors generated during image processing cross-correlation include the outliers, the mean-bias errors and RMS errors (Huang et al. 1997). In the present study, a 3×3 median filter is applied to the vector field to remove the outliers (random uncorrelated vector). The other two errors are in the order of 0.1 pixel (Huang et al. 1997). Since these errors generally remain the same regardless of the experimental conditions, a higher displacement is preferred to reduce the error. For instance, a relatively large Δt is chosen to maximize the velocity displacement. An interrogation shifting is applied and the particles moved about 12 pixels in the x -direction and 3 pixels in the y - and z -directions. This makes the cross-correlation in the current system to be 2% in the x -direction and 6%

in the y - and z -directions. Note that a larger displacement is not suitable considering that the particles would move out of the laser sheet plane, which would result in a failed correlation.

The complete nine velocity gradient components are computed using discrete differential methods, which also generates numerical errors. The accuracy of velocity gradient measurements are tested by comparing the calculated values with the mass conservation equation for incompressible flow. Figure 5.21 shows the PDFs of the out-of-plane velocity gradient $\partial w/\partial z$, with measured data and derived data from $\partial w/\partial z = -\partial u/\partial x - \partial v/\partial y$. As shown in the figure, the two PDFs collapse with each other and show very good agreement. The scaling factors for the two tails were off by only 1%.

Next a local divergence error defined as $\xi = \frac{(\partial u/\partial x + \partial v/\partial y + \partial w/\partial z)^2}{(\partial u/\partial x)^2 + (\partial v/\partial y)^2 + (\partial w/\partial z)^2}$ is computed

and the PDF is shown in Fig. 5.22. Mass conservation requires $\xi = 0$, and the PDF shows the highest peak occurs at 0 and drastically decreases with some high value ξ . The mean value of ξ is 0.3. The result is comparable to Zhang et al. 2007 where the mean values are 0.12-0.74.

Another way to quantify the local divergence error is to scale the divergence of velocity $\nabla \cdot u$ by the norm of local velocity gradient tensor $(\nabla u : \nabla u)^{1/2}$ (Mullin & Dahm 2006). Figure 5.23a shows the PDF of this ratio, and the mean was 0 with an RMS of 0.4. This is consistent with the RMS value of 0.35 by Mullin & Dahm 2006 and 0.25 by Ganapathisubramani et al. 2007. Further analysis includes plotting the joint PDF of the

divergence error ratio with the norm of velocity gradient tensor, as shown in Fig. 5.23b. The divergence error appears to be higher when the norm of velocity gradient is lower, which indicates that the measurement is more accurate with high velocity gradient, where the intense sheet-like structures are present.

To check the repeatability and reliability of the TR-SSPIV system, an experiment (Case 4) was done at the exact same downstream and radial location of the same turbulent jet as in Case 1, except for the camera configuration. As shown in Fig. 5.1c, the laser sheets are perpendicular to the jet centerline and the cameras are looking at the cross section of the jet. The PDFs of the same component of velocity gradient for the two cases are plotted in Fig. 5.24. The profiles are near identical, which proves the repeatability of the experiment and the reliability of the TR-SSPIV system.

A final check of the accuracy of the measurements included comparing the energy dissipation rate measured to various isotropic assumption and experimental correlations, as illustrated in Table 5.8. Since the current TR-SSPIV system provides the complete velocity gradient tensor, the energy dissipation rate can be calculated by its definition $\varepsilon \equiv 2\nu s_{ij}s_{ij}$. Compared to the experimental correlation using centerline velocity and local outer length scale (Papanicolaou & List 1988), the difference of the value is 4%. If the flow were completely homogenous isotropic, the energy dissipation rate can be calculated using $\varepsilon = 15\nu \overline{(\partial u / \partial x)^2}$ (Saarenrinne & Piirto 2000), the difference is 3%. Some other estimation of the energy dissipation rate was done (George & Hussein 1991, Tanaka &

Eaton 2007) due to the lack of 3D3C velocity measurement, and the difference is within 5% among all.

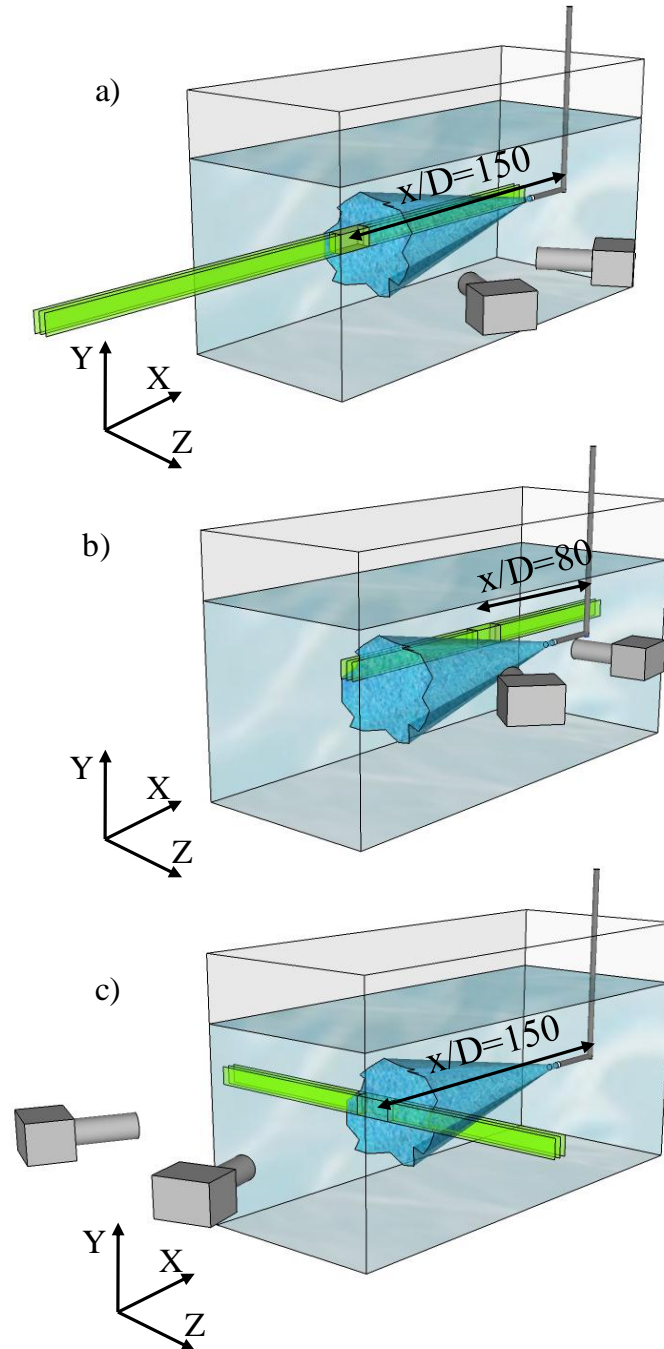


Figure 5.1. Schematic of the four measurement configurations: a) $x/D=150$ downstream jet centerline side-view (Case 1 and 2); b) $x/D=80$ downstream off-centerline side-view (Case 3) c) $x/D=150$ downstream jet cross-view (Case 4).

Component	Present data	Mullin & Dahm 2006	Ganapathisubramani et al. 2007	Homogeneous isotropy value
$\overline{\left(\frac{\partial u}{\partial y}\right)^2} / \overline{\left(\frac{\partial u}{\partial x}\right)^2}$	2.014	1.932	1.455	2
$\overline{\left(\frac{\partial u}{\partial z}\right)^2} / \overline{\left(\frac{\partial u}{\partial x}\right)^2}$	1.991	1.816	1.629	2
$\overline{\left(\frac{\partial v}{\partial x}\right)^2} / \overline{\left(\frac{\partial v}{\partial y}\right)^2}$	1.724	1.890	2.051	2
$\overline{\left(\frac{\partial v}{\partial z}\right)^2} / \overline{\left(\frac{\partial v}{\partial y}\right)^2}$	2.103	2.064	1.997	2

Table 5.1 Measured ratios of mean square velocity gradients, also showing results from Mullin and Dahm 2006, Ganapathisubramani et al. 2007 and from homogeneous isotropic theory for comparison.

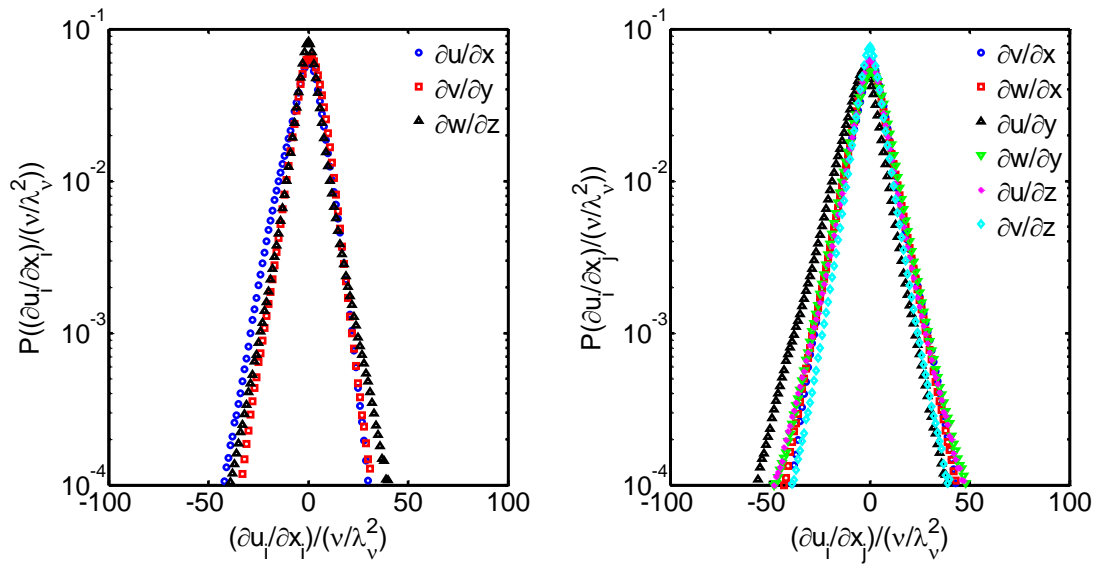


Figure 5.2. PDF of (a) three on-diagonal and (b) six off-diagonal velocity gradients for Case 1 ($Re_D=1500$, $x/D=150$, centerline side-view).

α	$\partial u/\partial x$	$\partial v/\partial x$	$\partial w/\partial x$	$\partial u/\partial y$	$\partial v/\partial y$	$\partial w/\partial y$	$\partial u/\partial z$	$\partial v/\partial z$	$\partial w/\partial z$
Left	0.068	0.067	0.068	0.067	0.064	0.068	0.068	0.067	0.068
Right	0.095	0.102	0.102	0.101	0.095	0.100	0.101	0.102	0.102

Table 5.2. Scaling exponent α of left and right tails of the 9 velocity gradient PDFs for Case 1.

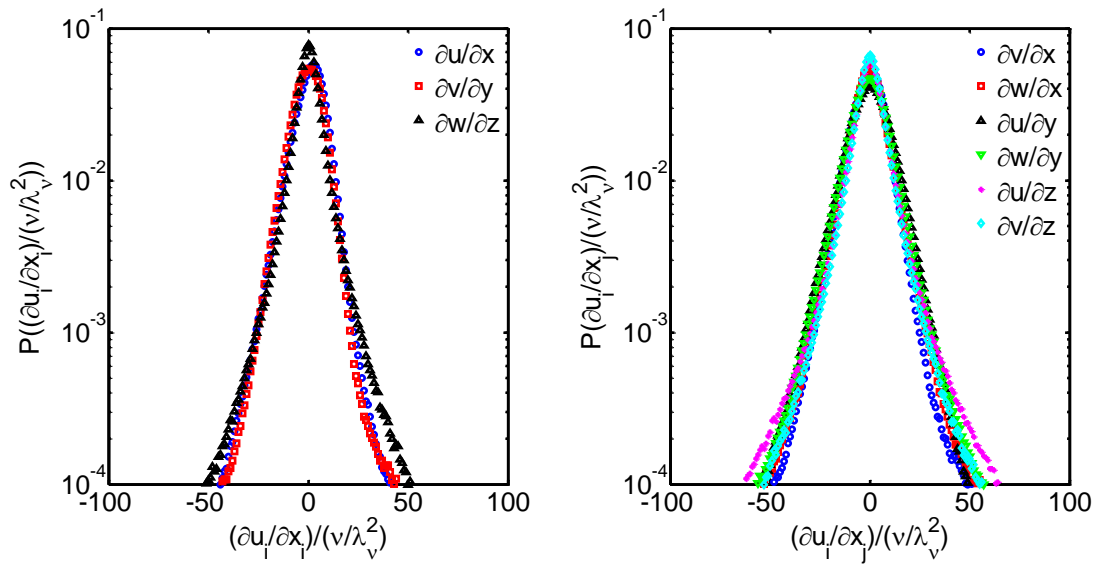


Figure 5.3. PDF of (a) three on-diagonal and (b) six off-diagonal velocity gradients for Case 2 ($Re_D=3000$, $x/D=150$, centerline side-view).

α	$\partial u/\partial x$	$\partial v/\partial x$	$\partial w/\partial x$	$\partial u/\partial y$	$\partial v/\partial y$	$\partial w/\partial y$	$\partial u/\partial z$	$\partial v/\partial z$	$\partial w/\partial z$
Left	0.066	0.064	0.062	0.061	0.066	0.060	0.057	0.062	0.063
Right	0.080	0.073	0.067	0.073	0.077	0.066	0.059	0.066	0.073

Table 5.3. Scaling exponent α of left and right tails of the 9 velocity gradient PDFs for Case 2.

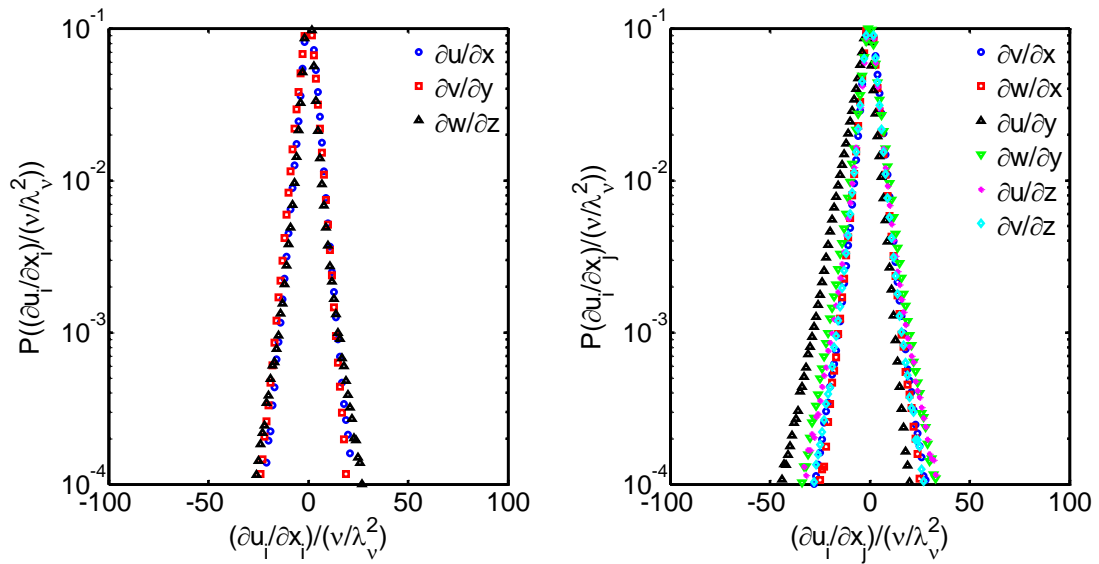


Figure 5.4. PDF of (a) three on-diagonal and (b) six off-diagonal velocity gradients for Case 3 ($Re_D=1500$, $x/D=80$, off-centerline side-view).

α	$\partial u/\partial x$	$\partial v/\partial x$	$\partial w/\partial x$	$\partial u/\partial y$	$\partial v/\partial y$	$\partial w/\partial y$	$\partial u/\partial z$	$\partial v/\partial z$	$\partial w/\partial z$
Left	0.146	0.141	0.145	0.119	0.145	0.137	0.137	0.141	0.143
Right	0.150	0.139	0.147	0.150	0.153	0.132	0.132	0.145	0.145

Table 5.4. Scaling exponent α of left and right tails of the 9 velocity gradient PDFs for Case 3.

Component	Present data	Mullin & Dahm 2006	Ganapathisubramani et al. 2007	Axisym. isotropy value
$\overline{\left(\frac{\partial u}{\partial y}\right)^2} / \overline{\left(\frac{\partial u}{\partial z}\right)^2}$	1.09	1.07	0.893	1
$\overline{\left(\frac{\partial v}{\partial y}\right)^2} / \overline{\left(\frac{\partial w}{\partial z}\right)^2}$	0.981	0.937	1.01	1
$\overline{\left(\frac{\partial v}{\partial y}\right)^2}$	1.09	0.937	0.855	1
$\left[\frac{1}{3} \overline{\left(\frac{\partial u}{\partial x}\right)^2} + \frac{1}{3} \overline{\left(\frac{\partial v}{\partial z}\right)^2} \right]$				

Table 5.5. Measured ratios of mean square velocity gradients, also showing results from Mullin & Dahm 2006, Ganapathisubramani et al. 2007 and from axisymmetric isotropic theory for comparison.

	$\partial u/\partial x$	$\partial v/\partial y$	$\partial w/\partial z$	$\partial u_i/\partial x_j, i \neq j$
			Skewness	
Present Work ($Re_\lambda=44$)	-0.43	-0.30	-0.15	-0.15 - 0.12
Mullin & Dahm 2006 ($Re_\lambda=45$)	-0.43	-0.38	-0.14	-0.22 - 0.03
Gulitski et al.2007 ($Re_\lambda=1600$)	-0.46	-0.35	-0.29	0.01 - 0.14
			Kurtosis	
Present Work ($Re_\lambda=44$)	4.5	5.2	4.8	4.2-8.4
Mullin & Dahm 2006 ($Re_\lambda=45$)	4.2	3.8	4.5	4.2 - 6.0
Gulitski et al. 2007 ($Re_\lambda=1600$)	5 - 13	5 - 13	5 - 13	5 - 13

Table 5.6. Comparison of present measured velocity gradient moment skewness and kurtosis with other work.

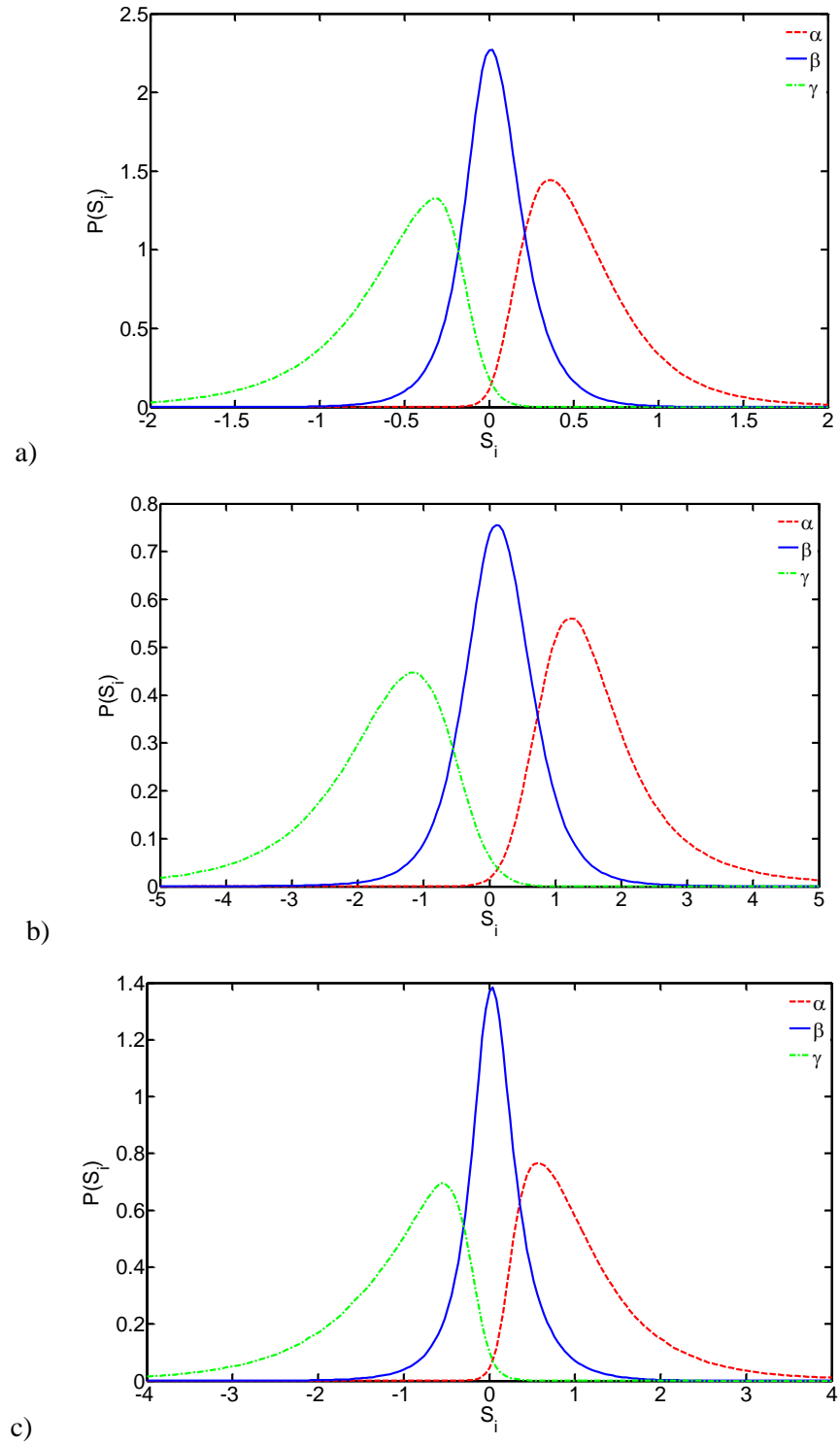


Figure 5.5. PDF of three principal strain rates α, β, γ for the Case 1-3. The values of principal strain rates are not normalized. The unit is 1/s.

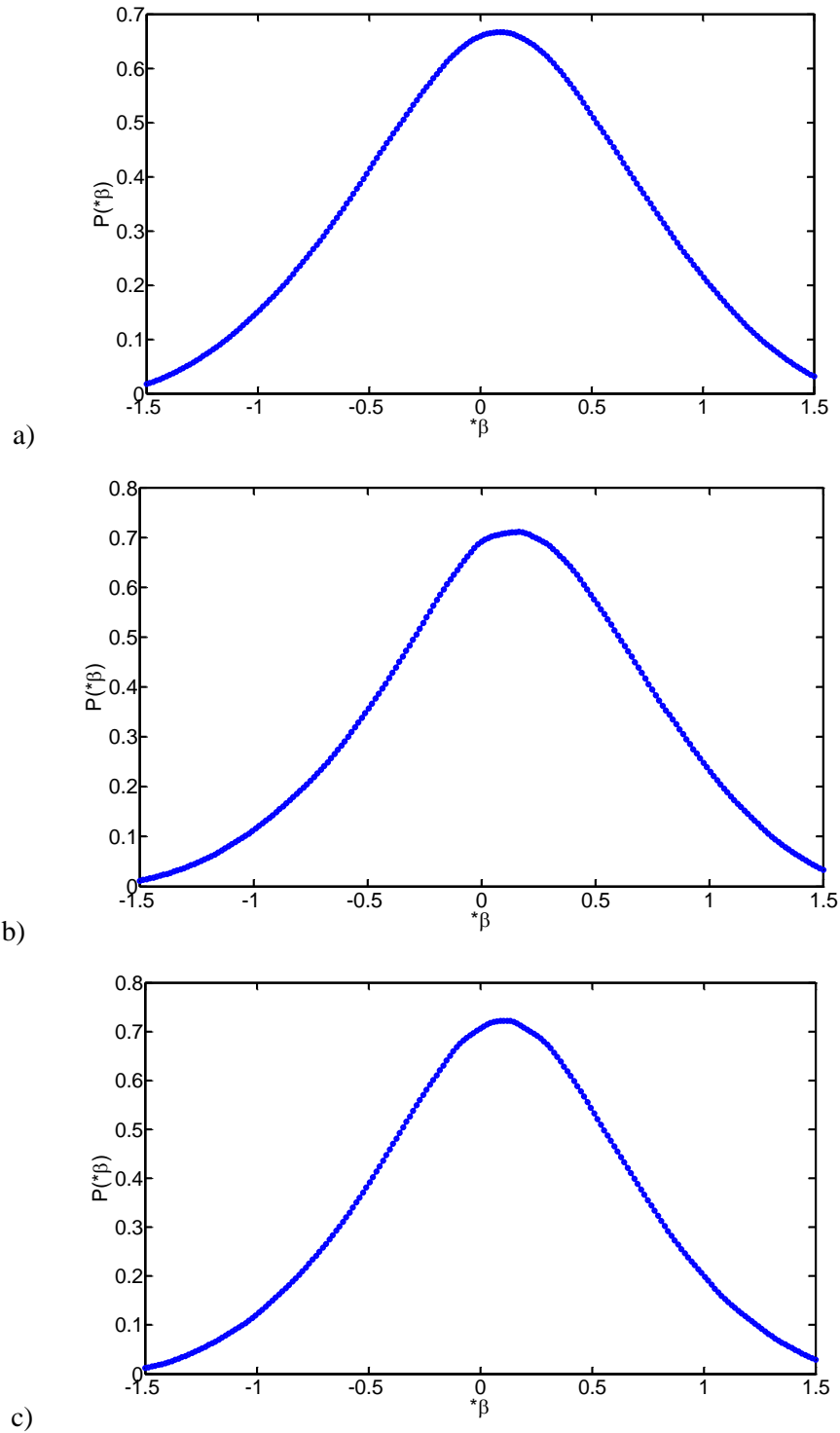


Figure 5.6. PDF of normalized intermediate strain rate for Case 1-3.

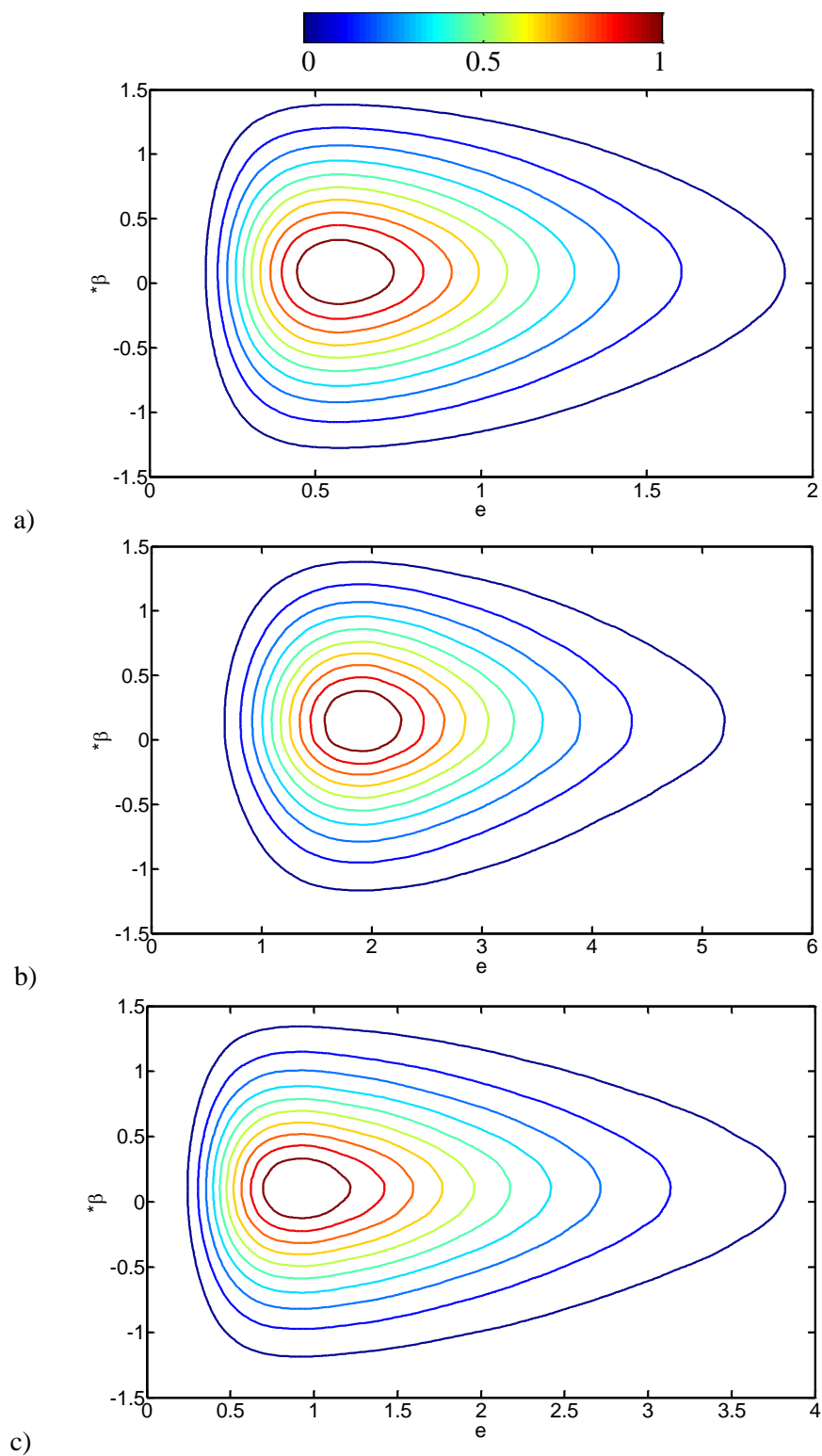


Figure 5.7. Joint PDF of magnitude of strain rate tensor e and intermediate strain rate $*\beta$ for Case 1-3. Unit of e is 1/s. The contour lines are from 0 to 1 with increment of 0.1.

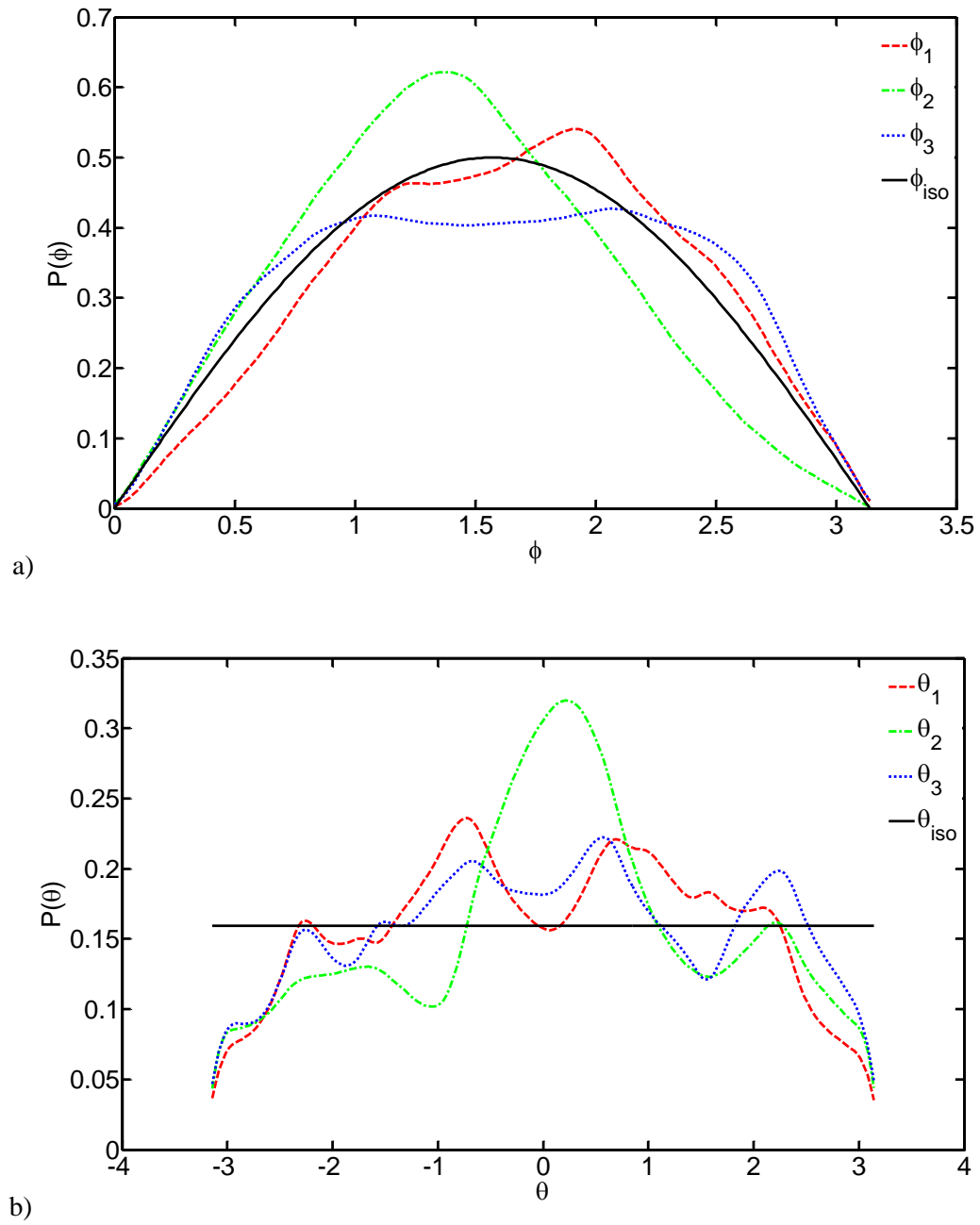


Figure 5.8. PDF of the orientation angle of ϕ and θ for three principal strain axes e_i for Case 1.

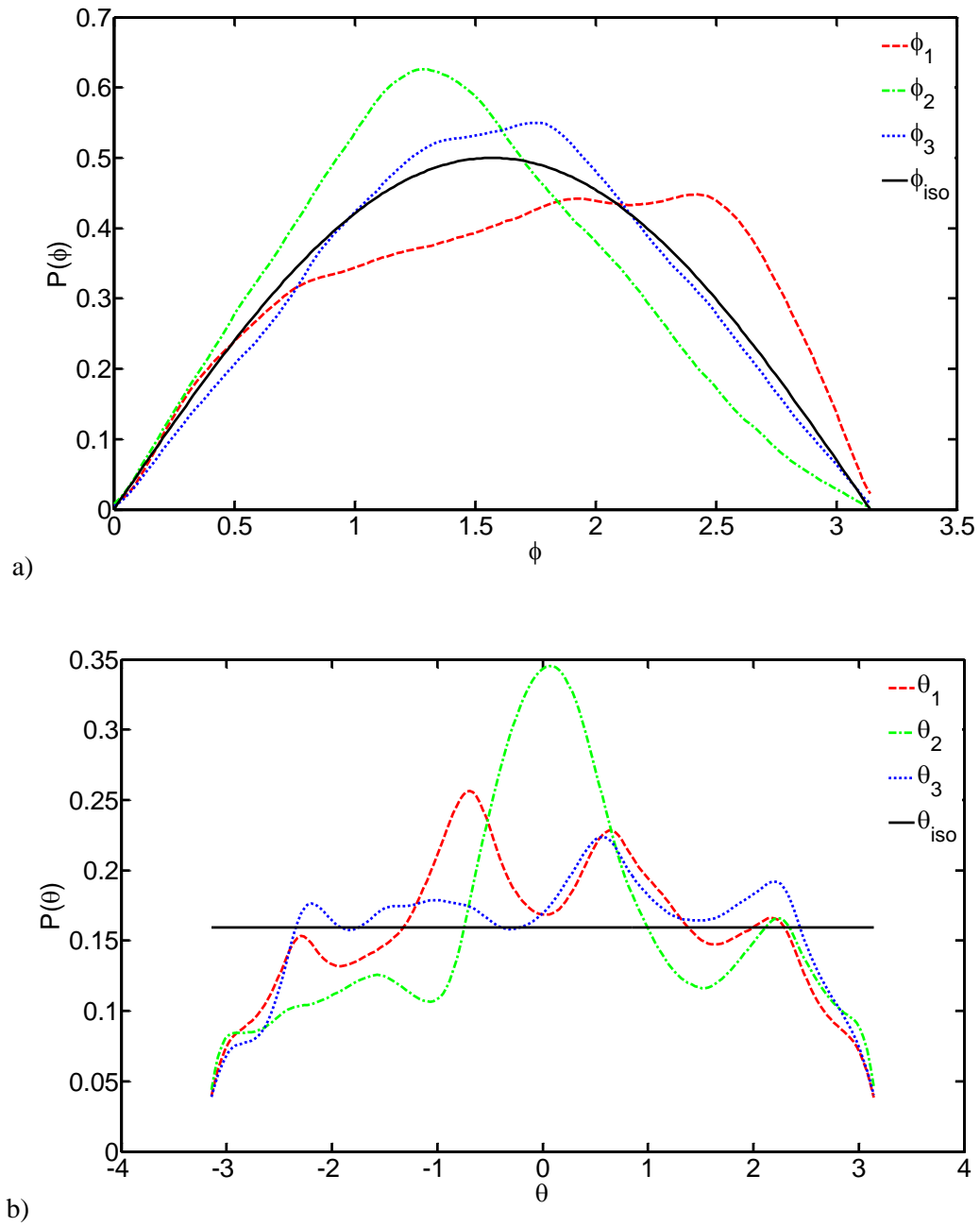


Figure 5.9. PDF of the orientation angle of ϕ and θ for three principal strain axes e_i for Case 2.

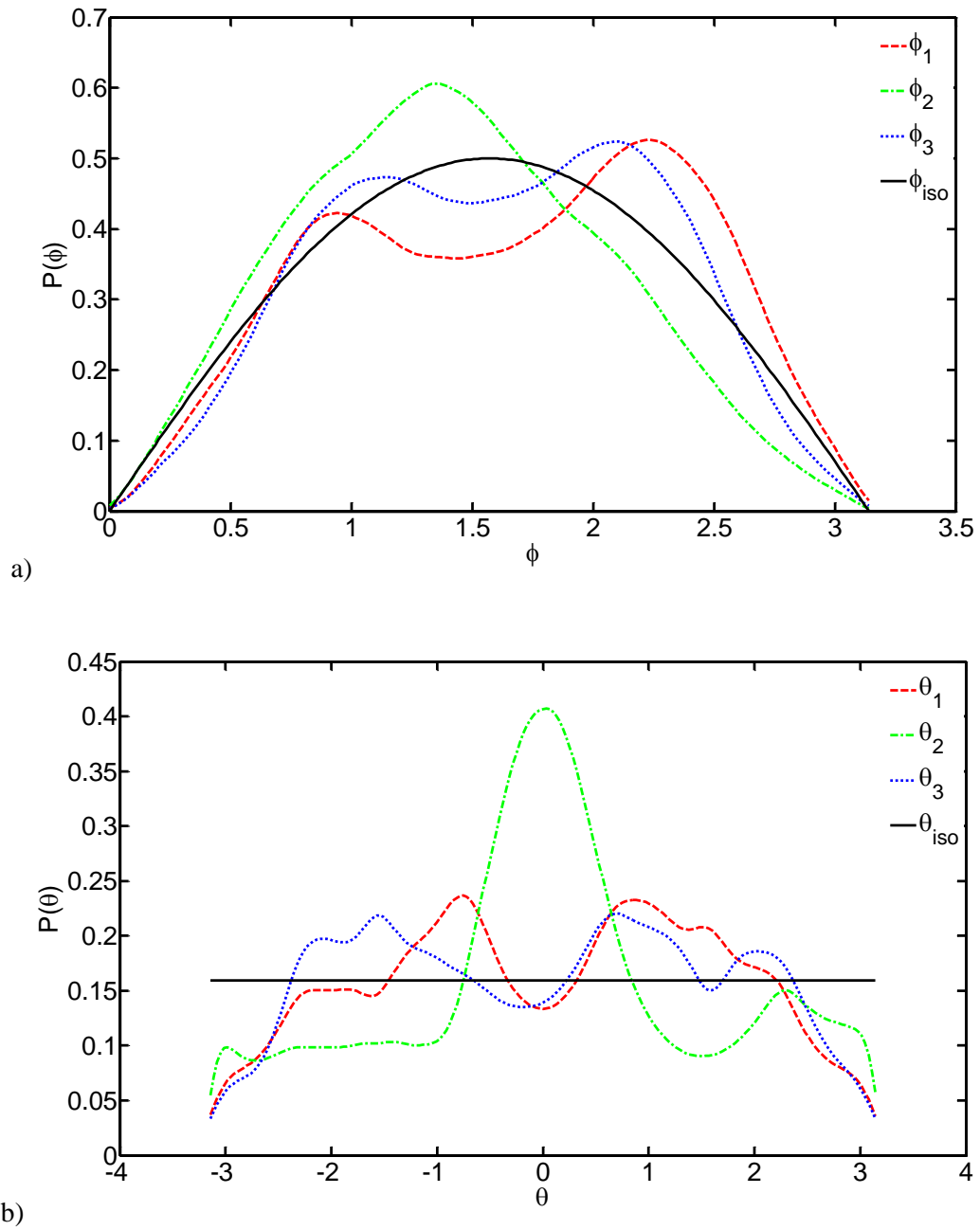


Figure 5.10. PDF of the orientation angle of ϕ and θ for three principal strain axes e_i for Case 3.

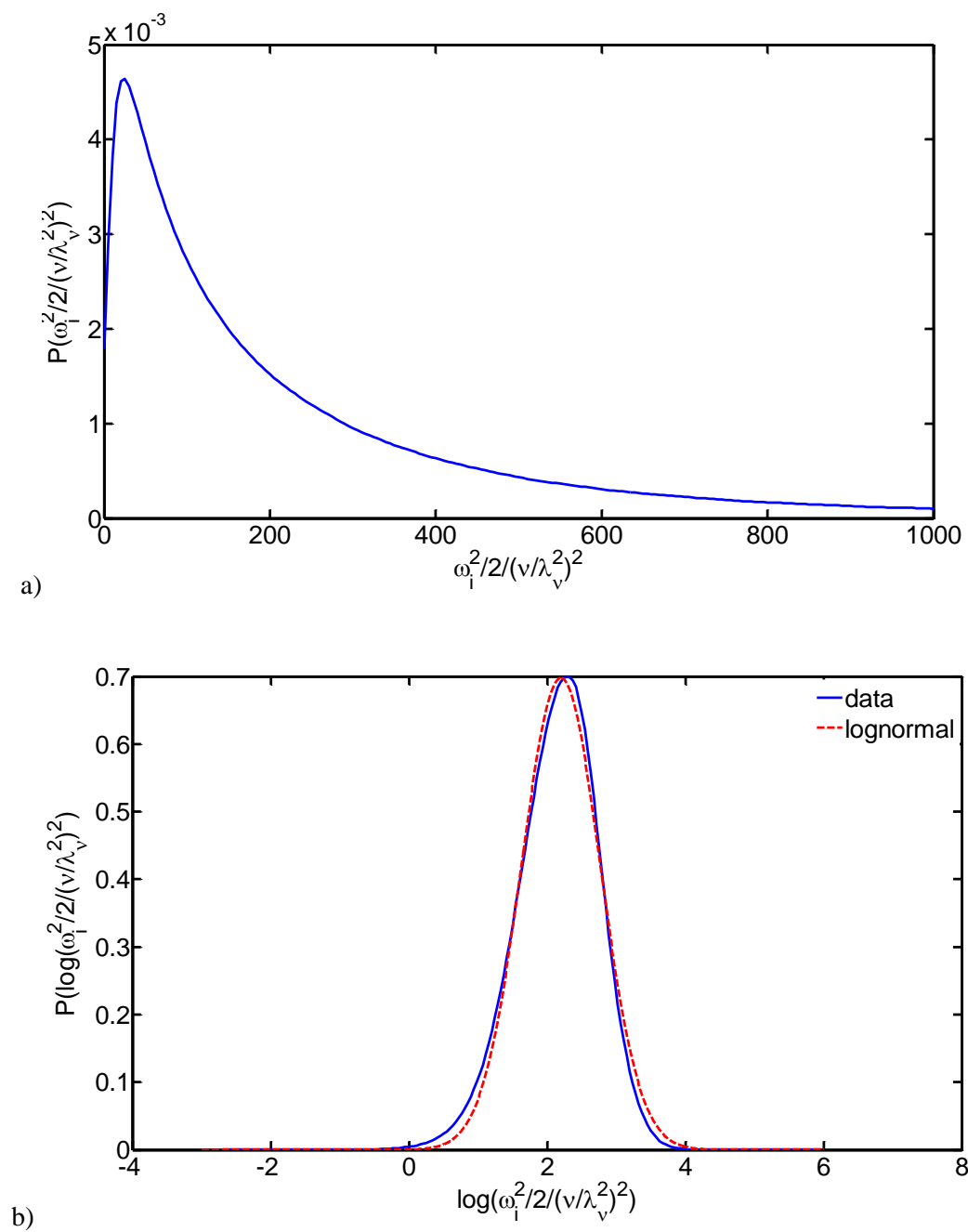


Figure 5.11. PDF of enstrophy field with log normal fits for Case 1.

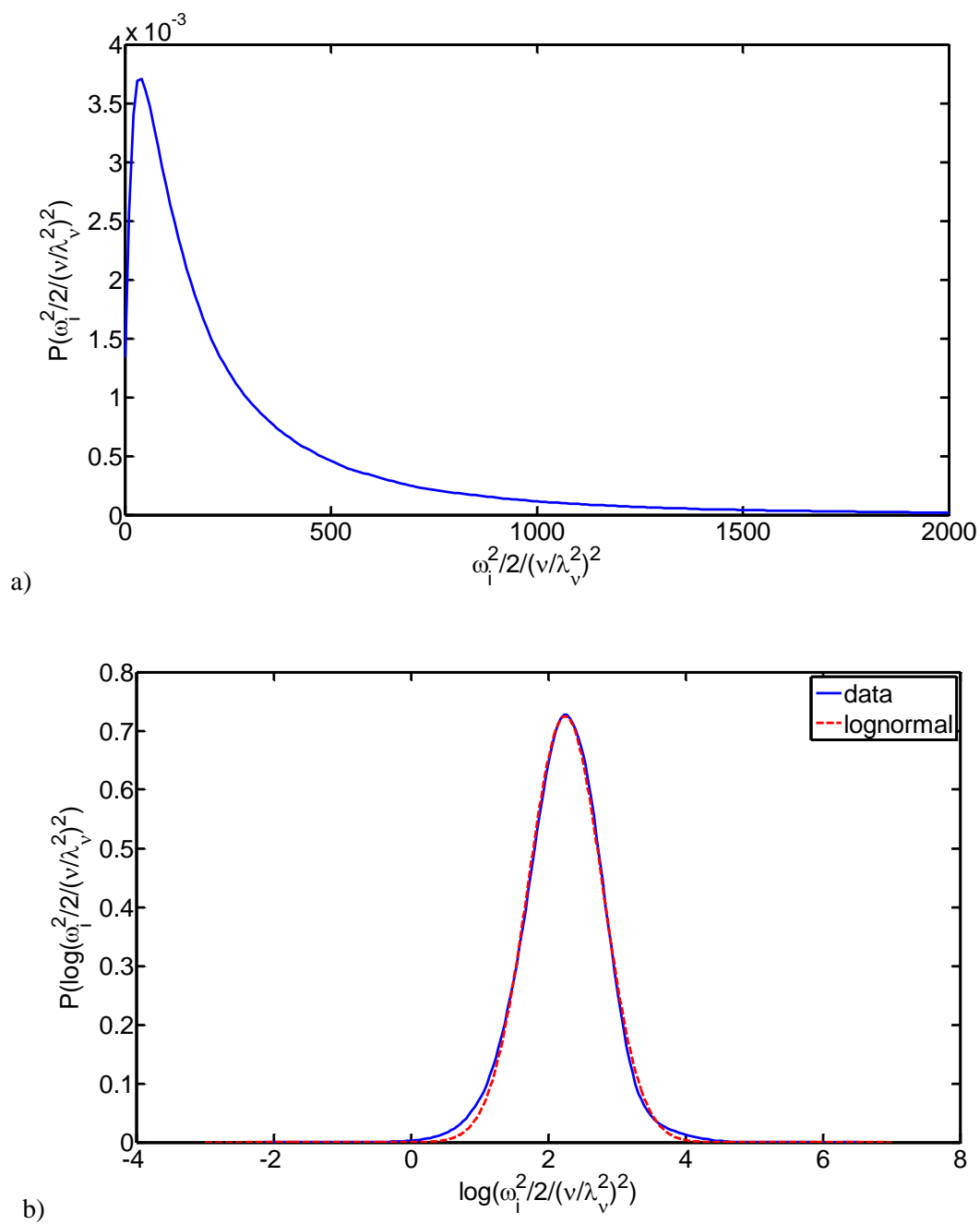


Figure 5.12. PDF of enstrophy field with log normal fits for Case 2.

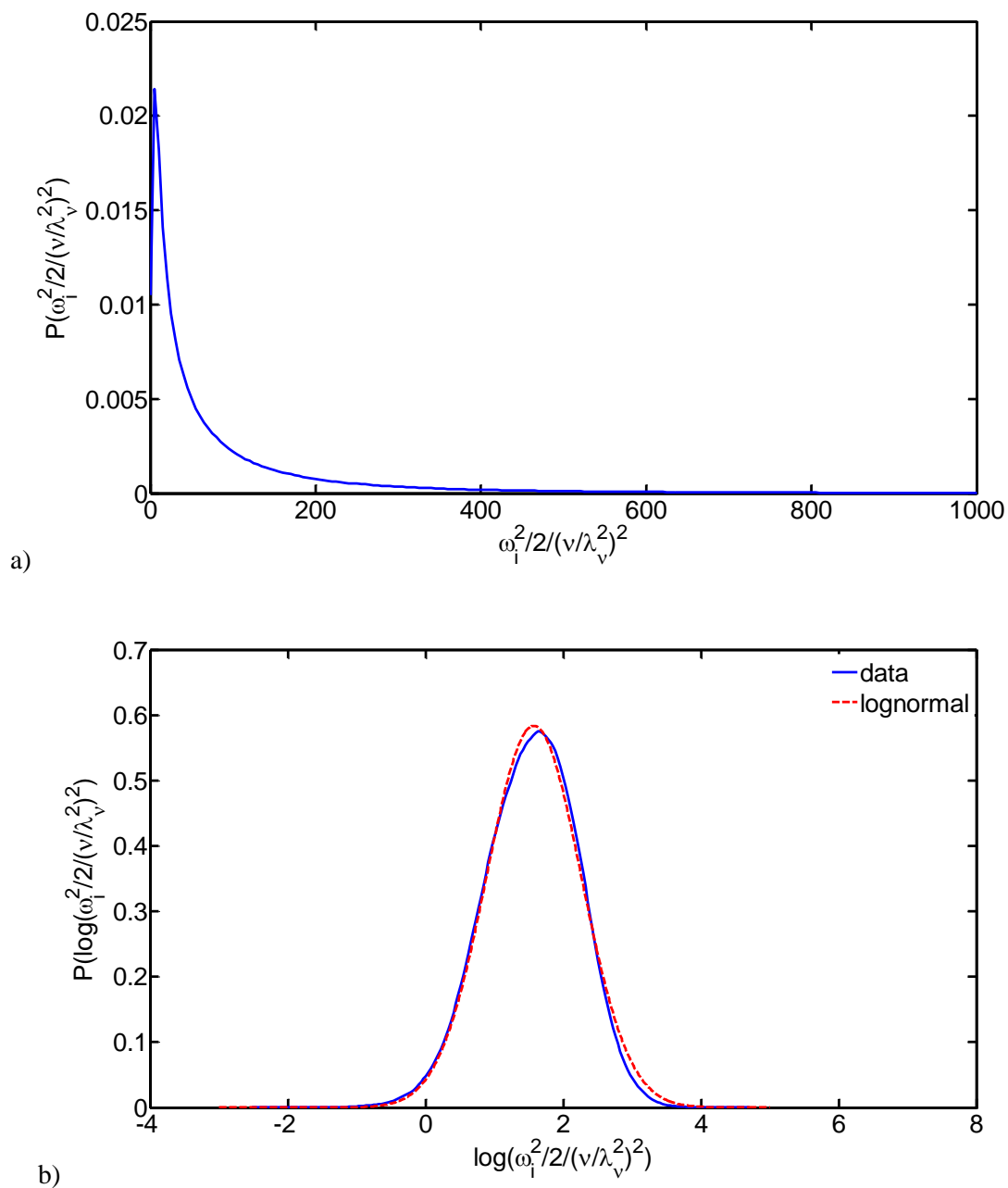


Figure 5.13. PDF of enstrophy field with log normal fits for Case 3.

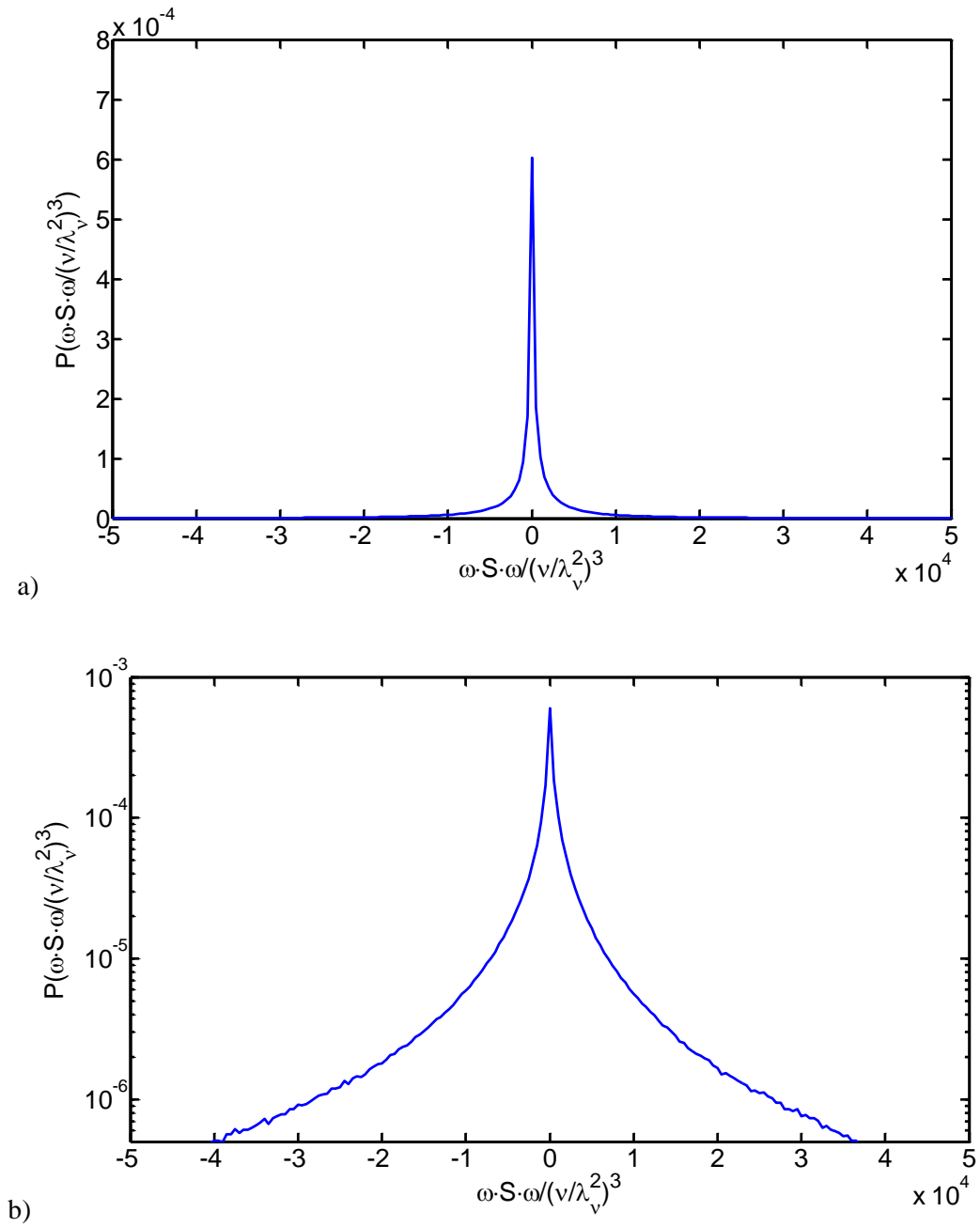


Figure 5.14. PDF of enstrophy production rate field with log normal fits for Case 1.

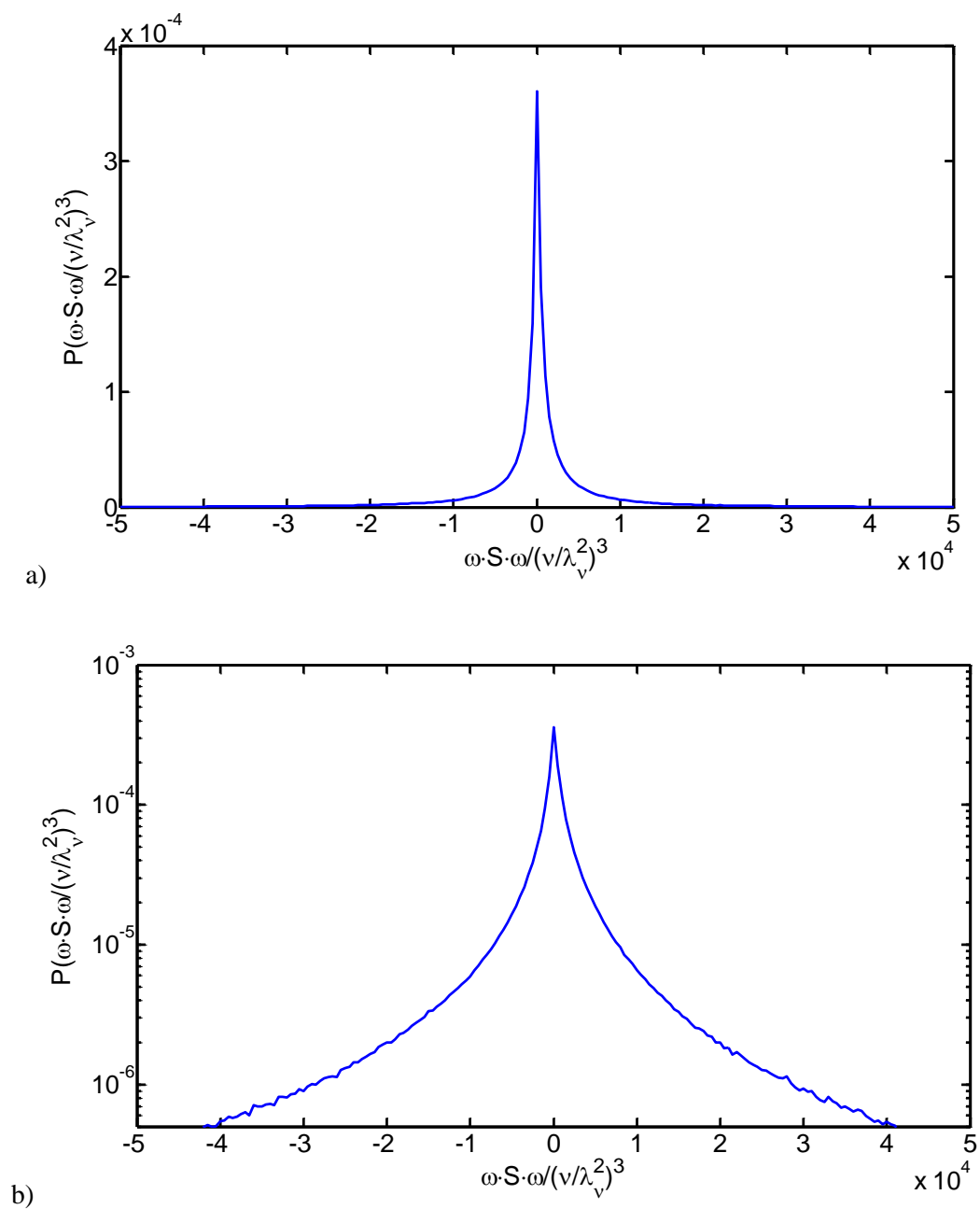


Figure 5.15. PDF of enstrophy production rate field with log normal fits for Case 2

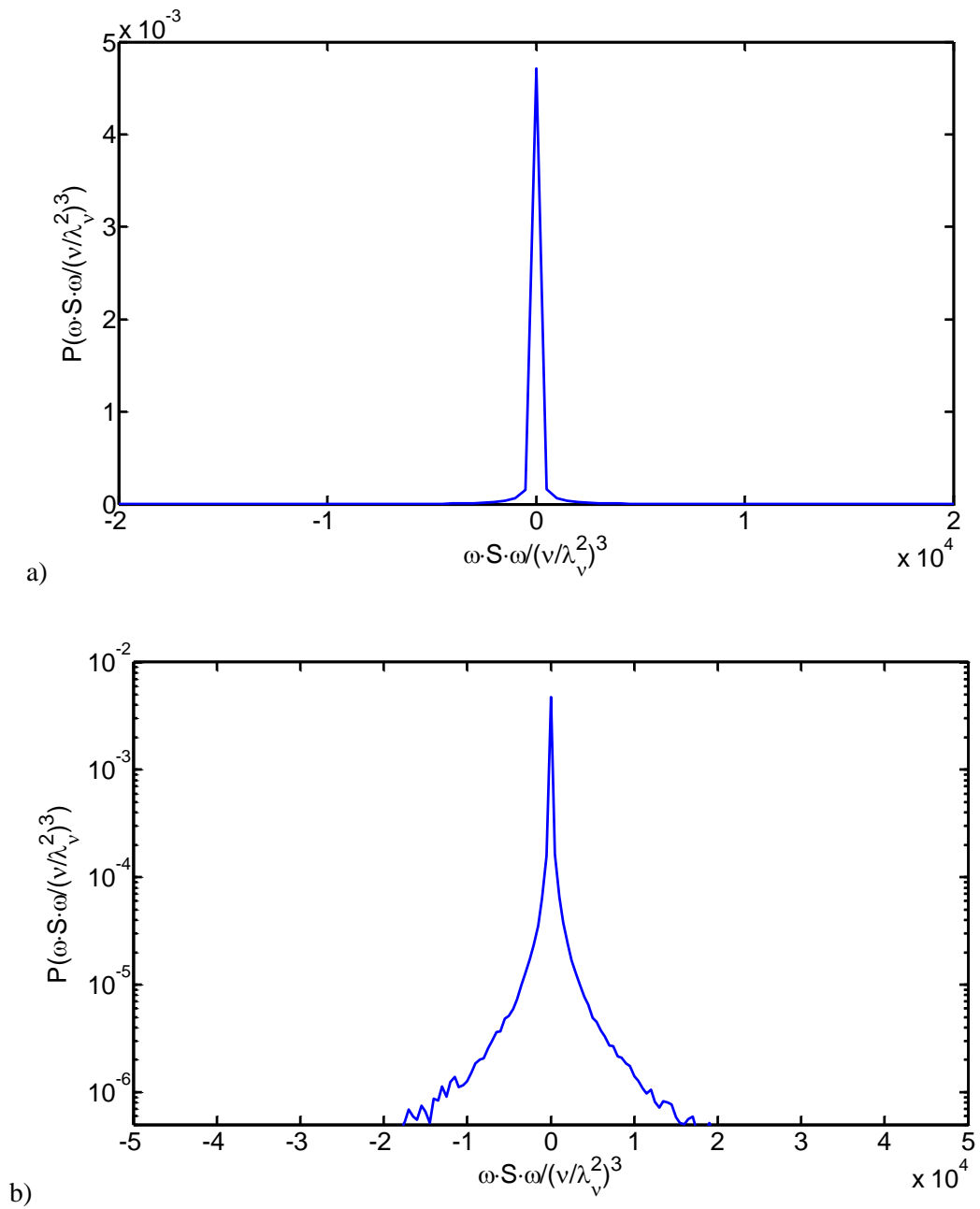


Figure 5.16. PDF of entrophy production rate field with log normal fits for Case 3.

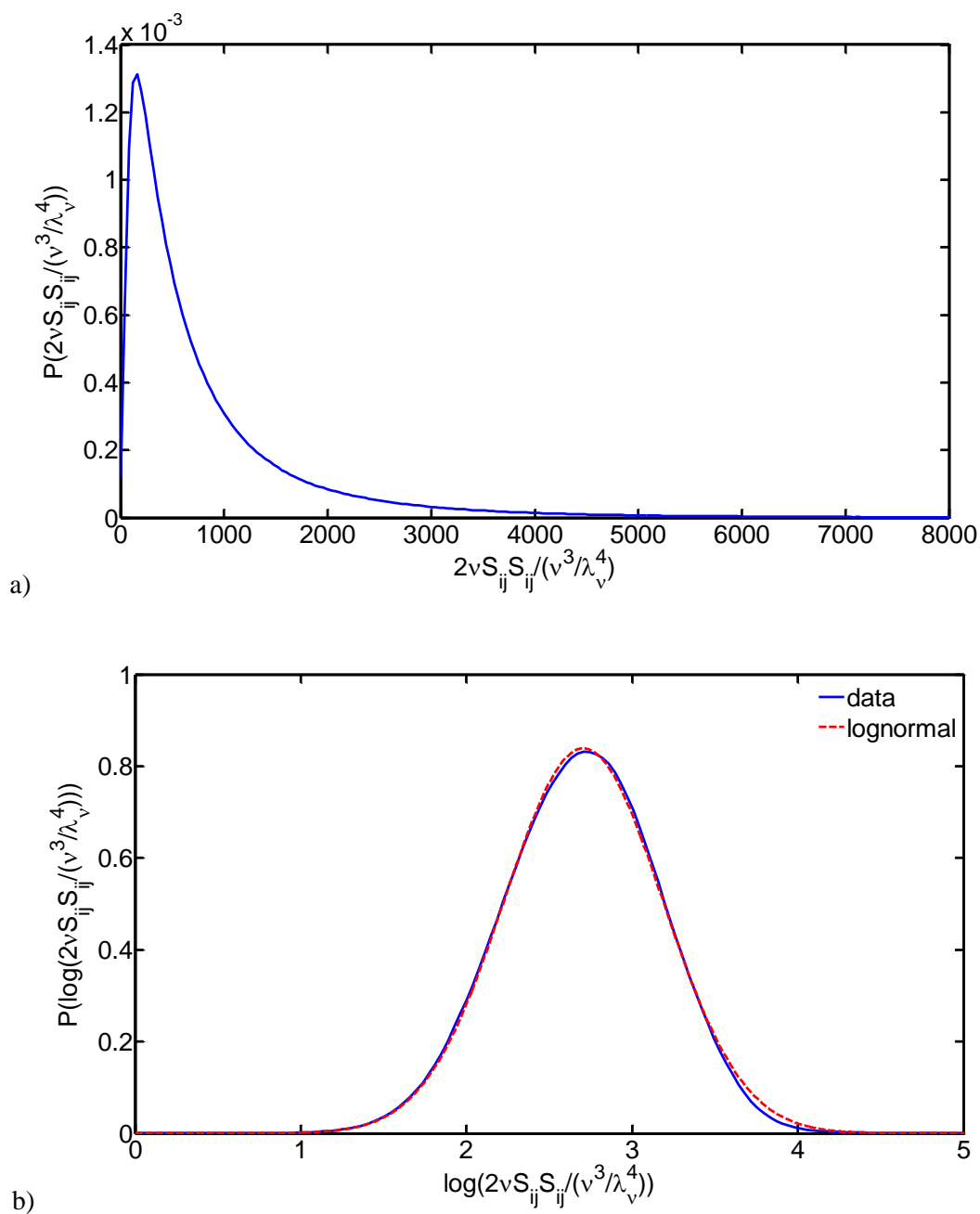


Figure 5.17. PDF of energy dissipation rate with log normal fits for Case 1.

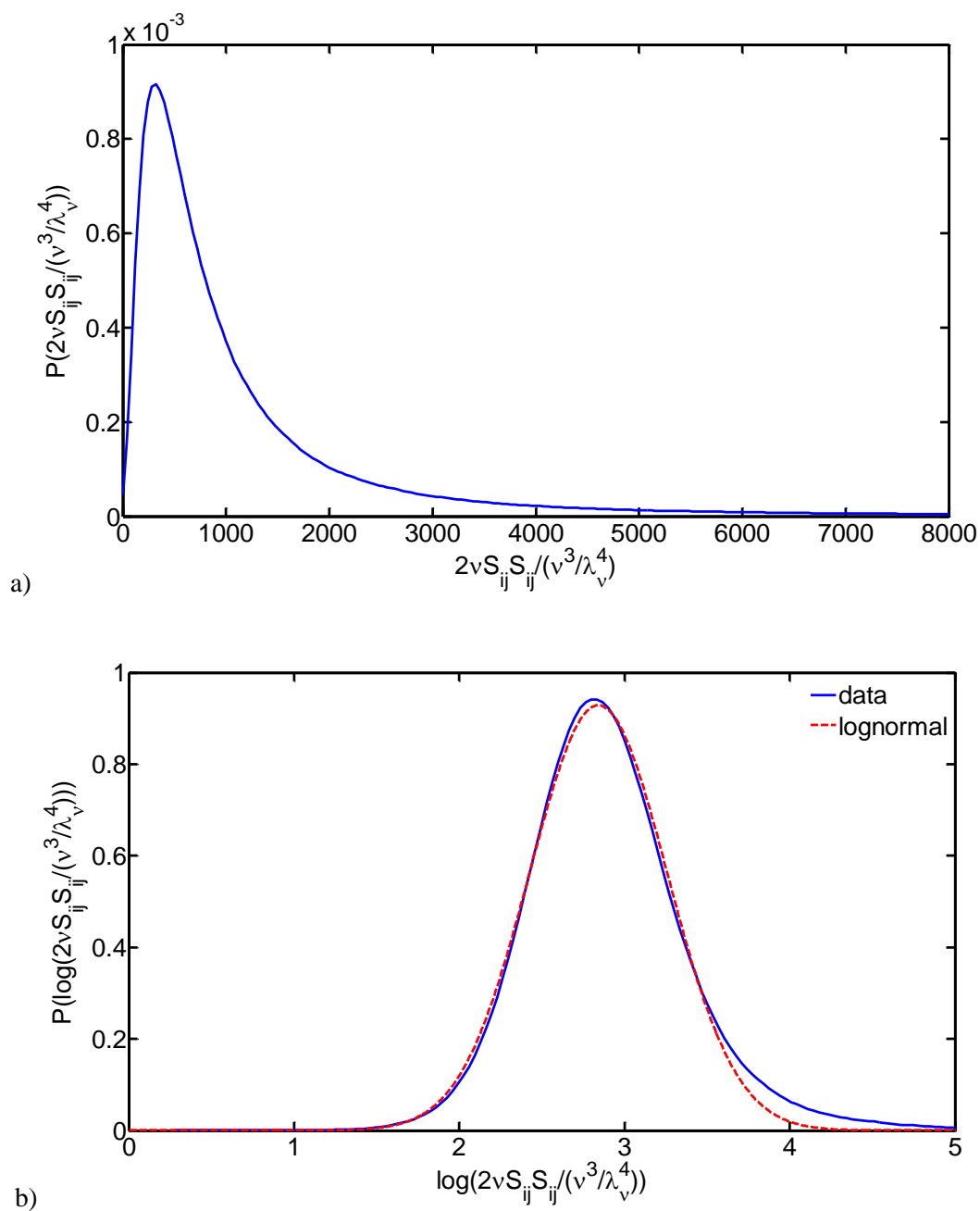


Figure 5.18. PDF of energy dissipation rate with log normal fits for Case 2.

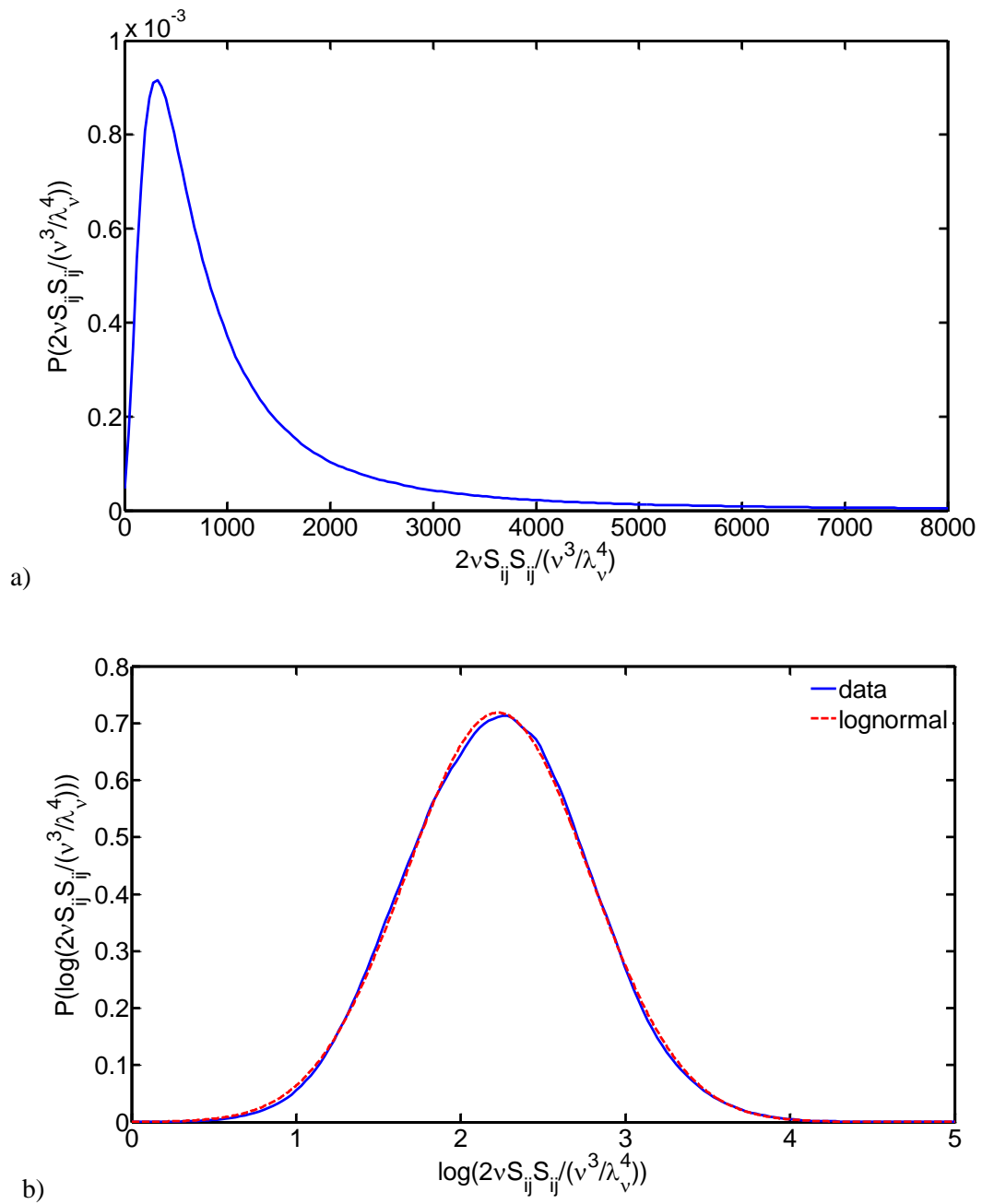


Figure 5.19. PDF of energy dissipation rate with log normal fits for Case 3.

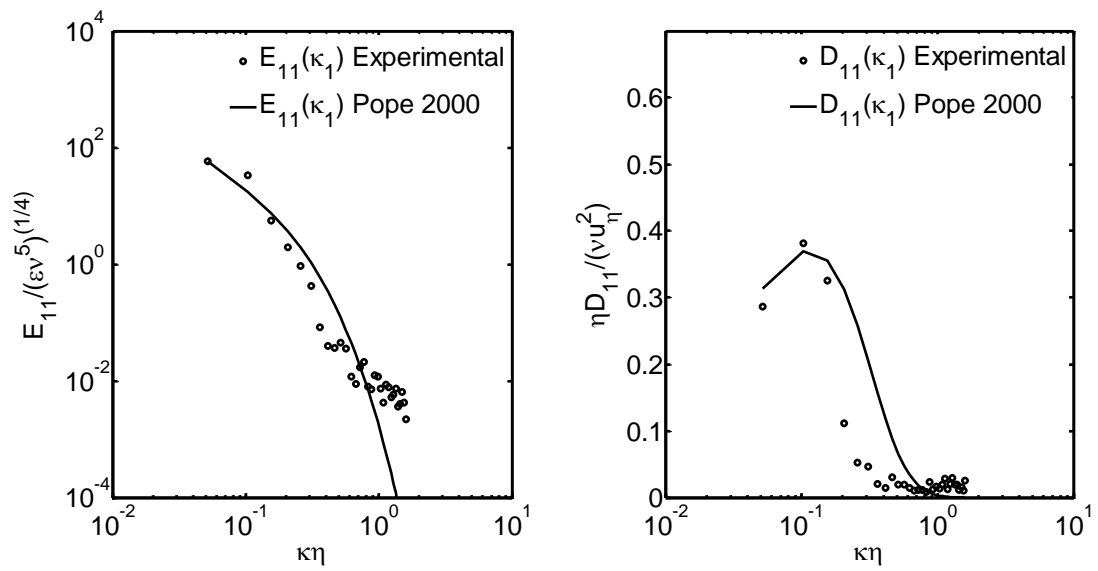


Figure 5.20. a) Energy and b) dissipation spectra of streamwise velocity compared to the model spectra by Pope 2000.

Parameter	Current data	Mullin & Dahm 2006
u'_{rms}	0.0047	0.006
v'_{rms}	0.0039	0.004
w'_{rms}	0.0069	0.008
Error ratio e_r	1.6	1.8

Table 5.7. RMS velocity fluctuation for each component and the error ratio. The result compares favorably to Mullin & Dahm 2006.

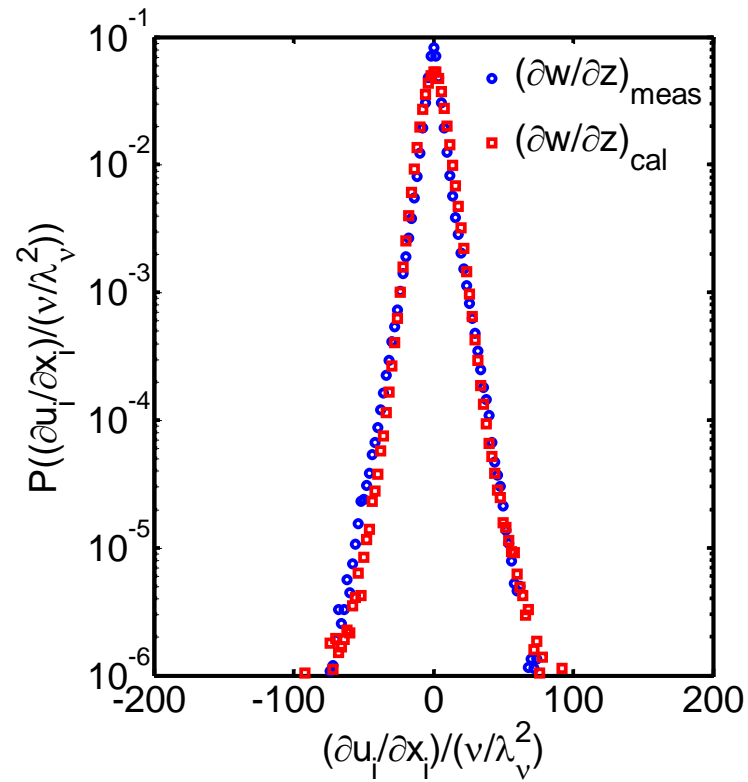


Figure 5.21. PDFs of $\partial w/\partial z$ measured and $\partial w/\partial z$ calculated using mass conservation $\partial u/\partial x + \partial v/\partial y + \partial w/\partial z = 0$.

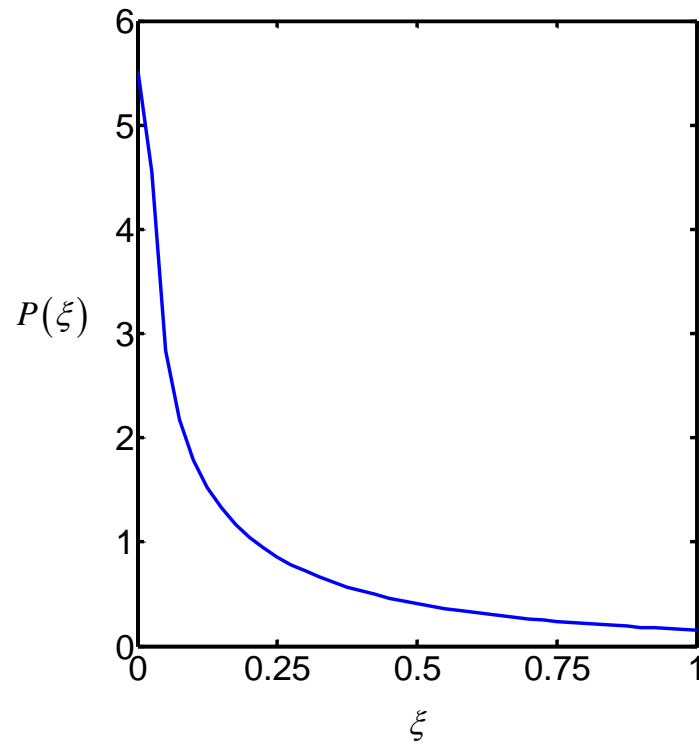


Figure 5.22. PDF of local divergence error defined as $\xi = \frac{(\partial u/\partial x + \partial v/\partial y + \partial w/\partial z)^2}{(\partial u/\partial x)^2 + (\partial v/\partial y)^2 + (\partial w/\partial z)^2}$.
 Mass conservation requires $\xi = 0$.

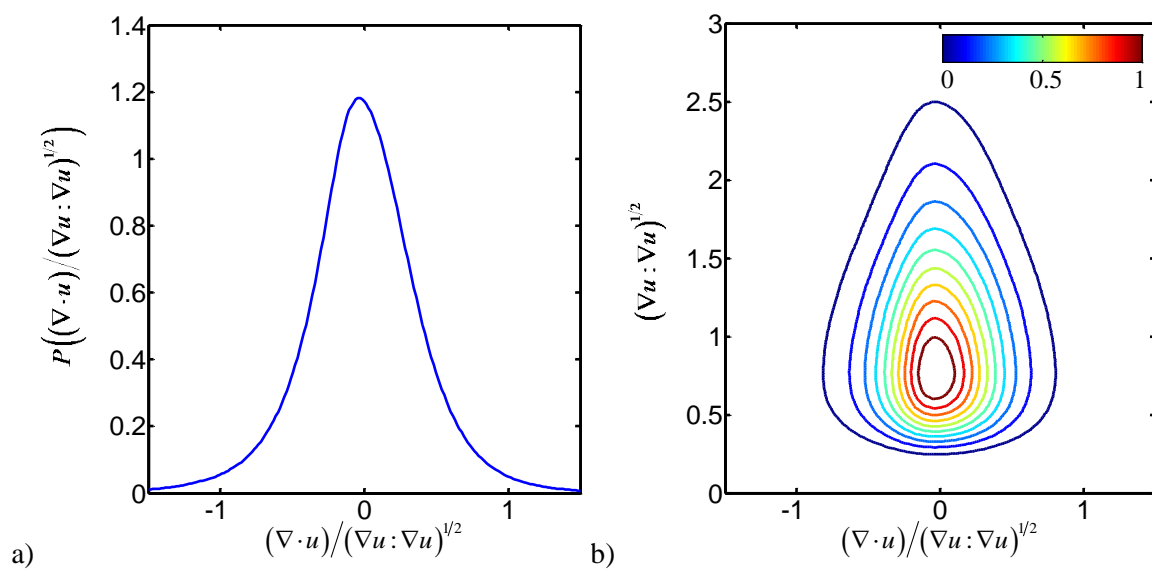


Figure 5.23. a) PDF of local divergence error normalized with norm of velocity gradient tensor; b) Joint PDF of local divergence error and norm of velocity gradient tensor.

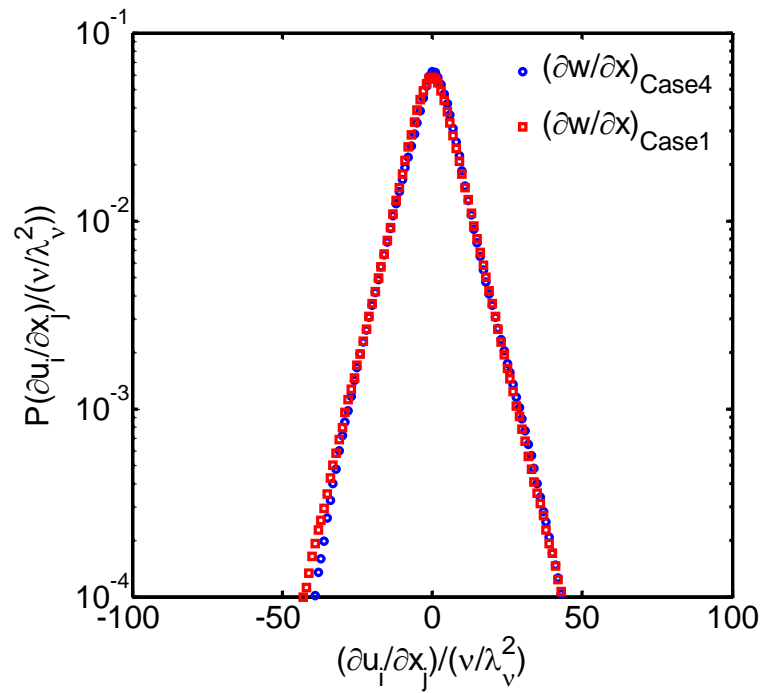


Figure 5.24. PDF of $\partial w / \partial z$ of the same jet downstream location measured with side-view configuration (Case 1) and cross-view configuration (Case 4). They show very good agreement, indicating the reliability of the TR-SSPIV system.

Turbulent kinetic energy dissipation rate	Value $10^{-6} m^2/s^3$
$\varepsilon = 0.08u_c^3/\delta$ (Papanicolaou & List 1988)	3.88
$\varepsilon \equiv 2\nu s_{ij}s_{ij}$ (Definition)	4.04
$\varepsilon = 3\nu \left\{ \overline{\left(\frac{\partial u}{\partial x}\right)^2} + \overline{\left(\frac{\partial v}{\partial y}\right)^2} + \overline{\left(\frac{\partial u}{\partial y} + \frac{\partial v}{\partial x}\right)^2} \right\}$ (Tanaka & Eaton 2007)	4.06
$\varepsilon = \nu \left\{ -\overline{\left(\frac{\partial u}{\partial x}\right)^2} + 2\overline{\left(\frac{\partial u}{\partial y}\right)^2} + 2\overline{\left(\frac{\partial v}{\partial x}\right)^2} + 8\overline{\left(\frac{\partial v}{\partial y}\right)^2} \right\}$ (George & Hussein 1991)	3.87
$\varepsilon = \nu \left\{ \frac{5}{3}\overline{\left(\frac{\partial u}{\partial x}\right)^2} + 2\overline{\left(\frac{\partial u}{\partial z}\right)^2} + 2\overline{\left(\frac{\partial v}{\partial x}\right)^2} + \frac{8}{3}\overline{\left(\frac{\partial v}{\partial z}\right)^2} \right\}$ (George & Hussein 1991)	3.70
$\varepsilon = 15\nu \left\{ \overline{\left(\frac{\partial u}{\partial x}\right)^2} \right\}$ (Saarenrinne & Piirto 2000)	3.93
$\varepsilon = 7.5\nu \left\{ \overline{\left(\frac{\partial u}{\partial z}\right)^2} \right\}$ (Saarenrinne & Piirto 2000)	3.89
$\varepsilon = 6\nu \left\{ \overline{\left(\frac{\partial u}{\partial x}\right)^2} + \overline{\left(\frac{\partial u}{\partial y}\right)^2} + \overline{\left(\frac{\partial u}{\partial y} \frac{\partial v}{\partial x}\right)} \right\}$ (Saarenrinne & Piirto 2000)	4.82

Table 5.8. Energy dissipation rate calculation with different methods and assumptions.

Chapter 6

Concluding Remarks

A time-resolved stereoscopic scanning particle image velocimetry (TR-SSPIV) system is developed, implemented, and applied to investigate free turbulent jets of $Re_\delta = 3200$ and 6400 at both centerline and off-centerline locations. The TR-SSPIV system provided simultaneous 3D3C velocity fields and the complete nine-component velocity gradient tensor. These results are able to provide both quantitative visualization of coherent structures as well as important dynamic properties of turbulence. The major contributions of the current works are listed below.

1. The TR-SSPIV system is applied to the study of turbulence at small scales for the first time. Hori & Sakakibara 2004 developed a similar system to visualize the vorticity structures in a jet. Their resolution, however, was over 10 Kolmogorov length scale η , which is not small enough to resolve fine-scale turbulence. The TR-SSPIV system in the current study was specifically developed to resolve the fine-scale structures with a spatial resolution of $0.6-0.9\eta$, which is among the highest in experimental studies (3η by Ganapathisubramani et al. 2008).

2. With the simultaneous measurement of nine-component velocity gradient tensor, the visualization results revealed the building blocks of complex velocity gradient structures including sheets, tubes, ribbons, and blobs in a three-dimensional volume. Compared to Mullin & Dahm 2006, who also studied small scale turbulent structures but in a 2D plane, the current measurement has the benefits of visualizing the shapes in the 3D domain, which provide better identification of the actual structures.

3. Local acceleration terms were obtained thanks to the high temporal resolution of the TR-SSPIV system. The structures are also visualized in the 3D volume and they showed a strong anti-alignment to the local convection acceleration terms. This experimentally verified the Random Taylor Hypothesis. Ganapathisubramani et al. 2008 was also able to resolve the small scale full velocity gradient structures in a 3D volume, but the acceleration and time evolution of the structure could not be measured due to their system using the Taylor Hypothesis for quasi-instantaneous volume reconstruction.

4. A novel vortex identification algorithm was proposed to detect core of vortical structures. This criterion identifies local low pressure region by solving the Poisson equation for incompressible flow using the full nine-component velocity gradient tensor. This pressure criterion has a high potential in vortex core identification since it provides better defined and restricted boundaries, compared to the current enstrophy, Q , λ_2 and Δ criteria.

5. The statistical analysis along the centerline of the round turbulent jet for two Reynolds number revealed isotropic flow conditions. But the analysis also show that off-axis measurements departed significantly for isotropy. The enstrophy production rate at the interface between the jet and the still fluid was much lower than at the jet centerline. The many results obtained during the statistical analysis also provide experimental support to both DNS and theory of fine-scale turbulence.

6. The measurement of complete nine-component velocity gradient tensor provides the true value of parameters related with important turbulent scaling constants. The kinetic energy dissipation rate is obtained directly and can be used to test the isotropy conditions of the flow by comparing it with results estimated using local homogenous isotropic or axisymmetric isotropic assumptions.

Furthermore, extensive verifications and comparisons with previously published work were completed, including the jet profile validation, RMS velocity fluctuation tests, local divergence error analysis with mass conservation equation, scaling factor comparison of velocity gradient PDFs, repeatability test with different camera configuration. Results are also compared to published works where possible.

The TR-SSPIV system has proven to be an effective and accurate measurement technique in the study of fine-scale turbulence. The system can be applied to the study of other flow behaviors such as turbulent boundary layer and turbulent wakes behind object. Although the goal of the current research is to experimentally resolve the finest scale possible in

turbulence, the TR-SSPIV system is versatile enough to be used on the visualization of 3D flow structures at large scales with minor adjustments. Another goal for the future is to develop a more robust vortex identification scheme. Given the current experimental technique and 3D3C data, the computation of local pressure can be improved in terms of the efficiency and accuracy of the numerical algorithm. The ability of obtaining pressure value with the high resolution grids (60,000 grid points in each domain) through experimental data will help investigating the relationship between pressure distribution and occurrence of vortices, which support the DNS studies and help developing the flow vortex theories.

Bibliography

- J.H. Agui, Y. Andreopoulos, A new laser vorticity probe - LAVOR: Its development and validation in a turbulent boundary layer, *Experiments in Fluids* 34 (2003) 192-205.
- R.J. Adrian, K.T. Christensen, Z.-C. Liu, Analysis and interpretation of instantaneous turbulent velocity fields, *Experiments in Fluids* 29 (3) (2000) 275–290.
- R. Benzi, L. Biferale, Multifractality in the statistics of the velocity gradients in turbulence, *Physical Review Letters* 67 (1991) 2299-2302.
- B.J. Boersma, G. Brethouwer, F.T.M. Nieuwstadt, A numerical investigation on the effect of the inflow conditions on the self-similar region of a round jet, *Physics of Fluids* 10 (4) (1998) 899-909.
- L.W.B. Browne, R.A. Antonia, D.A. Shah, Turbulent energy dissipation in a wake, *Journal of Fluid Mechanics* 179 (1987) 307-326.
- P. Bradshaw, Y.M. Koh, A note on Poisson's equation for pressure in a turbulent flow, *Physics of Fluids* 24 (4) (1981) 777.
- H. Chen, J.R. Herring, R.M. Kerr, R.H. Kraichnan, Non-Gaussian statistics in isotropic turbulence, *Physics of Fluids A* 1 (11) (1989) 1844-1854.
- Y. Cheng, S. Pothos, F.J. Diez, Phase discrimination method for simultaneous two-phase separation in time-resolved stereo PIV measurements, *Experiments in Fluids* 49 (6) (2010) 1375-1391.
- Y. Cheng, M.M. Torregrosa, A. Villegas, F.J. Diez, Time resolved scanning PIV measurements at fine scales in a turbulent jet, *International Journal of Heat and Fluid Flow* 32 (3) (2011) 708-718.
- K.T. Christensen, R.J. Adrian, Measurement of instantaneous Eulerian acceleration fields by particle image accelerometry: method and accuracy, *Experiments in Fluids* 33 (2002) 759–769.
- S. Coudert, J. Westerweel, T. Fournel, Comparison between asymmetric and symmetric stereoscopic DPIV system, *Proceeding of 10th International Symposium on Applications of Laser Technology to Fluid Mechanics* (2000) Lisbon, Portugal.

- W.J.A. Dahm, K. Southerland, Experimental assessment of Taylor's hypothesis and its applicability to dissipation estimates in turbulent flows. *Physics of Fluids* 9 (1997) 2101-2107.
- W.J.A. Dahm, L.K. Su and K.B. Southerland, A scalar imaging velocimetry technique for fully resolved four-dimensional vector velocity field measurements in turbulent flows, *Physics of Fluids A4* (1992) 2191–2206.
- P.J. Diamessis, K.K. Nomura, Interaction of vorticity, rate-of-strain, and scalar gradient in stratified homogeneous sheared turbulence, *Physics of Fluids* 12 (5) (2000) 1166-1188.
- P.E. Dimotakis, The mixing transition in turbulent flows, *Journal of Fluid Mechanics* 409 (2000) 69-98.
- F.J. Diez, Y. Cheng, A. Villegas, Time resolved visualization of velocity gradients measured with near Kolmogorov-scale resolution in turbulent free-shear flows, *Experimental Thermal and Fluid Science* 35 (6) (2011) 1223-1229.
- F.J. Diez, W.J.A. Dahm, Effects of heat release on turbulent shear flows. Part 3. Buoyancy effects due to heat release in jets and plumes, *Journal of Fluid Mechanics* 575 (2007) 221-255.
- P.E. Dimotakis, Turbulent mixing, *Annual Review of Fluid Mechanics* 37 (2005) 329-356.
- D.A. Donzis, P.K. Yeung, K.R. Sreenivasan, Dissipation and enstrophy in isotropic turbulence: resolution effects and scaling in direct numerical simulations, *Physics of Fluids* 20 (4) (2008) 045108.
- S. Douady, Y. Couder, M.E. Brachet, Direct observation of the intermittency of intense vorticity filaments in turbulence 67 (8) (1991) 983-986.
- G.E. Elsinga, I. Marusic, Universal aspects of small-scale motions in turbulence, *Journal of Fluid Mechanics* 662 (2010) 514-539.
- G.E. Elsinga, F. Scarano, B. Wieneke, B.W. Oudheusden, Tomographic particle image velocimetry, *Experiments in Fluids* 41 (6) (2006) 933–947.
- J.M. Foucaut, J. Carlier, M. Stanislas, PIV optimization for the study of turbulent flow using spectral analysis, *Measurement Science and Technology* 15 (6) (2004) 1046–1058.
- C.A. Friehe, C.W. Van Atta, C.H. Gibson, Jet turbulence dissipation rate measurements and correlations, *AGARD Turbulent Shear Flows* 93 (1971) 18-1–18-7.
- U. Frisch, S.A. Orszag, Turbulence: challenges for theory and experiment 43 (1) (1990) 24.

- B. Ganapathisubramani, K. Lakshminarasimhan, N.T. Clemens, Investigation of three-dimensional structure of fine scales in a turbulent jet by using cinematographic stereoscopic particle image velocimetry, *Journal of Fluid Mechanics* 598 (2008) 141–175.
- B. Ganapathisubramani, E.K. Longmire, I. Marusic, S. Pothos, Dual-plane PIV technique to determine the complete velocity gradient tensor in a turbulent boundary layer, *Experiments in Fluids* 39 (2) (2005) 222–231.
- W.K. George, H.J. Hussein, Locally axisymmetric turbulence, *Journal of Fluid Mechanics* 233 (1991) 1–23.
- T. Gotoh, D. Fukayama, T. Nakano, Velocity field statistics in homogeneous steady turbulence obtained using a high-resolution direct numerical simulation, *Physics of Fluids* 14 (3) (2002) 1065–1080.
- G. Gulitski, M. Kholmyansky, W. Kinzelbach, B. LüThi, A. Tsinober, S. Yorish, Velocity and temperature derivatives in high-Reynolds-number turbulent flows in the atmospheric surface layer. Part 1. Facilities, methods and some general results, *Journal of Fluid Mechanics* 589 (2007).
- D. Han, L.K. Su, R.K. Menon, M.G. Mungal, Study of a lifted-jet flame using a stereoscopic PIV system. *Proceedings of 10th International Symposium on Applications of Laser Techniques to Fluid Mechanics* (2000) Lisbon, Portugal.
- D.P. Hart, PIV error correction, *Experiments in Fluids* 29 (1) (2000) 13–22.
- E.F. Hasselbrink JR, M.G. Mungal, Transverse jets and jet flames. Part 2. Velocity and OH field imaging, *Journal of Fluid Mechanics* 433 (2001) 27–68.
- M. Holzner, A. Liberzon, N. Nikitin, B. LüThi, W. Kinzelbach, A. Tsinober, A Lagrangian investigation of the small-scale features of turbulent entrainment through particle tracking and direct numerical simulation, *Journal of Fluid Mechanics* 598 (2008) 465–475.
- M. Holzner, B. Luthi, A. Tsinober, W. Kinzelbach, Acceleration, pressure and related quantities in the proximity of the turbulent/non-turbulent interface, *Journal of Fluid Mechanics* 639 (2009) 153–165.
- H. Huang, D. Dabiri, M. Gharib, On errors of digital particle image velocimetry, *Measurement Science and Technology* 8 (1997) 1427–1440.
- H.J. Hussein, S.P. Capp, W.K. George, Velocity measurements in a high-Reynolds-number, momentum-conserving, axisymmetric, turbulent jet, *Journal of Fluid Mechanics* 258 (1994) 31–75.
- T. Hori, J. Sakakibara, High-speed scanning stereoscopic PIV for 3D vorticity measurement in liquids, *Measurement Science and Technology* 15 (6) (2004) 1067–1078.

- T. Ishihara, T. Gotoh, Y. Kaneda, Study of high-Reynolds number isotropic turbulence by direct numerical simulation, *Annual Review of Fluid Mechanics* 41 (1) (2009) 165–180.
- M. Ishikawa, Y. Murai, A. Wada, M. Iguchi, K. Okamoto, F. Yamamoto, A novel algorithm for particle tracking velocimetry using the velocity gradient tensor, *Experiments in Fluids* 29 (2000) 519-531.
- J. Jeong, F. Hussain, On the identification of a vortex, *Journal of Fluid Mechanics* 285 (1995) 69-94.
- J. Jiménez, A.A. Wray, P.G. Saffman, R.S. Rogallo, The structure of intense vorticity in isotropic turbulence, *Journal of Fluid Mechanics* 255 (1993) 65–90.
- C. Kalelkar, Statistics of pressure fluctuations in decaying isotropic turbulence, *Physical Review E* 73 (2006) 046301-1-10.
- Y. Kaneda, T. Ishihara, High-resolution direct numerical simulation of turbulence, *Journal of Turbulence* 7 (20) (2006) 1-17.
- R. Kerr, Higher-order derivative correlations and the alignment of small scale structures in isotropic numerical turbulence, *Journal of Fluid Mechanics* 153 (1985) 31-58.
- M. Kholmyansky, A. Tsinober, S. Yorish, Velocity derivatives in the atmospheric surface layer at $Re_\lambda = 10^4$, *Physics of Fluids* 13 (2001) 311–314.
- J. Kim, P. Moin, R. Moser, Turbulence statistics in fully developed channel flow at low Reynolds number, *Journal of Fluid Mechanics* 177 (1987) 133-166.
- S.J. Kline, W.C. Reynolds, F.A. Schraub, P.W. Runstadler, The structure of turbulent boundary layers, *Journal of Fluid Mechanics* 30 (1967) 741-773.
- V. Kolář, Vortex identification: new requirements and limitations, *International Journal of Heat and Fluid Flow* 28 (2007) 638-652.
- A. N. Kolmogorov, The local structure of turbulence in incompressible viscous fluid for very large Reynolds numbers, *Proceedings of Royal Society of London A* 434 (1991) 9-13,
- P.S. Kothnur, N.T. Clemens, Effects of unsteady strain rate on scalar dissipation structures in turbulent planar jets, *Physics of Fluids* 17 (12) (2005) 125104.
- D.B. Lang, P.E. Dimotakis, Measuring vorticity using the laser Doppler velocimeter, *The Bulletin of the American Physical Society* 27 (9) (1982) 1166.
- P. Lavoie, G. Avallone, F. Gregorio, G.P. Romano, R.A. Antonia, Spatial resolution of PIV for the measurement of turbulence, *Experiments in Fluids* 43 (1) (2007) 39–51.

- N.J. Lawson, J. Wu, Three-dimensional particle image velocimetry: error analysis of stereoscopic techniques, *Measurement Science and Technology* 8 (1997) 894-900.
- N.J. Lawson, J. Wu, Three-dimensional particle image velocimetry: experimental error analysis of a digital angular stereoscopic system, *Measurement Science and Technology* 8 (1997) 1455-1464.
- T.S. Lund, M.M. Rogers, An improved measure of strain state probability in turbulent flows, *Physics of Fluids* 6 (1994) 1838–1847.
- T. Makihara, S. Kida, H. Miura, Automatic tracking of low-pressure vortex, *Journal of the Physical Society of Japan* 71 (7) (2002) 1622-1625.
- J. Martin, C Dopazo, Dynamics of velocity gradient invariants in turbulence: restricted Euler and linear diffusion models, *Physics of Fluids* 10 (8) (1998) 2012-2025.
- M.V. Melander, Polarized vorticity dynamics on a vortex column, *Physics of Fluids A* 5 (8) (1993) 1992-2003.
- C. Meneveau, J. Katz, Conditional subgrid force and dissipation in locally isotropic and rapidly strained turbulence, *Physics of Fluids* 11 (8) (1999) 2317-2329.
- H. Meng, F. Hussain, Holographic particle velocimetry: a 3D measurement technique for vortex interactions, coherent structures and turbulence, *Fluid Dynamics Research* 8 (1-4) (1991) 33-52.
- G.J. Merkel, P. Rys, F.S. Rys, T. Dracos, Concentration and velocity field measurements in turbulent flows by laser induced fluorescence tomography, *Proceedings of EUROMEC Workshop on Imaging Techniques and Analysis in Fluid Dynamics* (1995) Rome.
- F. Moisy, J. Jiménez, Geometry and clustering of intense structures in isotropic turbulence, *Journal of Fluid Mechanics* 513 (2004) 111–133.
- J.A. Mullin, W.J.A. Dahm, Dual-plane stereo particle image velocimetry (DSPIV) for measuring velocity gradient fields at intermediate and small scales of turbulent flows, *Experiments in Fluids* 38 (2) (2005) 185–196.
- J.A. Mullin, W.J.A. Dahm, Dual-plane stereo particle image velocimetry measurements of velocity gradient tensor fields in turbulent shear flow. II. Experimental results, *Physics of Fluids* 18 (3) (2006) 035102.
- K.K. Nomura, G.K. Post, The structure and dynamics of vorticity and rate of strain in incompressible homogeneous turbulence, *Journal of Fluid Mechanics* 377 (1998) 65-97.
- M.G. Olsen, J.C. Dutton, Planar velocity measurements in a weakly compressible mixing layer, *Journal of Fluid Mechanics* 486 (2003) 51-77.

- L. Ong, J.M. Wallace, Joint probability density analysis of the structure and dynamics of the vorticity field of a turbulent boundary layer, *Journal of Fluid Mechanics* 367 (1998) 291-328.
- T. Passot, H. Politano, P.L. Sulem, J.R. Angilella, M. Meneguzzi, Instability of strained vortex layers and vortex tube formation in homogeneous turbulence, *Journal of Fluid Mechanics* 282 (1995) 313-338.
- B.R. Pearson, P.A. Korgstad, W. van de Water, Measurements of the turbulent energy dissipation rate, *Physics of Fluids* 14 (3) (2002) 1288-1290.
- A.E. Perry, M.S. Chong, Topology of flow patterns in vortex motions and turbulence, *Applied Scientific Research* 53 (1994) 357-374.
- M. Piirto, P. Saarenrinne, H. Eloranta, R. Karvinen, Measuring turbulence energy with PIV in a backward-facing step flow, *Experiments in Fluids* 35 (2003) 219-236.
- C. Poelma, J. Westerweel, G. Ooms, Turbulence statistics from optical whole field measurements in particle-laden turbulence, *Experiments in Fluids* 40 (3) (2006) 347-363.
- S.B. Pope, *Turbulent flows*, Cambridge University Press, 2000.
- P. Saarenrinne, M. Piirto, Turbulent kinetic energy dissipation rate estimation from PIV velocity vector fields, *Experiments in Fluids* 29 (2000) 300-307.
- J. Sakakibara, K. Hishida, W.R.C. Phillips, On the vortical structure in a plane impinging jet, *Journal of Fluid Mechanics* 434 (2001) 273-300.
- J. Schumacher, B. Eckhardt, C.R. Doering, Extreme vorticity growth in Navier-Stokes turbulence, *Physics Letters A* 374 (2010) 861-865.
- Z.S. She, E. Jackson, S.A. Orzag, Intermittent vortex structures in homogeneous isotropic turbulence, *Nature* 344 (1990) 226-228.
- J. Sheng, E. Malkiel, J. Katz, Using digital holographic microscopy for simultaneous measurements of 3D near wall velocity and wall shear stress in a turbulent boundary layer, *Experiments in Fluids* 45 (6) (2008) 1023-1035.
- E.D. Siggia, Numerical study of small-scale intermittency in three-dimensional turbulence, *Journal of Fluid Mechanics* 107 (1981) 375-406.
- K.R. Sreenivasan, Fluid turbulence, *Reviews of Modern Physics* 71 (2) (1999) S383-S395.
- K.R. Sreenivasan, R.A. Antonia, The phenomenology of small-scale turbulence, *Annual Review of Fluid Mechanics* 29 (1) (1997) 435-472.

K. Staack, R. Geisler, A. Schröder, D. Michaelis, 3D3C-coherent structure measurements in a free turbulent jet, 15th Int Symp on Applications of Laser Techniques to Fluid Mechanics, Lisbon, Portugal, 05-08 July, 2010.

A.M. Steinberg, J.F. Driscoll, S.L. Ceccio, Three-dimensional temporally resolved measurements of turbulence–flame interactions using orthogonal-plane cinema-stereoscopic PIV, *Experiments in Fluids* 47 (2009) 527-547.

T. Tanaka, J.K. Eaton, A correction method for measuring turbulence kinetic energy dissipation rate by PIV, *Experiments in Fluids* 42 (6) (2007) 893–902.

B. Tao, J. Katz, C. Meneveau, Geometry and scale relationships in high Reynolds number turbulence determined from three-dimensional holographic velocimetry, *Physics of Fluids* 12 (2000) 941.

G.I. Taylor, Statistical theory of turbulence, , *Proceedings of Royal Society of London A* 151 (873) (1935) 421-444.

H. Tennekes, Eulerian and Lagrangian time microscales in isotropic turbulence, *Journal of Fluid Mechanics* 67 (1957) 561-567.

H. Tennekes, J. Lumley, *A first course in turbulence*, MIT Press, Cambridge, Massachusetts, USA, 1972.

A. Thacker, S. Loyer, S. Aubrun, Comparison of turbulence length scales assessed with three measurement systems in increasingly complex turbulent flows, *Experimental Thermal and Fluid Science* (2009).

A. Tsinober, E. Kit, and T. Dracos, Experimental investigation of the field of velocity gradients in turbulent flows, *Journal of Fluid Mechanics* 242 (1992) 169-192.

A. Tsinober, P. Vedula, P.K. Yeung, Random Taylor hypothesis and the behavior of local and convective accelerations in isotropic turbulence, *Physics of Fluids* 13 (7) (2001) 1974–1984.

A. Vincent, M. Meneguzzi, The spatial structure and statistical properties of homogeneous turbulence, *Journal of Fluid Mechanics* 225 (1991) 1-20.

J.M. Wallace, Twenty years of experimental and direct numerical simulation access to the velocity gradient tensor: what have we learned about turbulence?, *Physics of Fluids* 21 (2) (2009) 021301

J.M. Wallace, P.V. Vukoslavcevic, Measurement of the velocity gradient tensor in turbulent flows, *Annual Review of Fluid Mechanics* 42 (2010) 157–181.

L. Wang, On properties of fluid turbulence along streamlines, *Journal of Fluid Mechanics* 648 (2010) 183-203.

- T.H. Weisgraber, D. Liepmann, Turbulent structure during transition to self-similarity in a round jet, *Experiments in Fluids* 24 (1998) 210-224.
- J. Westerweel, D. Dabiri, M. Gharib, The effect of a discrete window offset on the accuracy of cross-correlation analysis of digital PIV recordings, *Experiments in Fluids* 23 (1) (1997) 20–28.
- J. Westerweel, C. Fukushima, J. M. Pedersen, J.C.R. Hunt, Mechanics of the turbulent-nonturbulent interface of a jet, *Physical Review Letters* 95 (2005) 174501-1-4.
- J. Westerweel, T. Hofmann, C. Fukushima, J.C.R. Hunt, The turbulent/non-turbulent interface at the outer boundary of a self-similar turbulent jet, *Experiments in Fluids* 33 (2002) 873–878.
- B. Wieneke, Stereo-PIV using self-calibration on particle images, *Experiments in Fluids* 39 (2005) 267–280.
- M. Wilczek, A. Daitche, R. Friedrich, On the velocity distribution in homogeneous isotropic turbulence: correlations and deviations from Gaussianity, *Journal of Fluid Mechanics* (2011) doi:10.1017/jfm.2011.39.
- C. Willert, Stereoscopic digital particle image velocimetry for application in wind tunnel flows, *Measurement Science and Technology* 8 (1007) 1465-1479.
- I. Wygnanski, H. Fiedler, Some measurements in the self-preserving jet, *Journal of Fluid Mechanics* 38 (1969) 577-612.
- J. Zhang, B. Tao, J. Katz, Turbulent flow measurement in a square duct with hybrid holographic PIV, *Experiments in Fluids* 23 (1997) 373-381.
- B. Yip, R.L. Schmitt. M.B. Long, Instantaneous three-dimensional concentration measurements in turbulent jets and flames, *Optics Letters* 13 (1988) 96–98.
- B.W. Zeff, D.D. Lanterman, R. McAllister, R. Roy, E.J. Kostelich, D.P. Lathrop, Measuring intense rotation and dissipation in turbulent flows, *Nature* 421 (6919) (2003) 146–149.